

CHARACTERIZING THE IMPACT OF VIRAL PROTEIN BINDING ON THE FUNCTION
OF THE DEAD-BOX RNA HELICASE DDX3X

by

SARAH VENUS

Submitted in partial fulfillment of the requirements for the degree of
Doctor of Philosophy

Dissertation advisor: Dr. Eckhard Jankowsky

Department of Biochemistry
CASE WESTERN RESERVE UNIVERSITY

January 2023

CASE WESTERN RESERVE UNIVERSITY
SCHOOL OF GRADUATE STUDIES

We hereby approve the thesis/dissertation of

Sarah Venus

Candidate for the Doctor of Philosophy degree *

William C. Merrick (chair of the committee)

Eckhard Jankowsky

Donny Licatalosi

Derek Abbott

(date) July 25, 2022

*We also certify that written approval has been obtained for any proprietary material contained therein.

Table of Contents

List of figures	v
Acknowledgments	vii
List of abbreviations	ix
Abstract	xv
Chapter 1: General introduction to DEAD-box RNA helicases and their associated cofactors	1
1.1 Introduction to RNA helicase families	1
1.2 Mechanisms of RNA helicase enzymatic activity.....	2
1.3 DEAD-box RNA helicase architecture	6
1.4 Biological functions of eukaryotic DEAD-box RNA helicases	6
1.4.1 Transcription	7
1.4.2 Pre-mRNA splicing.....	8
1.4.3 mRNA export	8
1.4.4 Translation	9
1.4.5 RNA decay.....	10
1.4.6 Ribosome biogenesis.....	10
1.4.7 tRNA processing	11
1.4.8 snRNA processing	12
1.4.9 miRNA processing	12
1.4.10 piRNA processing	12
1.4.11 Mitochondrial RNA metabolism.....	13
1.5 DEAD-box RNA helicase cofactors	13
1.5.1 eIF4A cofactors.....	14
1.5.2 Ded1p cofactors.....	15
1.5.3 Dbp5p cofactors.....	16
1.5.4 Dbp2p cofactors.....	17
1.5.5 eIF4AIII cofactors.....	17
1.5.6 Dbp8p cofactors.....	18
1.5.7 Vasa cofactors	18

1.6	DEAD-box RNA helicases in human disease	18
Chapter 2: Introduction to RNA helicases in biomolecular condensates ...		20
2.1	Overview of biomolecular condensates	20
2.1.1	Types of biomolecular condensates	20
2.1.2	Biomolecular condensates in disease	23
2.2	Formation of biomolecular condensates	25
2.3	RNA helicases in biomolecular condensates	27
Chapter 3: Introduction to the DEAD-box RNA helicase DDX3X.....		31
3.1	DDX3X structure and enzymatic activity	31
3.2	Biological roles of DDX3X	38
3.3	DDX3X in human disease	43
3.3.1	DDX3X syndrome	43
3.3.2	DDX3X dysregulation in cancer	44
3.3.3	DDX3X in viral infections.....	47
Chapter 4: The viral protein K7 impacts DDX3X enzymatic activity by binding to DDX3X's disordered N-terminus		51
4.1	Introduction	51
4.2	K7 inhibits RNA unwinding by DDX3X	54
4.3	K7 inhibits RNA-dependent ATPase activity of DDX3X.....	56
4.4	K7 diminishes functional RNA binding by DDX3X	58
4.5	Discussion	59
Chapter 5: The viral protein K7 impacts DDX3X condensate formation <i>in vitro</i> and in human cells		63
5.1	Introduction	63
5.2	K7 inhibits condensate formation by DDX3X <i>in vitro</i>	65
5.3	K7 reduces DDX3X association with cellular stress granules	66
5.4	K7 reduces condensate formation by mutant DDX3X in cells	69
5.5	Discussion.....	72
Chapter 6: The viral protein K7 has minimal effects on global translation..		75
6.1	Introduction	75
6.2	K7 does not impact DDX3X association with the ribosome	76
6.3	K7 slightly reduces global translation	78
6.4	Discussion	82

Chapter 7: Modulation of DDX3X condensate formation by small molecules	84
7.1 Introduction	84
7.2 Bis-ANS exerts biphasic effects on liquid-liquid phase separation	85
7.3 Amino acids regulate Ded1p/DDX3X liquid-liquid phase separation	91
7.4 Discussion	94
Chapter 8: Summary and future directions	96
8.1 K7's therapeutic potential in DDX3X-associated diseases	96
8.2 Viral benefits of preventing DDX3X association with stress granules.....	103
8.3 Effect of K7 on DDX3X-dependent translation	109
8.4 Effects of other viral proteins that bind DDX3X	109
8.5 Effect of post-translational modifications	112
8.6 Determining the exact mechanism behind K7-mediated inhibition of DDX3X.....	113
8.7 DDX3X oligomerization as a precursor to liquid-liquid phase separation.....	114
Chapter 9: Materials and Methods	117
9.1 Protein purification.....	117
9.1.1 DDX3X	117
9.1.2 Truncated DDX3X (Δ DDX3X)	118
9.1.3 Ded1p	119
9.1.4 His-K7	120
9.1.5 Tau.....	121
9.1.6 FUS low complexity domain	121
9.1.7 SUMO protease	122
9.1.8 Determination of protein concentration	123
9.2 RNA unwinding assays	123
9.2.1 Formation of radiolabeled RNA duplex	123
9.2.2 Pre-steady state RNA unwinding assays	124
9.2.3 Equation fitting	125
9.3 ATP hydrolysis assays	126
9.4 Formaldehyde crosslinking.....	127
9.5 Liquid-liquid phase separation assays.....	127

9.6 Cloning	129
9.6.1 pEBB.myc-K7 / pEBB.myc	129
9.6.2 pEBB.DDX3XGFP-p2a-mycK7 / pEBB.DDX3XGFP-p2a-myc	130
9.6.3 Generation of DDX3X mutants (R534H, G302V, G325E, FFAA)	131
9.6.4 pMax.GFP-p2a-mycK7 / pMax.GFP-p2a-myc	132
9.7 Immunofluorescence	133
9.7.1 Image analysis	134
9.8 Western blotting	136
9.9 Polysome profiling	138
9.9.1 Analysis of polysome-associated proteins	139
9.10 Growth curves	139
9.11 CellTiter-Glo	140
9.12 MTT assay	140
9.13 Live cell imaging with bis-ANS	141
9.14 Propidium iodide staining	142
Appendix 1	143
Bibliography.....	150

List of figures

Figure 1.1. Biochemical activities of SF1 and SF2 helicases.....	2
Figure 1.2. Duplex unwinding mechanisms by RNA helicases.....	3
Figure 1.3. DEAD-box RNA helicase motifs.....	6
Figure 1.4. DEAD-box RNA helicase functions in RNA metabolism.....	7
Figure 1.5. Potential cofactor effects.....	14
Figure 3.1. DDX3X architecture.....	31
Figure 3.2. RNA-bound DDX3X crystal structure.....	35
Figure 3.3. Structural model for cooperative RNA duplex unwinding by the Minimal DDX3X unwinding unit dimer.....	36
Figure 3.4. DDX3X interactions during innate immune signaling.....	42
Figure 4.1. K7 binds DDX3X.....	53
Figure 4.2. Purification of DDX3X and K7.....	54
Figure 4.3. RNA unwinding by DDX3X in the presence of K7.....	56
Figure 4.4. ATP hydrolysis by DDX3X in the presence of K7.....	57
Figure 4.5. Dependence of RNA unwinding rate constants on DDX3X and ATP concentration in the presence of K7.....	59
Figure 4.6. Oligomerization of full-length and truncated DDX3X.....	61
Figure 4.7. K7 effects on DDX3X oligomerization.....	62
Figure 5.1. Formation of recombinant DDX3X condensates in the presence of K7.....	66
Figure 5.2. Stress granule formation in K7-expressing HCT 116 cells.....	68
Figure 5.3. Stress granule formation in cells expressing K7 without GFP.....	69
Figure 5.4. Co-expression of GFP-tagged DDX3X and myc-tagged K7 in human cells.....	70

Figure 5.5. Formation of granules with mutant DDX3X in K7-expressing cells.....	71
Figure 5.6. Expression of mutant GFP-tagged DDX3X in human cells.....	72
Figure 6.1. Co-expression of GFP and myc-tagged K7 in human cells.....	77
Figure 6.2. Impact of K7 on DDX3X association with translating ribosomes.....	78
Figure 6.3. Global translation in K7-expressing cells.....	79
Figure 6.4. Viability and growth of K7-expressing cells.....	80
Figure 6.5. Global translation in DDX3X-depleted cells.....	81
Figure 6.6. Localization of degron-tagged DDX3X.....	82
Figure 7.1. Chemical structure of bis-ANS (4,4'-dianilino-1,1'-binaphthyl-5,5'-disulfonic acid).....	85
Figure 7.2. Impact of bis-ANS on LLPS.....	87
Figure 7.3. Impact of bis-ANS on stress granules.....	89
Figure 7.4. Treatment with bis-ANS does not induce stress granule formation...	90
Figure 7.5. Effect of free amino acids on Ded1p condensate formation.....	92
Figure 7.6. Impact of proline on DDX3X and Ded1p condensate formation.....	93
Figure 8.1. Sequence alignment between DDX3X and Ded1p N-terminus.....	99
Figure 8.2. K7 binds Ded1p.....	99
Figure 8.3. Impact of K7 on RNA unwinding by Ded1p.....	99
Figure 8.4. Impact of K7 on Ded1p condensate formation.....	100
Figure 8.5. Impact of K7 on aberrant granules formed by DDX3X ^{G302V} and DDX3X ^{G325E}	103
Figure 8.6. Preliminary test of whether K7 expression alters cell survival during stress.....	108
Figure 8.7. Map of identified post-translational modifications on DDX3X.....	112

Acknowledgments

First, I want to thank my thesis advisor, Dr. Eckhard Jankowsky, for his support and encouragement over the past five years. I am thankful that he encouraged me to push my boundaries and try new things, while also being supportive if/when things didn't turn out the way we expected. He taught me to communicate clearly and think critically. I am grateful to have had the opportunity to develop my scientific skills in his laboratory.

I would also like to thank my thesis committee for their insight and support throughout the course of this project and my own development as a scientist. I especially want to thank Dr. Derek Abbott for his MSTP-specific guidance, as well as for making space for me in his laboratory so I could learn various techniques from his team. I also owe special thanks to Dr. William Merrick for his careful reading of my thesis draft and helpful comments.

I am especially grateful to the RNA Center and my fellow Jankowsky labmates for creating such a fun and collaborative environment to do science in. I always looked forward to coming to work even if I wasn't looking forward to the tasks I had planned for the day. Special thanks to Sukanya Srinivasan for being a great friend and for teaching me almost everything I know about *in vitro* helicase assays, Brittany Stawicki for being the best bench mate I could have asked for (and for lending me her time and polysome profiling expertise), Soon Yeul Yi for comedic relief and all his hard work on the helicase database/helicase review tables, Christine Lee-Poturalski for patiently teaching me tissue culture, Kaba Tandjigora for being the other member of the Jankowsky lab DDX3X team and

purifying Δ DDX3X, Dr. Andrea Putnam for taking the time to talk to me about helicases and liquid-liquid phase separation, and Dr. Zhaofeng Gao for teaching me about qPCR and flow cytometry. Special thanks are also owed to Dr. Joseph Luna for helping me drastically improve (and automate!) my stress granule image analysis.

I am also deeply grateful for my MSTP cohort. They kept me sane on the hard days and enjoyed the good days with me. I am especially grateful for my bestie Dr. Alicia Vagnozzi, as well as for Dr. Bowen Zhou, who spent lots of time teaching me about cloning and CRISPR.

Finally, I want to thank my family for their unconditional love and support. My brother Donald has always been my biggest fan and loudest supporter. I am especially thankful to my partner Bill for always being there to make me laugh and remind me that there's a world outside of school. I couldn't have done this work without the knowledge that my family would always have my back. Thank you.

List of abbreviations

Ago2: protein argonaute-2

ADP: adenosine diphosphate

ADPNP: 5'-adenylyl beta,gamma-imidodiphosphate

ALS: amyotrophic lateral sclerosis

AMPPNP: adenylyl-imidodiphosphate

ATCC: American Type Culture Collection

ATP: adenosine triphosphate

ATPase: adenosine triphosphatase

AVG: antiviral granule

bp: basepair

bis-ANS: 4,4'-dianilino-1,1'-binaphthyl-5,5'-disulfonic acid

BSA: bovine serum albumin

CAPRN1: cell cycle associated protein 1

cGAS: cyclic GMP-AMP synthase

CHEVI: class C homologues in endosome-vesicle interaction

circRNA: circular RNA

CK1 ϵ : casein kinase 1 isoform epsilon

CLIP: UV cross-linking and immunoprecipitation

CRM1: chromosomal maintenance 1

CTP: cytidine triphosphate

DMSO: dimethyl sulfoxide

DNA: deoxyribonucleic acid

DPBS: Dulbecco's phosphate-buffered saline

dpm: disintegrations per minute

dsDNA: doublestranded DNA

dsRNA: double stranded RNA

EDTA: ethylenediaminetetraacetic acid

eIF: eukaryotic initiation factor

FBS: fetal bovine serum

FMRP: fragile X mental retardation protein

FRAP: fluorescence recovery after photobleaching

FTD: frontotemporal dementia

FUS: fused in sarcoma

FXTAS: fragile X-associated tremor/ataxia syndrome

G3BP1/2: Ras GTPase-activating protein-binding protein 1/2

GFP: green fluorescent protein

GTP: guanosine triphosphate

HBV: hepatitis B virus

HCV: hepatitis C virus

HDAC6: histone deacetylase 6

hnRNPA1: heterogenous nuclear ribonucleoprotein A1

HNSCC: head and neck squamous cell carcinoma

hr: hour

IAA: indole 3-acetic acid

IBV: infectious bronchitis virus

IDR: intrinsically disordered region

IFN- β : interferon beta

IGEPAL CA-630: octylphenoxyethoxyethanol

IKK α : inhibitor of nuclear factor kappa-B kinase subunit alpha

IKK ϵ : inhibitor of nuclear factor kappa-B kinase subunit epsilon

InsP₆: inositol-hexakisphosphate

IRAK2: interleukin 1 receptor associated kinase 2

IRF-3/p300/CBP complex: interferon regulatory factor 3/CREB-binding protein/p300 complex

kb: kilobase

kDa: kilodaltons

LLPS: liquid-liquid phase separation

LPS: lipopolysaccharide

lncRNA: long noncoding RNA

mAID: mini auxin inducible degron

MAVS: mitochondrial antiviral-signaling protein

MBP: maltose binding protein

MDA5: melanoma differentiation-associated protein 5

min: minutes

miRNA: micro RNA

MOPS: 3-(N-morpholino)propanesulfonic acid

mRNA: messenger RNA

mRNP: messenger ribonucleoprotein

MTT: 3-(4,5-dimethylthiazol-2-yl)-2,5-diphenyltetrazolium bromide

NEAT1: nuclear paraspeckle assembly transcript 1

Ni-NTA: nickel-nitrilotriacetic acid

nt: nucleotides

NTP: nucleotide triphosphate

NTPase: nucleotide triphosphatase

OSCC: oral squamous cell carcinoma

PACT: protein activator of the interferon-induced protein kinase

PAGE: polyacrylamide gel electrophoresis

PBS: phosphate-buffered saline

PcG body: polycomb group body

PCR: polymerase chain reaction

Pdcd4: programmed cell death protein 4

PEI-cellulose: polyethylenimine-cellulose

piRNA: piwi-interacting RNA

PKR: protein kinase R

PML: promyelocytic leukemia protein

PMSF: phenylmethylsulfonyl fluoride

PVDF: polyvinylidene fluoride

R16/41-3: 16 bp RNA duplex with a 3'- 25 nt ssRNA tail

RAN: repeat-associated non-AUG

RBP: RNA binding protein

RIG-I: retinoic acid-inducible gene I

RISC: RNA-induced silencing complex

RNA: ribonucleic acid

RNP: ribonucleoprotein

rRNA: ribosomal RNA

SDS: sodium dodecyl sulfate

SDS-PAGE: sodium dodecyl sulfate-polyacrylamide gel electrophoresis

SF: superfamily

SHH: sonic hedgehog

SMN complex: survival motor neuron complex

SNAT2: sodium-dependent neutral amino acid transporter 2

snoRNA: small nucleolar RNA

snoRNP: small nucleolar ribonucleoprotein

snRNA: small nuclear RNA

snRNP: small nuclear ribonucleoprotein

Sp1: specificity protein 1

Spir-1: spire type actin nucleation factor 1

ssRNA: single-stranded RNA

STAT1: signal transducer and activator of transcription 1

TAP: transporter associated with antigen processing

TBK1: TANK-binding kinase 1

TDP-43: TAR DNA-binding protein 43

TEV: Tobacco Etch Virus

TLC: thin layer chromatography

TMAO: trimethylamine N-oxide

TRAF3: TNF receptor-associated factor 3

TRAF6: TNF receptor-associated factor 6

TRAMP complex: Trf4/Air2/Mtr4p polyadenylation complex

TRBP: transactivation response RNA binding protein

tRNA: transfer RNA

TTP: tristetraprolin

UTP: uridine triphosphate

UTR: untranslated region

VACV: vaccinia virus

YY1: yin yang 1

ZNFX1: zinc finger NFX1-type containing 1

Characterizing the Impact of Viral Protein Binding on the Function of the DEAD-box RNA Helicase DDX3X

Abstract
by

SARAH VENUS

The DEAD-box RNA helicase DDX3X is targeted by proteins from diverse viruses, including K7 from vaccinia virus, core protein from Hepatitis C virus, NS1 and NP proteins from influenza A virus, and capsid protein from dengue virus. These interactions have been shown to disrupt DDX3X-mediated promotion of innate immune signaling; however, it is unknown whether and how these viral proteins impact the biochemical and cellular functions of DDX3X.

Biochemically, DDX3X hydrolyzes ATP and unwinds RNA duplexes. In the cell, this biochemical activity enables DDX3X to promote translation initiation by remodeling structured mRNAs. Vaccinia virus K7 protein binds to the N-terminus of DDX3X that contains large intrinsically disordered regions. These intrinsically disordered regions mediate DDX3X's oligomerization required for optimal helicase activity *in vitro* and DDX3X's association with stress granules in the cell.

Here I show that K7 binding to DDX3X's N-terminus inhibits the ATP-dependent RNA unwinding and RNA-dependent ATP hydrolysis activities of DDX3X by reducing the functional RNA affinity of DDX3X. K7 also reduces the formation of recombinant DDX3X phase-separated droplets *in vitro*. In cells, K7

inhibits formation of DDX3X-containing stress granules. In addition, K7 reduces the formation of aberrant DDX3X foci induced by mutations in DDX3X that are associated with medulloblastoma and intellectual disability. Finally, K7 reduces global translation in HCT 116 cells by approximately 14%, suggesting that K7-mediated inhibition of DDX3X helicase activity may reduce translation of structured DDX3X-dependent transcripts.

Our data reveal that K7 binding to the intrinsically disordered N-terminus of DDX3X is an effective way to interfere with the ability of DDX3X to resolve RNA structure and to undergo liquid-liquid phase separation. Dual inhibition of DDX3X enzymatic activity and condensate formation by K7 binding suggests that the N-terminal extension of DDX3X participates in inter-DDX3X interactions important for both DDX3X oligomerization and DDX3X liquid-liquid phase separation. Our findings also provide mechanistic insight into viral strategies that target DDX3X to alter host RNA metabolism, as well as highlight potential strategies to therapeutically target aberrant liquid-liquid phase separation linked to DDX3X mutations in medulloblastoma and intellectual disability.

Chapter 1

General introduction to DEAD-box RNA helicases and their associated cofactors

Portions of Chapter 1 were adapted with permission from Methods volume 204, Venus S and Jankowsky E, Measuring the impact of cofactors on RNA helicase activities, pages 376-385, copyright Elsevier (2022).

1.1 Introduction to RNA helicase families

RNA helicases are enzymes that utilize nucleotide triphosphates to bind and/or remodel RNA, RNA-protein complexes, or both^{1,2}. RNA helicases have been identified in bacteria, archaea, eukaryotes, and many viruses³. RNA helicases constitute the largest class of enzymes in RNA metabolism, with more than 70 members in humans⁴. All eukaryotic RNA helicases share a structurally highly conserved helicase core consisting of two RecA-like domains, arranged in tandem via a flexible linker^{2,5}. The conserved helicase core contains 8 to 13 highly conserved, characteristic helicase motifs^{1,6}, and the helicase core is often flanked by variable C- and N-terminal extensions¹. Based on the conserved core motifs and small structural variations in the helicase core, RNA helicases are classified into two helicase superfamilies (SF1, SF2), which also contain structurally closely related DNA helicases⁶. RNA helicases in each superfamily are further divided into distinct families, including the DEAD-box, DEAH/RHA, Ski2-like, Rig-I-like for SF2, and Upf1-like for SF1^{1,6} (**Fig. 1.1**). Work by many groups over the last three decades has revealed family-specific biochemical functions^{6,7} (**Fig. 1.1**).

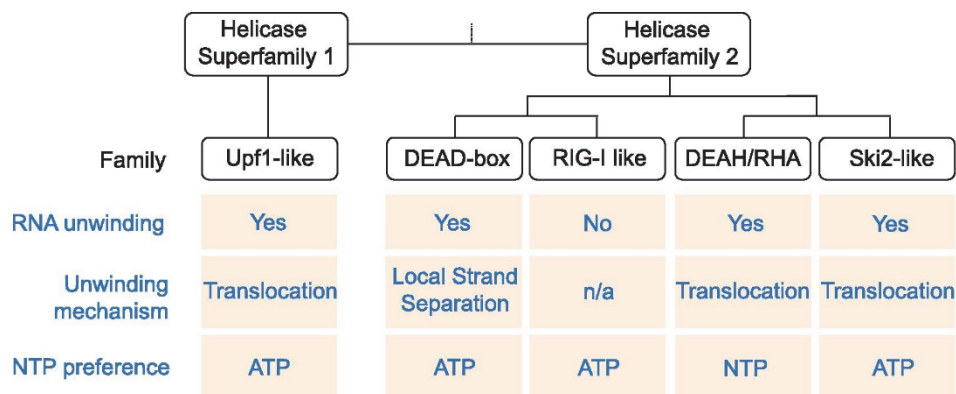


Figure 1.1. Biochemical activities of SF1 and SF2 helicases. Eukaryotic RNA helicase families and their major biochemical activities. The schematic phylogeny is not to scale.

1.2 Mechanisms of RNA helicase enzymatic activity

As noted above, RNA helicases bind and remodel RNA and/or RNA-protein complexes in an ATP-dependent manner^{1,2}. This remodeling activity occurs via multi-step reactions that comprise the binding and remodeling of RNA (strand separation or resolving of RNA structure) and the binding and hydrolysis of NTPs (**Fig. 1.2**). Each RNA helicase family employs one of two distinct modes to perform these multi-step reactions (**Fig. 1.2**). DEAH/RHA, Upf1-like, and Ski2-like RNA helicases unwind RNA via translocation (**Fig. 1.1 & 1.2a**). DEAH/RHA helicases translocate relative to a single strand of RNA^{1,2}, with most eukaryotic DEAH/RHA helicases only performing few contiguous translocation steps before dissociating from the RNA⁸. Upf1-like (SF1) RNA helicases can translocate on an RNA strand with considerable processivity⁹. Ski2-like RNA helicases also appear to translocate while unwinding duplexes^{10,11}.

DEAD-box RNA helicases are the largest helicase family and do not translocate to unwind duplexes^{1,2,12}. Instead, DEAD-box RNA helicases load directly onto the duplex RNA, often aided by nearby unpaired RNA stretches, and

then pry the strands apart in an ATP-dependent fashion^{1,2} (**Fig. 1.2b**). This unwinding mechanism is termed local strand separation and is well suited for specific local rearrangements of RNA structure in multi-component RNA and RNA-protein complexes^{1,2,12}. Both DEAD-box RNA helicases and translocating RNA helicases also have the ability to displace bound proteins from RNA¹³⁻¹⁶.

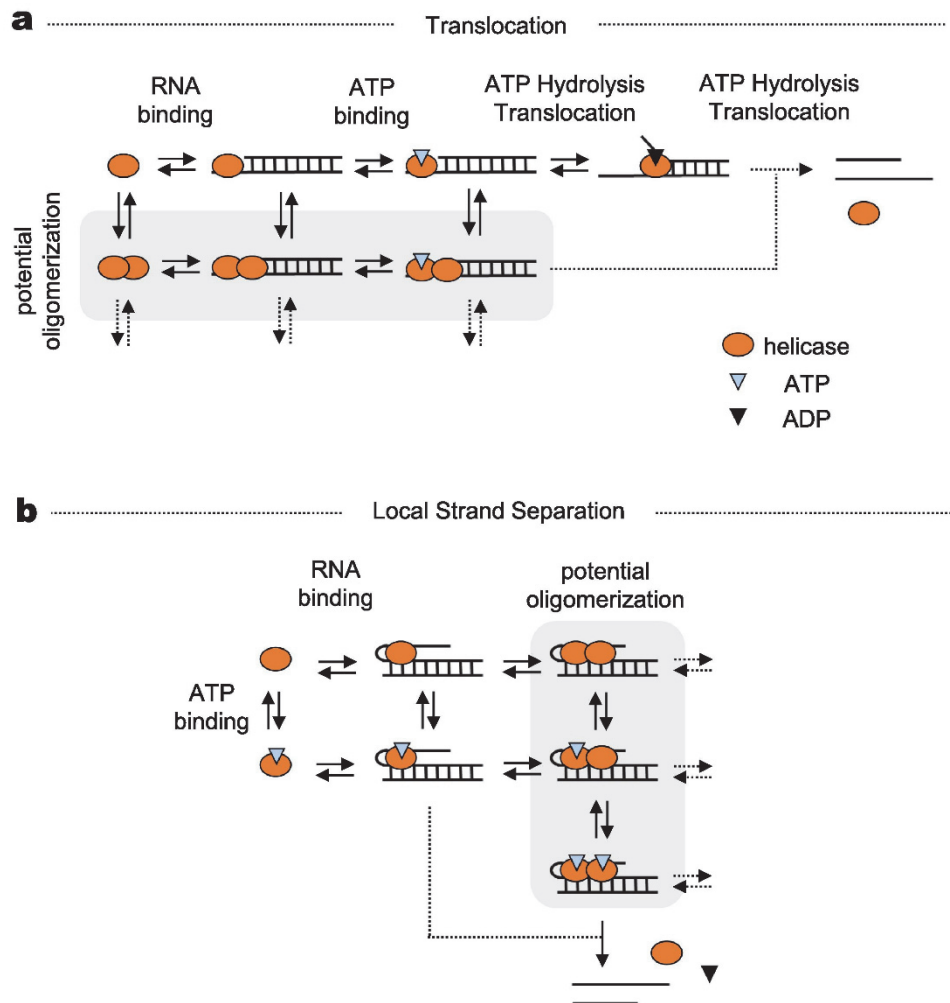


Figure 1.2. Duplex unwinding mechanisms by RNA helicases. (a) RNA unwinding by translocation along one of the RNA strands. Only one pathway for the order of RNA and ATP binding is shown for simplicity, and RNA and ATP can bind in the reverse order. Symbols are explained in the legend. The black lines denote RNA. (b) RNA unwinding by local strand separation. For simplicity, only dimerization is shown as example for oligomerization, but oligomerization of more than two protomers is possible.

RNA helicases require NTPs to exert their enzymatic function, but the coordination between NTP binding and hydrolysis and RNA remodeling varies between different helicase families and can also depend on specific substrates⁶. Of note, most RNA helicases for which links between NTP binding, hydrolysis, and RNA remodeling have been examined, do not require the hydrolysis of NTPs for the actual RNA remodeling step¹². Most DEAD-box helicases that have been tested in this regard require only ATP binding for strand separation¹². ATP hydrolysis promotes dissociation of the protein from the RNA¹². However, not every ATP hydrolysis event leads to dissociation and therefore, ATP hydrolysis can occur without complete strand separation and without the enzyme dissociating from the RNA¹². These non-productive ATP hydrolysis events increase markedly with duplex length and stability^{12,17}. For translocating RNA helicases, NTP hydrolysis promotes movement of the helicase on the RNA, not necessarily the actual strand separation event. However, it is usually challenging to de-convolute translocation and strand separation events^{1,2}.

For RIG-I like helicases, which do not unwind RNA, ATP binding is necessary for activation of RIG-I signaling in response to viral RNA. ATP hydrolysis, on the other hand, promotes rapid dissociation of RIG-I from endogenous, but not from viral RNAs. Thus, ATP ensures that RIG-I is activated only by pathogenic RNAs^{18,19}.

For most RNA helicases, NTP hydrolysis is stimulated by unstructured RNA and often scales with RNA length and other RNA features (e.g. sequence, non-duplex structure)²⁰⁻²². Since NTP hydrolysis can occur without RNA

remodeling, it is challenging to infer RNA remodeling activity from RNA-stimulated NTPase activity. Nevertheless, NTP binding to RNA helicases universally impacts RNA binding and vice versa⁶. In essentially all tested instances, NTP and RNA binding promote the closing of the two helicase domains²³⁻²⁵. Yet, NTP and RNA binding are not always thermodynamically cooperative²⁶.

While some RNA helicases unwind RNA as monomers, several RNA helicases oligomerize to unwind duplexes efficiently^{2,27-32}. For DEAD-box helicases for which oligomerization has been examined, different protomers use NTP differently during the reaction cycle. For example, the yeast DEAD-box helicase Ded1p functions as a trimer, in which two protomers bind and hydrolyze ATP while the third protomer remains subsaturated with respect to ATP, even though this is the active unwinding unit²⁸. This differential ATP utilization across the protomers in an oligomer further complicates the assessment of links between NTPase and strand separation activities.

Moreover, several RNA helicases promote strand annealing, the phenomenological opposite of duplex unwinding^{21,33-36}, as well as non-enzymatic strand exchange, the ATP-independent swapping of basepairing from one complementary strand of RNA to another^{37,38}. Both strand annealing and strand separation or RNA structure resolution can be important for the function of RNA helicases as RNA chaperones^{1,2}.

1.3 DEAD-box RNA helicase architecture

As noted earlier, both SF1 and SF2 helicases contain from 8 to 13 highly conserved helicase motifs within their helicase cores^{1,6}. Differences in the inclusion and amino acid composition of these various motifs underlies the classification of RNA helicases into superfamilies and associated families⁶ (**Fig. 1.1**). Many DEAD-box RNA helicases contain all 13 characteristic helicase motifs within their core, and the family is named for the conserved Asp-Glu-Ala-Asp (DEAD) motif within motif II^{12,39} (**Fig. 1.3**). The helicase motifs are spread across the two RecA-like domains, with the ATP binding cleft forming between the two domains¹². RNA binding occurs via interactions between several helicase motifs and the phosphate backbone of the RNA^{5,12}. Thus, DEAD-box helicases bind RNA with no apparent sequence specificity^{5,12}. Various biochemical studies have delineated which conserved motifs are involved in ATP binding and hydrolysis, RNA binding, and the coordination of these two activities^{6,12} (**Fig. 1.3**).



Figure 1.3. DEAD-box RNA helicase motifs. Schematic of the helicase motif organization of the characteristic DEAD-box RNA helicase DDX3X. Colored boxes depict the conserved motifs important for enzymatic function. Red = ATP hydrolysis. Light blue = RNA binding. Yellow = Communication between ATP hydrolysis and RNA binding sites.

1.4 Biological functions of eukaryotic DEAD-box RNA helicases

DEAD-box RNA helicases comprise the largest helicase family, and thereby play roles in virtually every stage of RNA metabolism, as outlined below (**Fig 1.4**).

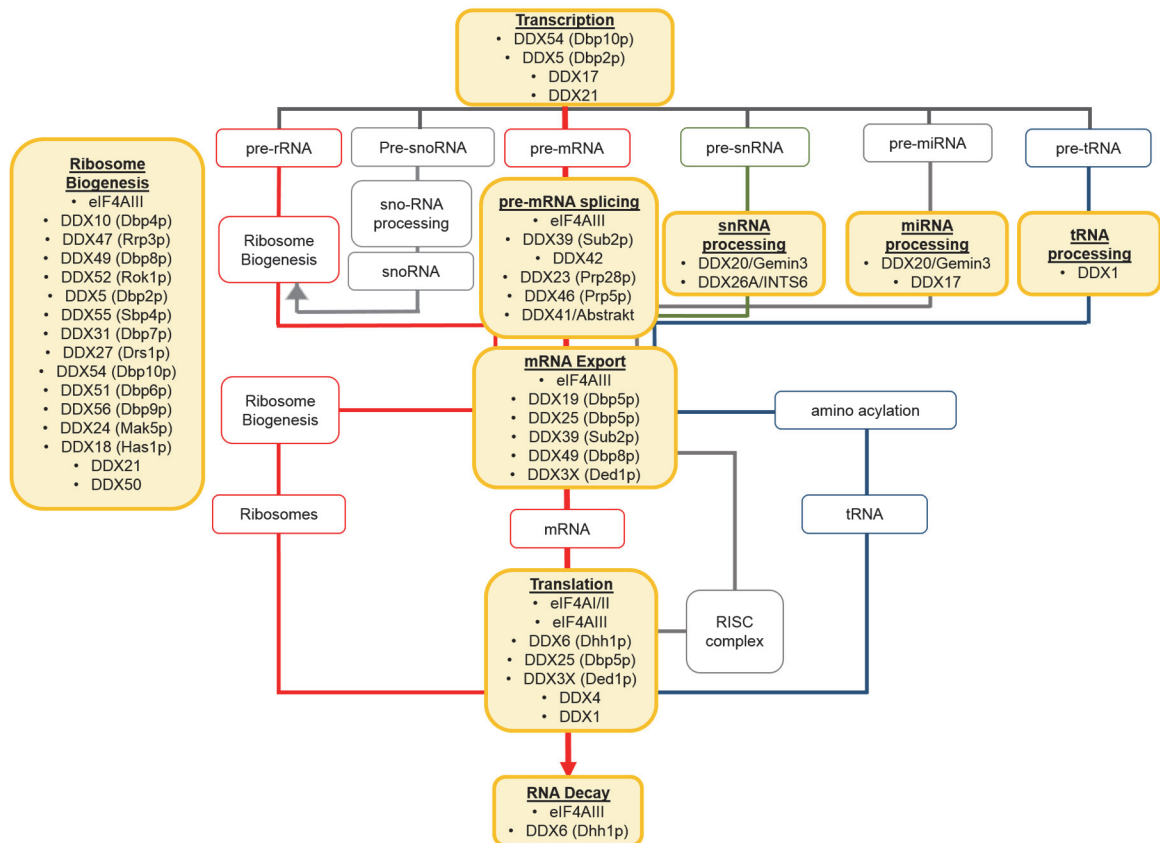


Figure 1.4. DEAD-box RNA helicase functions in RNA metabolism. Simplified schematic of RNA metabolism adapted with permission from Brittany Stawicki and Dr. Eckhard Jankowsky. Stages where DEAD-box RNA helicases are implicated are highlighted in yellow, and the associated DEAD-box RNA helicases are listed. Yeast orthologs are listed in parentheses where relevant.

1.4.1 Transcription

Transcription is the process by which RNA is made from DNA. DEAD-box RNA helicases regulate various aspects of the transcription process. DDX5 (yeast ortholog Dbp2p), DDX17, and DDX54 regulate transcription indirectly via association with epigenetic modifiers such as long noncoding RNAs (lncRNAs) and proteins that remodel chromatin⁴⁰⁻⁴². DDX5/Dbp2p also indirectly regulates transcription by associating with and remodeling R-loops that form on newly transcribed RNA^{43,44}. R-loop formation can stimulate or inhibit transcription, and

proper remodeling of R-loops is required to maintain genomic stability^{43,44}.

DDX5/Dbp2p, DDX17, and DDX54 also regulate transcription directly via their interactions with various transcription factor complexes^{40,45,46}. In addition, DDX21 associates with several promoters to directly regulate the transcription of rRNA and snoRNA⁴⁷.

1.4.2 Pre-mRNA splicing

Pre-mRNA splicing is the process by which introns are removed from pre-mRNAs during their maturation into mRNAs. Several DEAD-box RNA helicases facilitate the rearrangements of the spliceosome, associated small nuclear ribonucleoproteins (snRNPs), and pre-mRNA required for successful pre-mRNA splicing. DDX39A/B (yeast ortholog Sub2p) and DDX46 (yeast ortholog Prp5p) promote assembly of the spliceosome⁴⁸. DDX23 (yeast ortholog Prp28p) coordinates with the Ski2-like helicase Brr2p to remodel the spliceosome into its active conformation⁴⁸. Several RNA helicases from the DEAH-box family then facilitate the catalytic steps of the spliceosome and subsequent spliceosome disassembly⁴⁸. In humans, the DEAD-box RNA helicase DDX42 also promotes spliceosome assembly, while eIF4AIII and DDX41 participate in the catalytic steps performed by the spliceosome⁴⁸.

1.4.3 mRNA export

Pre-mRNAs are transcribed and processed in the nucleus, then packaged into mRNPs and exported into the cytoplasm⁴⁹. DDX39A/B (yeast ortholog Sub2p) recruits Aly (yeast ortholog Yra1p) to nuclear mRNAs, which then recruits the nuclear transport receptors to facilitate mRNA export from the nucleus⁵⁰.

DDX19/DDX25 (yeast ortholog Dbp5p) then remodel the exported mRNP to allow release of the mRNA into the cytoplasm^{51,52}. DDX49 (yeast homolog Dbp8p) also promotes the nuclear export of mRNAs in a splicing-independent manner⁵³. Additionally, the DEAD-box RNA helicases eIF4AIII and DDX3X (yeast ortholog Ded1p) are both implicated in the export of viral mRNAs during infection^{54,55}.

1.4.4 Translation

Translation is the process by which proteins are made from mRNAs. DEAD-box RNA helicases are essential for translation initiation, the process by which the pre-initiation complex forms on the mRNA 5'-UTR and then scans the mRNA to locate the start codon where translation will begin⁵⁶. eIF4AII is a component of the eIF4F translation initiation complex, which recruits the 43S pre-initiation complex to mRNAs to initiate scanning of the mRNA 5'-UTR^{57,58}. DDX3X/Ded1p also associates with the pre-initiation complex near the mRNA entry channel to facilitate scanning by resolving secondary structures in the 5'-UTR⁵⁹⁻⁶². Interestingly, DDX3X appears to be required for efficient translation initiation on a smaller fraction of total transcripts in humans than the fraction of transcripts dependent on the yeast Ded1p for efficient translation^{59,60,63,64}. DDX4/Vasa is a DEAD-box RNA helicase that associates with the translation initiation factor eIF5B to promote translation of transcripts during germ cell development^{65,66}.

In addition to roles in translation initiation, DEAD-box RNA helicases also have other roles associated with translation. Association of the exon junction

complex, which contains eIF4AIII, with mRNAs stimulates translation of bound transcripts⁶⁷. The testis-specific DDX25 (yeast ortholog Dbp5p) promotes translation elongation (the process by which amino acids are incorporated into the nascent polypeptide) during germ cell development⁶⁸. DDX6 (yeast ortholog Dhh1p) interacts with ribosomes to monitor translation efficiency and coordinate mRNA decay of inefficient transcripts⁶⁹. DDX1 coordinates the fatty acid-responsive translation of insulin mRNA⁷⁰. Thus, several DEAD-box RNA helicases are involved in regulating various aspects of translation.

1.4.5 RNA decay

RNA decay constitutes the various pathways by which RNAs are degraded and removed from the cell. Several non-DEAD-box RNA helicases are involved in RNA decay, including the SF1 helicase Upf1p which functions in nonsense-mediated decay⁷¹ (the co-translational decay of mRNAs with premature termination codons^{72,73}), and the Ski2-like helicase Mtr4p that associates with both the TRAMP complex and the nuclear exosome^{74,75} (protein complexes that carry out RNA surveillance and perform 3' to 5' RNA degradation⁷²). As noted above, the DEAD-box RNA helicase DDX6/Dhh1p associates with ribosomes and the mRNA decay machinery to coordinate translation with mRNA decay⁶⁹. Additionally, eIF4AIII enhances mRNA decay as a component of the exon junction complex^{76,77}.

1.4.6 Ribosome biogenesis

Ribosomes are the ribonucleoproteins that perform the process of translation. Ribosomes consist of a small subunit and a large subunit that are

both composed of numerous proteins and RNAs. Ribosome biogenesis (the assembly of ribosomes) is a highly orchestrated process that has been most well characterized in *S. cerevisiae* and requires at least 14 DEAD-box RNA helicases, in addition to three DEAH-box RNA helicases and one Ski2-like RNA helicase^{78,79}. DDX10 (yeast ortholog Dpb4p), DDX49 (yeast ortholog Dbp8p), eIF4AIII, DDX52 (yeast ortholog Rok1p), and DDX47 (yeast ortholog Rrp3p) assist in assembling the small ribosomal subunit^{78,79}. DDX5 (yeast ortholog Dbp2p), DDX51 (yeast ortholog Dbp6p), DDX31 (yeast ortholog Dbp7p), DDX56 (yeast ortholog Dbp9p), DDX54 (yeast ortholog Dbp10p), DDX27 (yeast ortholog Drs1p), DDX24 (yeast ortholog Mak5p), and DDX55 (yeast ortholog Sbp4p) assist in assembling the large ribosomal subunit^{78,79}. DDX18 (yeast ortholog Has1p) assists with the assembly of both the small and large subunits^{78,79}. In humans, DDX21 is involved in rRNA transcription⁴⁷, as well as the recruitment of various late-acting snoRNAs that assist in modification/maturation of the small ribosomal subunit⁸⁰. Additionally, the human DEAD-box RNA helicase DDX50 localizes to nucleoli where ribosome biogenesis occurs, suggesting that it may also play a role in ribosome biogenesis⁸¹.

1.4.7 tRNA processing

tRNAs are highly structured and modified RNAs that deliver amino acids to the ribosome during protein synthesis⁸². DDX1 is a component of the tRNA ligase complex, which facilitates splicing of the 6% of mammalian tRNAs that are expressed from intron-containing transcripts^{83,84}.

1.4.8 snRNA processing

Small nuclear RNAs (snRNAs) are small noncoding RNAs included within spliceosomal small nuclear ribonucleoproteins (snRNPs) that constitute and regulate the spliceosome^{85,86}. The human DEAD-box RNA helicase DDX26A/INTS6 is a component of the integrator complex that processes the 3'-ends of snRNAs⁸⁷. Another human DEAD-box RNA helicase, DDX20/Gemin3, is a component of the survival motor neuron (SMN) complex, which facilitates the assembly of snRNA-containing snRNPs^{86,88}.

1.4.9 miRNA processing

MicroRNAs (miRNAs) are small noncoding RNAs that regulate gene expression within the RNA-induced silencing complex (RISC)^{86,89}. RISC consists of Dicer, Ago2, PACT, and TRBP⁸⁹. miRNAs target the RISC to mRNAs, leading to post-transcriptional gene silencing⁸⁹. DDX20/Gemin3 also associates with a second ribonucleoprotein complex containing the RISC component Ago2 and various miRNAs⁸⁶. Within this complex, DDX20/Gemin3 is thought to promote miRNA maturation and possibly also assist in downstream miRNA target recognition⁸⁶. Additionally, DDX17/p72 binds to precursor miRNAs to facilitate their processing into mature miRNAs^{90,91}.

1.4.10 piRNA processing

Piwi-interacting RNAs (piRNAs) are small noncoding RNAs that bind to and regulate proteins from the piwi subfamily of argonaute proteins^{92,93}. Argonaute proteins are a highly conserved protein family with roles in small non-coding RNA maturation and RNA-based gene silencing⁹⁴. piRNA-piwi

interactions regulate numerous biological processes, including transposon silencing, spermiogenesis, epigenetic regulation of gene expression, and the maintenance of germline stem cells^{92,93}. DDX43 has been implicated as a factor in the biogenesis and amplification of piRNAs⁹⁵.

1.4.11 Mitochondrial RNA metabolism

DDX28 is a mitochondrial DEAD-box RNA helicase that promotes assembly of the mitoribosome⁹⁶. Formation of the mitoribosome is required for the synthesis of the 13 mammalian mitochondrial proteins that facilitate oxidative phosphorylation⁹⁶.

1.5 DEAD-box RNA helicase cofactors

RNA helicases are frequently part of multi-component complexes, including the TRAMP complex, the spliceosome, or the exon junction complex, as discussed above⁹⁷⁻¹⁰⁰. In these complexes, RNA helicases interact with one or several other proteins, and both SF1 and SF2 RNA helicases are thought to invariably interact with other proteins in cells. These protein cofactors are thought to regulate the function of RNA helicases in cells, and many have also been shown to regulate RNA helicase enzymatic activity *in vitro*¹⁰¹⁻¹⁰³. Two families of proteins that recurrently interact with and regulate RNA helicases have been identified: MIF4G proteins and G-patch proteins¹⁰¹. However, not all RNA helicase cofactors belong to these two protein families. Proteins containing the conserved MIF4G-domain interact with and regulate several DEAD-box RNA helicases¹⁰¹. Two well-studied examples are the interaction between eIF4G and eIF4A and the interaction between Gle1 and Dbp5p, both described in greater

detail below. G-patch proteins contain glycine-rich G-patch domains and interact with several DEAD-box RNA helicases to stimulate their ATPase and unwinding activities¹⁰¹. Theoretically, cofactors can alter one or many of the mechanistic steps involved in RNA/RNP remodeling by RNA helicases, as illustrated in **Fig. 1.5**. Specific cofactors that regulate DEAD-box RNA helicases are identified in detail below.

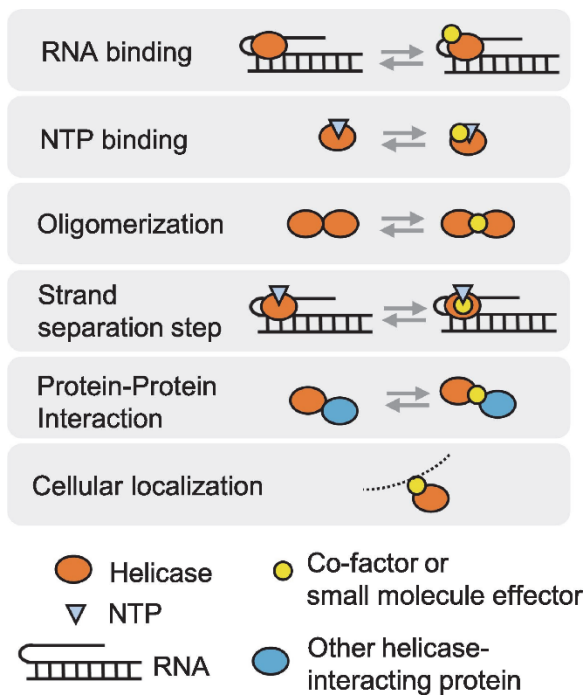


Figure 1.5. Potential cofactor effects. Different possibilities for cofactor impact on helicase activities and cellular functions. Cofactors and small molecule effectors can inhibit or stimulate the respective reaction step, the molecular interaction between the helicase and other factors or cellular compartments, or multiple processes.

1.5.1 eIF4A cofactors

eIF4A is an essential component of the eIF4F complex that initiates translation^{57,58}. The eIF4F complex consists of three eukaryotic translation initiation factors: eIF4A (either the more common isoform I or the less common

isoform II), eIF4E, and eIF4G⁵⁷. On its own, eIF4A is only able to unwind very short duplexes *in vitro*; however, association with the eIF4F complex stimulates eIF4A's unwinding and ATP hydrolysis activities^{104,105}. This stimulation likely assists eIF4A in resolving large and stable mRNA secondary structures during translation initiation. Additional eukaryotic initiation factors eIF4B and eIF4H are also able to interact with eIF4A (or eIF4F) and enhance its unwinding activity *in vitro*, in part by increasing its processivity along RNA substrates^{104,106}. eIF4B and eIF4H both enhance eIF4A activity by increasing eIF4A's affinity for RNA¹⁰⁷, while eIF4F primarily increases eIF4A's activity by maintaining it in an "open" or active conformation and speeding up the rate-limiting phosphate release step¹⁰⁸⁻¹¹⁰. These cofactor interactions with eIF4A have been confirmed to promote efficient translation *in vivo*^{111,112}.

In addition to these activating interactions, eIF4A/II is inhibited by interactions with the tumor suppressor Pcd4 (programmed cell death protein 4)¹¹³. Pcd4 interacts with eIF4A in the cytoplasm, reduces eIF4A interactions with eIF4G, and inhibits eIF4A helicase activity *in vitro*¹¹³. This interaction inhibits translation initiation by reducing RNA binding to eIF4A¹¹³⁻¹¹⁵.

1.5.2 Ded1p cofactors

The yeast DEAD-box RNA helicase Ded1p interacts with eIF4A and eIF4G, which both stimulate Ded1p helicase unwinding activity *in vitro*^{116,117}. Ded1p alone functions as a trimer to unwind RNA helicases *in vitro*, but forms a 1:1 complex with eIF4A and eIF4G, wherein Ded1p is the active unwinding unit^{28,116,118}. This Ded1p-eIF4A-eIF4G complex has faster unwinding rate

constants than Ded1p alone, due to direct effects of eIF4A and eIF4G on the strand separation step during unwinding¹¹⁶. These interactions are important *in vivo*, where Ded1p associates with the 43S pre-initiation complex to promote scanning along mRNAs with structured 5'-UTRs^{59,63,64}. Ded1p inactivation leads to pre-initiation complex stalling upstream of mRNA secondary structures⁵⁹. This stalling results in translation initiation from near-cognate start codons when they are present upstream of the secondary structure⁵⁹.

Ded1p also interacts with the protein Gle1p, which inhibits Ded1p ATPase activity *in vitro* and translation initiation *in vivo*¹¹⁹. Gle1p inhibits Ded1p activity by reducing its RNA affinity¹²⁰.

1.5.3 Dbp5p cofactors

The yeast DEAD-box RNA helicase Dbp5p plays a key role in mRNA export from the nucleus, where it associates with the nuclear pore complex to remodel exported mRNPs allowing unidirectional translocation of mRNA into the cytoplasm^{51,52}. Dbp5p's activity at nuclear pore complexes during mRNA export is enhanced by several cofactors. Gle1p bound to inositol-hexakisphosphate (InsP₆) stimulates Dbp5p ATP hydrolysis activity *in vitro* by increasing both ATP binding and the rate-limiting release of free phosphate¹²¹⁻¹²⁴. This stimulation of ATP hydrolysis ultimately increases recycling of Dbp5p at the nuclear pore¹²⁵. Dbp5p recycling at the nuclear pore is also enhanced by the cofactor Nup159. Nup159 recruits Dbp5p to the nuclear pore and assists in the release of ADP from Dbp5p during Dbp5p recycling^{124,126,127}. This cofactor-stimulated cycling of Dbp5p through the ATP hydrolysis cycle is required to promote release of

mRNAs from RNPs at the nuclear pore and their subsequent transport into the cytoplasm^{122,124}.

1.5.4 Dbp2p cofactors

Dbp2p has roles in transcription and ribosome biogenesis^{40,78,79}. In addition to promoting transcription via interactions with lncRNAs and transcription factors, Dbp2p co-transcriptionally recruits Yra1p, Nab2p, and the nuclear export receptor Mex67p onto nascent mRNAs to form mRNPs¹²⁸. Co-transcriptional mRNP formation stabilizes nascent mRNAs and orchestrates subsequent mRNA processing steps¹²⁹. Dbp2p's role in nascent mRNP formation is regulated by Yra1p. Yra1p binding to Dbp2p inhibits its RNA duplex unwinding activity *in vitro* by preventing Dbp2p association with ssRNA^{128,130}. This Yra1p-mediated reduction in Dbp2p ssRNA binding prevents the over-accumulation of Dbp2p on mRNA and subsequent alterations in mRNP formation and mRNA stability^{128,130}.

1.5.5 eIF4AIII cofactors

eIF4AIII is a component of the exon junction complex, a protein complex that is deposited on mRNAs during splicing and remains bound to the mRNA until its translation¹³¹. By this presence on mRNA throughout its lifecycle, the exon junction complex exerts influence on pre-mRNA splicing, mRNA export, translation, and mRNA decay¹³¹. The core exon junction complex that remains stably bound to mRNA consists of the proteins MAGOH, Y14, eIF4AIII, and MLN51¹³². Direct interactions between eIF4AIII, MAGOH, and Y14 inhibit eIF4AIII's ATP hydrolysis activity, allowing eIF4AIII to serve as a clamp that anchors the exon junction complex on mRNAs^{132,133}.

1.5.6 Dbp8p cofactors

The yeast DEAD-box RNA helicase Dbp8p plays a role in ribosome biogenesis^{78,79}. During its association with pre-rRNA, Dbp8p interacts with the nucleolar protein Esf2p¹³⁴. *In vitro*, Esf2p enhances Dbp8p ATP hydrolysis activity, though the exact biological function of this interaction remains unclear¹³⁴.

1.5.7 Vasa cofactors

Vasa is a DEAD-box RNA helicase that regulates translation during germ cell development^{65,66}. Vasa function is regulated by widely conserved interactions with LOTUS domain-containing proteins^{135,136}. LOTUS domain-containing proteins are conserved from bacteria to eukaryotes, bind to G4 quadruplex RNA, and have various functions during development/gametogenesis¹³⁷. LOTUS domain-containing proteins enhance vasa ATP hydrolysis activity *in vitro* and recruit vasa to germ granules that form during germ cell development^{135,136}.

1.6 DEAD-box RNA helicases in human disease

Given their roles in virtually all aspects of RNA metabolism (**Fig. 1.4**), dysregulation of DEAD-box RNA helicases contributes to the development of numerous human diseases. Mutations in eIF4AIII lead to the rare autosomal recessive disorder Richieri-Costa-Pereira syndrome characterized by craniofacial malformations and limb defects^{138,139}. Mutations in DDX59 lead to the rare autosomal recessive disorder orofacial digital syndrome type 5 characterized by polydactyly and oral malformations¹⁴⁰. Mutations in several DEAD-box RNA helicases lead to neurodevelopmental disorders and intellectual disability, including DDX6, DDX54, DDX23, and DDX3X¹⁴¹⁻¹⁴⁴. Mutations in DDX3X can

also cause Toriello-Carey syndrome characterized by craniofacial malformations, brain abnormalities, heart defects, hypotonia, and intellectual disability^{145,146}. Meanwhile, dysregulation of DDX5 can contribute to the development of polycystic kidney disease and myotonic dystrophy¹⁴⁷⁻¹⁴⁹. In addition to these genetic diseases, virtually all DEAD-box RNA helicases exhibit altered expression or recurrent mutations in human tumor samples, with several DEAD-box RNA helicases being dysregulated in more than 10 cancer types: eIF4AII, eIF4AIII, DDX39, DDX3X, and DDX5 (see **Appendix 1**).

Chapter 2

Introduction to RNA helicases in biomolecular condensates

2.1 Overview of biomolecular condensates

Biomolecular condensates are cellular organelles that lack a defined outer membrane and organize cellular processes by concentrating specific proteins and nucleic acids together¹⁵⁰⁻¹⁵². Due to their lack of a membrane, condensates quickly exchange components with the surrounding cellular cytosol or nucleoplasm^{150,152}. Thus, while condensates often contain a set of core proteins and nucleic acids essential for their formation, the entire proteome/transcriptome associated with a condensate is also comprised of proteins and nucleic acids that transiently associate with the condensate¹⁵². Given their ability to concentrate various proteins/nucleic acids together, biomolecular condensates can either enhance and/or add specificity to catalytic processes by localizing enzymes with a subset of their ligands or inhibit catalytic processes by sequestering key proteins and nucleic acids¹⁵⁰⁻¹⁵². Sequestration of nucleic acids and proteins within condensates may also serve as a way to store/protect biomolecules¹⁵⁰⁻¹⁵². Finally, since biomolecular condensates are not membrane-bound and cellular molecules can freely interact with and diffuse into them, condensates provide a mechanism for cells to rapidly respond to environmental changes¹⁵⁰⁻¹⁵².

2.1.1 Types of biomolecular condensates

Several different types of biomolecular condensates have been identified, with each condensate having a specific composition that varies over time and in response to stimuli^{150,152}. A wide variety of condensates form within the nucleus,

where they either regulate RNA/RNP processing or gene expression. One well-known nuclear condensate is the nucleolus, the site of rRNA and ribosome biogenesis^{153,154}. Numerous studies have shown that the nucleolus is a dynamic structure that contains several phase-separated sub-compartments where various stages of ribosome biogenesis take place¹⁵⁴⁻¹⁵⁸. Another condensate involved in RNA processing within the nucleus is Cajal bodies, where snRNP and snoRNP biogenesis and processing occur^{153,159-161}. Paraspeckles are nuclear RNA-protein condensates composed of more than 40 RNA binding proteins that assemble along the NEAT1 lncRNA^{160,162}. By sequestering proteins and RNAs, paraspeckles regulate post-transcriptional gene expression^{153,162}.

Other nuclear condensates regulate transcription, including nuclear speckles^{153,163,164}, PcG bodies that contain condensates of chromatin-modifying polycomb group proteins¹⁶⁵⁻¹⁶⁷, and PML bodies localized around the PML protein^{153,160,168,169}. Heterochromatin itself, the compact translationally-repressed form of chromatin, is thought to be a biomolecular condensate whose rapid formation and dissolution is regulated by various heterochromatin proteins^{150,170-175}. Furthermore, the clusters of proteins and nucleic acids at sites of active transcription and DNA damage repair also constitute biomolecular condensates^{150,152,170,176-183}.

Cytoplasmic biomolecular condensates primarily regulate the translation, stability, and localization of RNAs. Germ granules are widely conserved ribonucleoprotein (RNP) granules that regulate mRNA translation, stability, and localization within germ cells¹⁸⁴⁻¹⁸⁷. This spatiotemporal control of mRNA

orchestrates the correct timing of protein expression during germ cell development¹⁸⁸. RNA transport granules are biomolecular condensates that allow spatiotemporal control of translation within cells, most notably within large cells like neurons, where specific proteins are made in different regions of the cell^{150,152,189-191}. Cytoplasmic biomolecular condensates also participate in cell-cell communication. Pre-/post-synaptic neuron densities and membrane-associated/cytoplasmic signaling clusters are two types of biomolecular condensates directly involved in cell signaling^{150,152}.

P-bodies are RNP condensates containing RNA decay proteins and translationally-repressed mRNAs that form in yeast and mammalian cells¹⁹². In yeast, P-bodies are highly enriched for 7 RNA binding proteins (RBPs) involved in RNA decay: Dcp2p, Edc3p, Lsm1p, Pat1p, Dhh1p, Upf1p, and Xrn1p¹⁹³. However, since decay intermediates are not enriched in P-bodies, it remains unclear whether P-bodies are sites of active RNA decay or sites of storage for inactive decay enzymes and translationally-repressed mRNAs¹⁹². *In vitro* reconstituted P-bodies inhibit the decapping activity of Dcp1p/Dcp2p, but allow for ~90-fold increases in decapping activity when the decapping activator Edc3p is added (compared to the 3-fold increases upon Edc3p addition in solution biochemical reactions)^{194,195}. These *in vitro* results suggest that while P-bodies may primarily act as storage sites for inactive decay enzymes, they also allow the rapid activation/regulation of RNA decay.

Stress granules are another class of cytoplasmic ribonucleoprotein condensate that contain translationally-repressed mRNAs. Stress granules form

exclusively in response to inhibited translation initiation, which physiologically occurs downstream of eIF2 α phosphorylation in the integrated stress response¹⁹⁶. Thus, stress granules typically form in response to cellular stress; however, pharmacological inhibition of translation initiation or the overexpression of essential stress granule proteins (CAPRIN1, G3BP1/2, TIA1, TTP, FMRP, etc.) also induces stress granule formation^{196,197}. Interestingly, stress granule composition varies with the type of inducing stress¹⁹⁸. Stress granules form downstream of inhibited translation initiation after the elongating ribosomes run off the transcripts, releasing mRNAs from polysomes^{196,197,199}. These free mRNAs and their associated stalled translation initiation complexes are then bound by numerous RBPs in the cytoplasm, resulting in the formation of stress granules^{196,197,199}. Functionally, stress granules promote cell survival during acute stress and then dissolve during stress recovery¹⁹⁹.

2.1.2 Biomolecular condensates in disease

Dysregulation of biomolecular condensates is associated with the development of a variety of human diseases^{150,197}. Numerous neurodegenerative diseases, including amyotrophic lateral sclerosis (ALS), frontotemporal dementia, Huntington disease, and Alzheimer's disease, have all been linked to specific protein mutations that shift condensates out of a liquid-like state into a less dynamic solid/fibrillary state^{150,197}. Specific proteins in which these pathogenic mutations have been identified include the RNA binding proteins TDP43, FUS, TIA1, hnRNPA1, and G3BP1^{150,197}.

Several biomolecular condensates have also been implicated in the development of cancer. Nuclear paraspeckles and the associated NEAT1 lncRNA have been directly linked to tumorigenesis in mice, where NEAT1 knockdown prevents the development of chemically-induced skin tumors²⁰⁰. Additionally, several instances have been identified where cancer-associated mutations and/or fusion proteins promote tumorigenesis by altering condensate formation and the associated gene expression and/or cellular signaling pathways^{200,201}. Similarly the formation of stress granules is observed in various cancers, where they promote cancer cell survival in the face of metabolic stress and treatment with radio- and chemotherapies^{196,197,201}. The exact role of biomolecular condensate dysregulation in the development of cancer remains an ongoing area of research²⁰⁰.

Biomolecular condensates are also heavily involved in the innate immune response to viral infection. cGAS is a cytosolic protein that binds dsDNA produced by viral infection or nuclear damage²⁰². dsDNA binding activates cGAS, leading to signaling cascades that ultimately induce expression of interferons and proinflammatory cytokines²⁰². dsDNA binding also promotes the formation of cGAS-containing biomolecular condensates, which further potentiates downstream proinflammatory signaling cascades²⁰³⁻²⁰⁵. Formation of these cGAS condensates is blocked by herpesvirus²⁰².

Stress granules are also frequently disrupted by viruses²⁰⁶. Numerous viruses either sequester/degrade essential stress granule proteins to disrupt stress granule formation and/or target PKR to prevent eIF2 α phosphorylation²⁰⁶.

This disruption of stress granules likely serves to free the host translation initiation machinery to participate in viral replication²⁰⁷. Additionally, several antiviral signaling proteins, including PKR, RIG-I, and MDA5, localize to stress granules following viral infection, which may potentiate proinflammatory signaling cascades similar to observations of cGAS condensates²⁰⁷.

2.2 Formation of biomolecular condensates

Biomolecular condensates form via liquid-liquid phase separation (LLPS), a process in which a multi-component liquid de-mixes into two distinct phases: a dense phase within the condensate and a surrounding dilute phase, similar to the formation of oil droplets in water¹⁵⁰. Biomolecular condensates exhibit many liquid-like qualities (fusion, exchange of molecules with surroundings on the second to minute timescale, dripping, etc.) and are thus dynamic structures that can form, change, and dissolve rapidly in response to cellular conditions¹⁵⁰⁻¹⁵². Changes in cellular temperature, pH, ion concentration, osmolyte concentration, and/or metabolite (eg. ATP, etc.) concentration can all impact condensate formation and dissolution¹⁵⁰.

Cellular LLPS is largely driven by multivalent interactions that primarily occur between proteins with multiple binding domains and/or proteins with intrinsically disordered regions (IDRs)¹⁵². Proteins with multiple binding domains are able to form multiple intra- and intermolecular interactions with their ligands and binding partners. Intrinsically disordered proteins have low sequence complexity and consist of repeated sequence elements that can participate in weak multivalent intermolecular interactions¹⁵². IDRs are enriched for glycine,

polar amino acids (serine, glutamine, asparagine), aromatic amino acids (phenylalanine, tyrosine), and/or charged amino acids (lysine, arginine, glutamate, aspartate)¹⁵². Given the relative lack of hydrophobic amino acids in IDRs, these regions are unable to form long-range hydrophobic interactions required for folding into stable tertiary structures²⁰⁸. The repetition of charged/polar/aromatic residues in IDRs leads to a variety of weak intermolecular interactions: cation- π interactions between aromatic and charged amino acids, dipolar interactions between polar amino acids, and/or charge-charge interactions between blocks of positively- and negatively-charged amino acids¹⁵². These multivalent interactions result in the formation of large oligomers that have reduced solubility, promoting liquid-liquid phase separation¹⁵².

As detailed in Section 2.1.1, the large majority of biomolecular condensates contain RNA, which can directly impact LLPS¹⁵⁰⁻¹⁵². RBPs can bind to RNA at specific binding sites and/or nonspecifically, leading to the concentration of RNA and RBPs together in a multivalent interaction network that promotes LLPS¹⁵¹. RNA can also interact with itself, providing additional sites of multivalent, LLPS-promoting interactions¹⁵¹. Furthermore, since RNA is negatively charged, RNA contributes to charge-charge interactions that promote LLPS^{151,152}. Interestingly, while low concentrations of RNA support condensate formation via multivalent charge-charge interactions and the recruitment/concentration of numerous RBPs, high RNA concentrations dissolve condensates, likely via charge inversion and charge repulsion effects^{151,209}.

The inclusion of RNA in condensates affects the formation, composition, and material properties of biomolecular condensates¹⁵¹. Several characteristics of a given RNA, including the length, structure, and/or modification status, all contribute to the effects that a given RNA has on a condensate¹⁵¹. Similar dynamic characteristics of condensate-associated proteins, including post-translational modifications and interactions with protein chaperones and/or the proteasome, also impact the properties and formation of biomolecular condensates¹⁵⁰.

2.3 RNA helicases in biomolecular condensates

As described earlier, RBPs are a frequent component of biomolecular condensates. Interestingly, RNA helicases are particularly enriched in condensates, with more than 1/3 of DEAD- and DEAH-box helicases having LLPS-promoting IDRs in their N- and/or C-terminal extensions²¹⁰. The ability of RNA helicases to undergo LLPS also appears to be widely conserved across eukaryotes²¹⁰. It's been suggested that the RNP remodeling and ATPase activities of RNA helicases allows them to regulate the dissolution of biomolecular condensates (such as stress granules and P-bodies) in an ATP-dependent manner²¹⁰. Similarly, the DEAD-box RNA helicase eIF4A, which lacks IDRs but associates with stress granules as a component of the translation initiation machinery, functions as an RNA chaperone to reduce stress granule formation in human cells^{210,211}. DDX19 and DDX39 have been suggested to have similar RNA chaperone activities²¹¹.

Several other RNA helicases are directly implicated in the formation and/or remodeling of biomolecular condensates. DDX6 (yeast ortholog Dhh1p) and Mov10 (an SF1 helicase) are found in P-bodies²¹². DDX6/Dhh1p is one of the most highly enriched proteins in P-bodies¹⁹³. Interactions between Dhh1p and Pat1p are required for P-body assembly, while Dhh1p ATPase activity is required for P-body disassembly^{213,214}. The MIF4G protein Not1p stimulates Dhh1p ATPase activity to promote condensate dissolution²¹⁴. Dhh1p's role in regulating P-body dynamics appears to be conserved, as the *C. elegans* ortholog CGH-1 prevents the transition of P-bodies from a liquid to solid state during oogenesis²¹⁵. Recently, missense mutations in the human ortholog DDX6 that prevent P-body formation have been found to cause neurodevelopmental disorders in humans¹⁴¹.

DDX3X (yeast ortholog Ded1p), DDX1, and DHX36 all localize to stress granules^{212,216}. DDX3X/Ded1p are essential stress granule components that undergo robust LLPS *in vitro*^{210,217,218}. Overexpression of DDX3X/Ded1p induces stress granule formation, while DDX3X/Ded1p depletion reduces stress granule formation^{219,220}. In yeast, Ded1p facilitates the efficient translation of many housekeeping genes, and following Ded1p sequestration within stress granules, translation of these housekeeping genes decreases while the translation of stress-responsive transcripts is maintained²¹⁷. Thus, the formation of Ded1p-containing stress granules promotes the switch to pro-survival stress-responsive gene expression programs²¹⁷. In human macrophages, DDX3X can either associate with stress granules or the pro-pyrototic inflammasome to promote

cell survival or cell death, respectively²²¹. Thus, stress granule formation promotes cell survival by sequestering DDX3X²²¹. Interestingly, several recurrent DDX3X missense mutations that induce constitutive stress granules occur in cancer and neurodevelopmental disorders^{62,222-224}. In the setting of neurodevelopment, this constitutive stress granule formation is pathogenic, as patients with granule-inducing mutations have more severe clinical phenotypes than patients with DDX3X haploinsufficiency²²⁴. The pathogenicity of these aberrant stress granules in the setting of cancer is less clear.

DDX4/Vasa, DDX25/GRTH, and ZNFX-1 (an SF1 helicase) are found in germ granules^{212,225}. DDX25/GRTH is an essential component of chromatoid bodies, a type of germ granule that stores translationally-repressed transcripts during mammalian spermatogenesis^{187,188}. Mutation of DDX25/GRTH leads to reduced chromatoid body formation and male sterility in mice and humans¹⁸⁸. In *C. elegans*, ZNFX-1 associates with perinuclear germ granules and facilitates transgenerational inheritance of gene silencing by small noncoding RNAs²²⁵⁻²²⁷. DDX4/Vasa is a canonical component of germ granules that is widely conserved in metazoans¹⁸⁷. DDX4/Vasa has intrinsically disordered N- and C-terminal extensions that allow its LLPS *in vitro* and promote the formation of germ granules *in vivo*^{228,229}. DDX4/Vasa loss results in germ granule disruption and male/female sterility²²⁸.

As detailed here, RNA helicases are intricately involved in the formation and regulation of biomolecular condensates. Dysregulation of RNA helicases can

disrupt condensate formation, leading to wide-reaching effects on gene expression and RNA processing, with many of these effects resulting in disease.

Chapter 3

Introduction to the DEAD-box RNA helicase DDX3X

My thesis work focuses on the DEAD-box RNA helicase DDX3X and the functional impacts of its interaction with a viral protein. As detailed below, DDX3X is a highly conserved RNA helicase with involvement in several human diseases.

3.1 DDX3X structure and enzymatic activity

The DEAD-box RNA helicase DDX3X (yeast ortholog Ded1p) is highly conserved across eukaryotes³⁹. DDX3X contains the conserved DEAD-box helicase core with characteristic enzymatic motifs (**Fig. 3.1**)^{29,39,230}. Extending from both the N- and C-terminal ends of the helicase core, DDX3X has 100 – 200 amino acid long intrinsically disordered tails (**Fig. 3.1**)^{29,39,230}. Removal of these disordered extensions results in nearly complete loss of DDX3X catalytic activity *in vitro*, with inclusion of truncated N- and C-terminal extensions (amino acids 132-181 and 545-607) restoring some, but not all, of the helicase activity²³⁰.

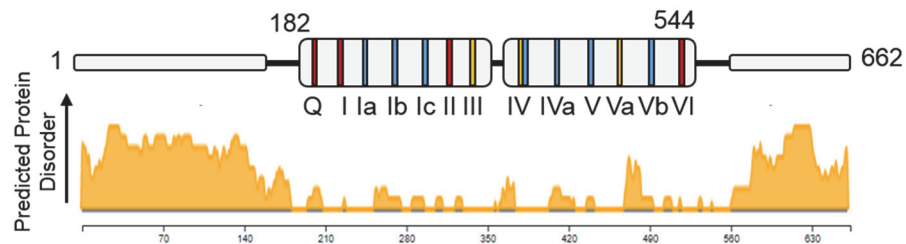


Figure 3.1. DDX3X architecture. Schematic of DDX3X helicase architecture overlaid with a plot of predicted protein disorder. The conserved helicase core extends from residues 182 to 544. Colored boxes depict the conserved motifs important for enzymatic function. Red = ATP hydrolysis. Light blue = RNA binding. Yellow = Communication between ATP hydrolysis and RNA binding sites. Plot of predicted protein disorder generated by MobiDB 3.0²³¹.

The characteristic DEAD-box RNA helicase activities (RNA duplex unwinding and ATP hydrolysis) of DDX3X and Ded1p have been characterized *in vitro*²¹. Both DDX3X and Ded1p unwind RNA duplexes with 5'- or 3'-ssRNA overhangs and have higher functional affinities for duplexes with single-stranded overhangs of at least 25 nt^{21,232}. However, unlike Ded1p, DDX3X displays a strong preference for substrates with 3'-ssRNA overhangs²¹. For both helicases, the strand separation step is impacted by duplex stability, with RNA unwinding rate constants decreasing as duplex stability increases²¹. Both helicases are also able to unwind RNA-DNA hybrid duplexes, but cannot resolve DNA-DNA duplexes²¹. Unwinding activity by both helicases requires ATP binding, with essential contacts occurring at the N6 amino group and N7 position on the adenine base²¹. Thus, other nucleotides (CTP, UTP, GTP) are unable to promote DDX3X/Ded1p-mediated RNA unwinding²¹.

Both helicases have limited ATPase activity in the absence of oligonucleotides²¹. The ATPase activity of Ded1p is optimally stimulated by the presence of RNA duplexes or RNA-DNA duplexes with ssRNA overhangs²¹. Patterns of oligonucleotide stimulation for DDX3X's ATPase activity are similar, except that RNA-DNA duplexes with a DNA overhang stimulate DDX3X's ATPase activity to the same level as RNA-RNA duplexes and RNA-DNA duplexes with RNA overhangs²¹. ssRNA also stimulates DDX3X and Ded1p ATPase activity; however, ssRNA stimulates DDX3X/Ded1p ATPase activity approximately half as much as dsRNA²¹. One final difference between DDX3X and Ded1p *in vitro* enzymatic activities is their ability to promote strand

annealing. Ded1p greatly enhances RNA annealing in the absence of ATP (~ 3 orders of magnitude above annealing rates seen in the absence of helicase), while DDX3X has very weak RNA annealing activity (~ 2-fold increase compared to annealing in the absence of helicase)²¹.

Despite the slight differences between DDX3X and Ded1p enzymatic activities detailed above, both DDX3X and Ded1p function as oligomers to unwind RNA duplexes *in vitro*^{21,28,230}. This oligomeric activity has been characterized in detail for unwinding of an RNA-RNA duplex with a ssRNA overhang by the Ded1p trimer²⁸. Two units of Ded1p bind to a region of ssRNA to facilitate loading of a third unit onto a nearby dsRNA²⁸. This third unit of Ded1p is the active unwinding unit²⁸. Similar to other DEAD-box RNA helicases, ATP binding is required for local strand separation to occur, while ATP hydrolysis promotes Ded1p release from the RNA²⁸. Interestingly, ATP utilization is different for the various monomers within the trimer²⁸. The ATP affinity of the unwinding unit is weaker than for the two loading units, and ATP binding across the two loading units is anti-cooperative²⁸. Thus, the preferred trimeric state is one in which only one of the two loading units is bound to ATP²⁸. This state likely facilitates trimerization by increasing the amount of time the two loading units are bound to the ssRNA and able to recruit a third unit of Ded1p²⁸. Importantly, ATP binding and hydrolysis are not always coupled to productive unwinding; cycles of futile RNA binding and ATP hydrolysis without unwinding can also occur. Finally, while a region of ssRNA adjacent to the dsRNA duplex promotes Ded1p trimer formation and enhances RNA unwinding activity, it's not required for these two

processes; Ded1p also oligomerizes to unwind blunt RNA duplexes lacking ssRNA overhangs²³².

Several lines of evidence indicate that DDX3X oligomers function in a similar manner. RNA unwinding rate constants for both DDX3X and Ded1p exhibit a sigmoidal dependence on helicase concentration with Hill coefficients around $H = 3$ ^{21,28}. Formation of the active Ded1p trimer was found to depend on Ded1p's disordered N- and C-terminal extensions^{28,116}. The minimal unwinding unit of DDX3X containing the truncated N- and C-terminal extensions also demonstrates a sigmoidal relationship between DDX3X concentration and RNA unwinding rate constants with a Hill coefficient of approximately $H = 2$ ^{29,230}. This finding implies that the loss of enzymatic activity when DDX3X's N- and C-terminal extensions are completely removed may be due to the loss of oligomerization, with the truncated extensions restoring some of this ability²³⁰.

Crystal structures are available for the minimal unwinding unit of DDX3X in both the unbound/apo state, the RNA-bound pre-unwinding state, and the ADP-bound state^{29,230,233}. In the RNA-bound structure, two units of DDX3X are bound to a 26 bp dsRNA duplex in the absence of ATP or ATP analogs²⁹. The RecA-like domains of each helicase align so that both domain 1 regions are on one side of the duplex and both domain 2 regions are on the other side of the duplex (**Fig. 3.2**). The two DDX3X units primarily interact with opposite strands of the RNA duplex, but domain 2 of each DDX3X interacts with both strands²⁹. The two DDX3X units align with the entire length of the 26 bp 2-turn RNA duplex, providing structural insight into the inability of DEAD-box helicases to unwind

longer duplexes (**Fig. 3.2**)^{29,37}. While DDX3X (and Ded1p) optimally unwind RNA duplexes with ssRNA overhangs as oligomers *in vitro*^{21,28}, Ded1p is also thought to oligomerize to unwind blunt RNA duplexes²³², in agreement with the mode of DDX3X activity suggested by the crystal structure of truncated DDX3X (**Fig. 3.2**). Finally, in agreement with the lack of sequence specificity for DEAD-box helicases, DDX3X primarily interacts with the RNA phosphate backbone and 2'-OH groups²⁹.

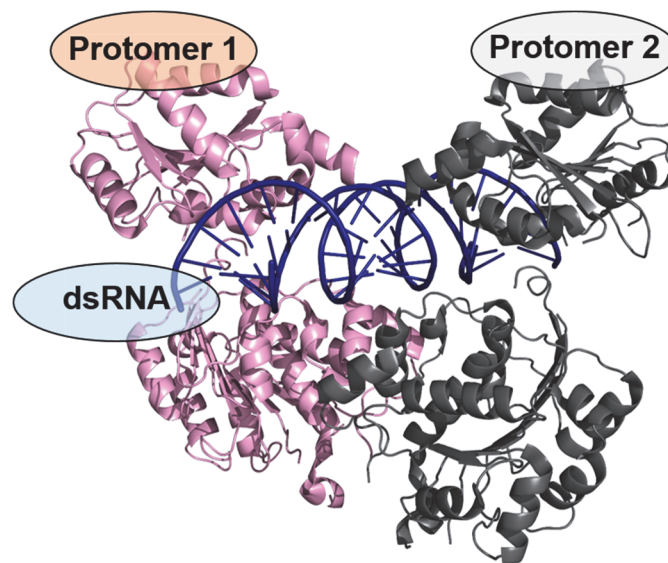


Figure 3.2. RNA-bound DDX3X crystal structure. Crystal structure showing two truncated DDX3X proteins (residues 132-607) bound to a 26 bp dsRNA duplex in the pre-unwinding state. One unit of DDX3X is depicted in light pink and the other unit of DDX3X is depicted in dark gray. The dsRNA duplex is depicted in dark blue. PDB: 6O5F. Figure is modified from²⁹ under the terms of the Creative Commons License (<http://creativecommons.org/licenses/by/4.0/>).

Many insights into the cooperative mechanism of RNA unwinding by DDX3X become clear after comparing this pre-unwinding DDX3X structure with 3 other helicase structures: (1) the unbound/apo DDX3X structure, (2) an ADP-bound DDX3X structure, and (3) a post-unwinding structure of the highly similar

DEAD-box RNA helicase DDX4/Vasa bound to ssRNA and the nonhydrolyzable AMPPNP (**Fig. 3.3**)^{29,230,233,234}. First, many of the contacts between one unit of DDX3X and its bound RNA strand pre-unwinding are maintained in the post-unwinding state²⁹. Second, many conformational changes occur within the helicase core throughout the catalytic cycle. The second RecA-like domain rotates by 180° when it binds the dsRNA duplex, then again rotates another 180° to perform local strand separation²⁹. This structural model supports the functional kinetic data indicating DDX3X oligomerization. Each unit of DDX3X within the dimer remains bound to its strand of the RNA duplex and pries them apart when rotating from the pre- to post-unwinding state²⁹.

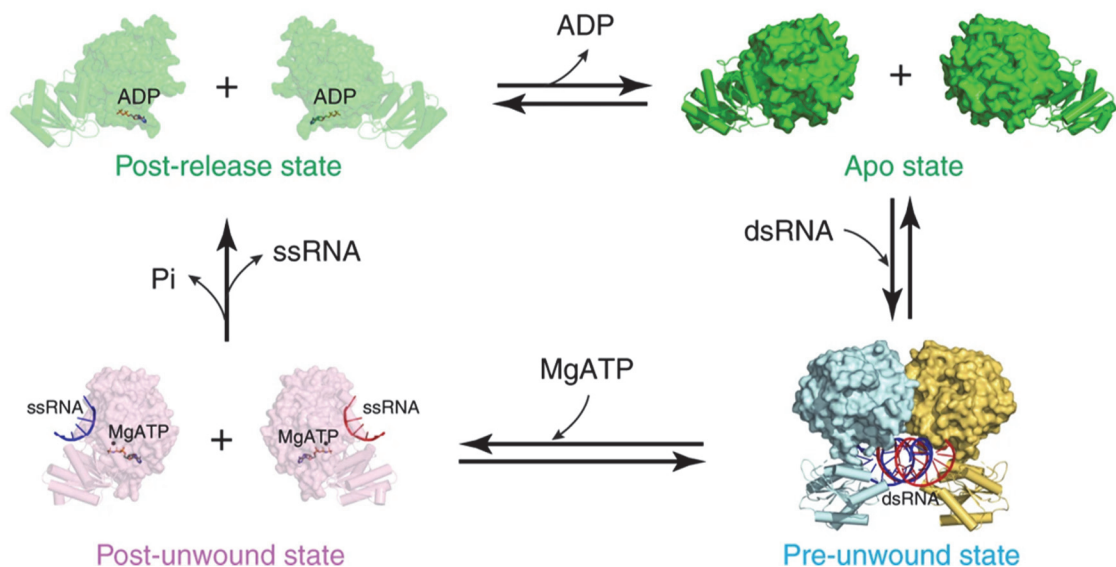


Figure 3.3. Structural model for cooperative RNA duplex unwinding by the minimal DDX3X unwinding unit dimer. Helicase domain 1 of each monomer is represented as a molecular surface. Helicase domain 2 of each monomer is represented as cartoons. Unbound/apo state PDB: 5E71. Pre-unwound state PDB: 6O5F. Post-unwound state PDB: 2DB3. Post-release state PDB: 4PXA. All structures are of the DDX3X helicase core except for the post-unwound state, which is the closely related DDX4/vasa RNA helicase. Figure is adapted from²⁹ under the terms of the Creative Commons License (<http://creativecommons.org/licenses/by/4.0/>).

While this mode of DDX3X unwinding appears to be in conflict with the above-described kinetically-determined mechanism of RNA duplex unwinding by the yeast Ded1p, wherein one protomer of Ded1p is the active unwinding unit²⁸, there are several possible explanations. First, the above-described kinetic mechanism was determined for unwinding of a dsRNA duplex with a ssRNA overhang²⁸; however, the solved RNA-bound DDX3X crystal structure (**Fig. 3.2, 3.3**) is for a blunt RNA duplex. *In vitro* data suggests that Ded1p also functions as an oligomer to unwind blunt RNA duplexes, even though there is no ssRNA to facilitate formation of the trimer²³². This mechanism of blunt RNA unwinding by Ded1p has not been as thoroughly investigated, and could potentially require an alternative distribution of activities across the Ded1p oligomer than those observed for unwinding of an RNA duplex with an ssRNA overhang. Additionally, the RNA-bound DDX3X crystal structure (**Fig. 3.2**) was solved for truncated DDX3X, which does not oligomerize or unwind RNA duplexes as efficiently as full-length DDX3X^{21,28,29,230}. Therefore, the dimers observed upon truncated DDX3X binding (**Fig. 3.2, 3.3**) may have a differing mode of action than trimers formed by the fully-functional full-length DDX3X. Finally, while kinetic studies indicated that one protomer of the Ded1p trimer is the active unwinding unit of the trimer²⁸, this mode of action does not necessarily preclude the mechanism indicated by the structural analysis (**Fig. 3.3**). While one protomer of Ded1p may be the active unwinding unit, the other protomers of Ded1p could still interact with the RNA duplex and anchor one strand, while the active unwinding protomer pries the second strand away from the anchored strand. Additionally, while

Ded1p and DDX3X exhibit highly similar enzymatic activities *in vitro*, their activities are not identical, raising the possibility for differences in the mechanism of Ded1p and DDX3X RNA unwinding²¹. Ultimately, further kinetic analysis of Ded1p/DDX3X unwinding on blunt RNA duplexes, as well as additional structural studies with full-length DDX3X and RNA duplexes containing a ssRNA overhang, are required to fully characterize the mechanism of DDX3X RNA helicase activity.

3.2 Biological roles of DDX3X

DDX3X is an X-linked gene that has been shown to be essential in tissue culture and mouse studies²³⁵⁻²³⁸. DDX3X escapes X-inactivation and is expressed in all human tissues^{39,143,224}. In males the highly similar (> 90% sequence similarity) DDX3Y is expressed from the Y chromosome in the testes, the heart, hematopoietic immune cells, and the enteric nervous system^{218,239}. DDX3Y and DDX3X function redundantly in translation, even though DDX3Y exhibits reduced enzymatic activity *in vitro*^{218,239}. Thus, DDX3Y is able to compensate for DDX3X loss in tissues where DDX3Y is expressed^{218,236,239-241}.

DDX3X plays a role in both nuclear and cytoplasmic RNA metabolism via its interactions with RNA and other proteins. In the nucleus, DDX3X regulates transcription by interacting with several transcription factors. DDX3X interacts with the IRF-3/p300/CBP complex that activates transcription from the IFN- β promoter to induce production of interferons and proinflammatory cytokines²⁴². DDX3X's association with this complex enhances its binding to the IFN- β promoter²⁴². DDX3X also interacts with the Sp1 transcription factor to enhance

transcription of the cyclin-dependent kinase inhibitor p21^{waf1/cip1}, which is involved in cell cycle control^{243,244}. Finally, DDX3X has circRNA-mediated interactions with the YY1 transcription factor that increase β -catenin expression and Wnt/ β -catenin signaling (involved in maintenance of stem cells, cell proliferation/migration, and development)²⁴⁵⁻²⁴⁷.

DDX3X has also been implicated in miRNA biogenesis. DDX3X can associate with the Drosha/DGCR8 complex that cleaves primary miRNAs in the nucleus prior to their cytoplasmic export for further processing into mature miRNAs^{248,249}. DDX3X also associates with several miRNA loci, where DDX3X may impact their transcription²⁵⁰. Loss of DDX3X negatively impacts the expression of several miRNAs, suggesting a functional role for DDX3X in miRNA processing^{248,250,251}. DDX3X also interacts with two nuclear export receptors, TAP and CRM1, as well as eIF4E-dependent export mRNPs; however, DDX3X is not required for nuclear export to occur, so the functional significance of these interactions remains unclear^{55,252-254}.

DDX3X's most well-characterized functions occur in the cytoplasm. Both Ded1p and DDX3X directly bind components of the eIF4F complex as well as helix 16 near the entry channel of the ribosome^{59-61,116,219,255}. RNA cross-linking and immunoprecipitation (CLIP) studies combined with ribosome profiling revealed that Ded1p and DDX3X bind extensively along mRNAs near ribosome-bound regions^{61,62}. Ded1p and DDX3X promote translation of structured mRNAs; however, Ded1p appears to be required for efficient translation of a higher percentage of the yeast transcriptome compared to DDX3X's role in

humans^{59,60,63,64,217,256,257}. Mechanistically, DDX3X/Ded1p are thought to promote translation by resolving mRNA secondary structures in the 5'-UTR to facilitate scanning by the pre-initiation complex and translation initiation at canonical start codons^{59,60,63,64,217,255-257}.

DDX3X also plays a role in regulating repeat-associated non-AUG (RAN) translation^{258,259}. RAN translation occurs in trinucleotide repeat expansion diseases such as Fragile X-associated tremor/ataxia syndrome (FXTAS), *C9orf72*-associated amyotrophic lateral sclerosis and frontotemporal dementia (*C9orf72*-ALS/FTD), and Huntington's disease^{258,259}. These repeat expansion diseases express long repeat-containing RNAs that cause cellular toxicity by sequestering RNA-binding proteins and/or via accumulation of their encoded dipeptide repeat proteins^{258,259}. Expression of these toxic dipeptide repeat proteins occurs via RAN translation that initiates on the hairpin-forming repeats independent of the start codon in the repeat-expanded RNA²⁶⁰. In the setting of FXTAS, DDX3X is required for RAN translation to occur²⁵⁸; however, in the setting of *C9ORF72*-ALS/FTD, DDX3X expression represses RAN translation²⁵⁹. The differences between these two settings and the exact role of DDX3X in modulating RAN translation remains unclear.

DDX3X and Ded1p are both components of cytoplasmic stress granules. As detailed in Chapter 2, stress granules form following inhibition of translation initiation via pharmacological inhibition or eIF2 α phosphorylation during the integrated stress response^{196,197,199}. Stress granules consist of translationally-repressed mRNAs, stalled translation initiation complexes, and a wide variety of

RBPs^{196,197,199,261}. DDX3X is an essential stress granule component whose knockdown reduces stress granule formation and whose overexpression nucleates stress granule formation in the absence of applied stress^{220,261}. DDX3X associates with stress granules via its N-terminal intrinsically disordered region, and overexpression of the N-terminus alone is sufficient to induce stress granule formation (though to a lesser extent than overexpression of full-length DDX3X)^{62,220}.

DDX3X also plays a role in Wnt/ β -catenin, pyroptosis, and innate immune signaling cascades. DDX3X binds CK1 ϵ and stimulates its kinase activity, stabilizing β -catenin and potentiating Wnt/ β -catenin signaling^{262,263}. Following exposure to stress, DDX3X can associate with stress granules or the inflammasome, with DDX3X incorporation into the inflammasome promoting cell death via pyroptosis²²¹.

In the innate immune response, several classes of pattern recognition receptors recognize pathogens and activate intracellular signaling cascades that drive transcription of interferons and proinflammatory cytokines²⁶⁴. Most of these signaling cascades converge to include the two homologous kinases TBK1 or IKK ϵ that act upstream of interferon transcription²⁶⁴. Studies from multiple groups demonstrate that DDX3X is required for interferon production^{242,264,265}. DDX3X directly binds both TBK1 and IKK ϵ ^{264,266}. DDX3X binds and activates IKK ϵ , which then phosphorylates DDX3X, leading to enhanced transcriptional activation of the IFN- β promoter²⁶⁶. The homologous kinase TBK1 also phosphorylates DDX3X, which promotes DDX3X association with the IFN- β promoter, leading to

enhanced interferon production²⁶⁴. DDX3X's association with the IFN- β promoter is mediated by DDX3X binding to the IRF-3/p300/CBP complex that activates IFN- β transcription²⁴².

DDX3X also interacts with two proteins in the signaling cascade upstream of TBK1/IKK ϵ : TRAF3 and MAVS, which form a complex following activation of RIG-I by viral RNA^{267,268}. Given DDX3X's activating presence at several stages of the innate immune signaling cascade, it is possible that DDX3X may serve as a scaffolding protein to promote innate immune signaling (**Fig. 3.4**)²⁶⁸. Finally, DDX3X also binds the kinase IKK α , which functions in a parallel signaling pathway to promote the TBK1/IKK ϵ -independent induction of interferons²⁶⁹.

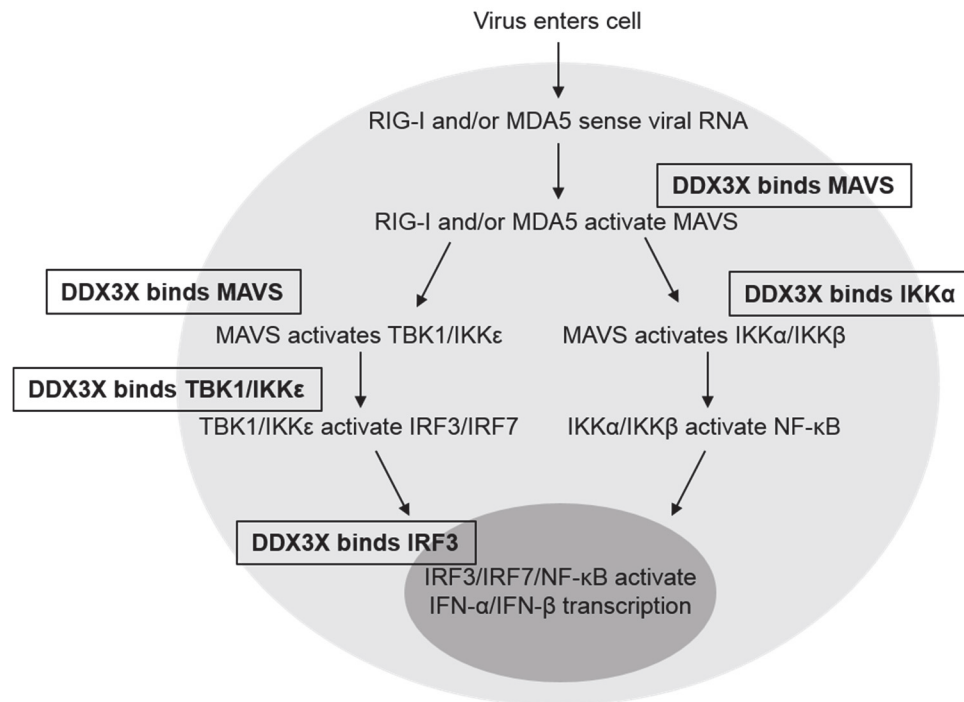


Figure 3.4. DDX3X interactions during innate immune signaling. Simplified schematic of RIG-I/MDA5 innate immune signaling is depicted^{270,271}. Signaling complexes bound by DDX3X are indicated.

3.3 DDX3X in human disease

Dysregulation of DDX3X occurs in several disease states, including DDX3X syndrome, numerous cancers, and viral infection.

3.3.1 DDX3X syndrome

DDX3X syndrome is a genetic neurodevelopmental disorder that is a leading cause of intellectual disability and global developmental delay in female patients, accounting for 1-3% of intellectual disability in females^{143,272}. DDX3X syndrome results from *de novo* germline mutations in DDX3X that disrupt proper neurodevelopment^{224,272,273}. These mutations are most frequently missense mutations or in-frame deletions, but nonsense, frameshift, and splice site mutations also occur²²⁴. The clinical presentation of DDX3X syndrome is variable, with the majority of patients exhibiting intellectual disability or developmental delay¹⁴³. Other symptoms include hypotonia, movement disorders, microcephaly, autism spectrum disorder, hyperactivity, aggression, and epilepsy¹⁴³. The higher proportion of female patients with DDX3X syndrome is thought to arise from both embryonic lethality in male patients with deleterious DDX3X mutation, as well as some compensation for DDX3X loss by the highly similar Y chromosome-encoded DDX3Y^{224,241}.

Several recurrent missense mutations in DDX3X syndrome induce the aberrant formation of DDX3X-containing stress granules when exogenously overexpressed in human cells²²⁴. The majority of these mutations occur within the helicase core and disrupt DDX3X enzymatic activity *in vitro*²²⁴. Interestingly, patients with granule-inducing missense mutations exhibit more severe clinical

phenotypes than patients with non-granule-inducing or nonsense mutations²²⁴. This finding suggests that the aberrant formation of DDX3X-containing granules acts in a dominant negative manner to produce more severe neurodevelopmental defects than DDX3X haploinsufficiency²²⁴. Interestingly, *de novo* germline mutations in DDX3X have also been associated with autism spectrum disorder and Toriello-Carey neurodevelopmental disorder^{224,272}.

3.3.2 DDX3X dysregulation in cancer

DDX3X mutations and changes in DDX3X expression level have been identified in numerous cancers with varying correlations to patient prognosis²⁷⁴⁻²⁷⁶. Depending on the primary tissue type and experimental detection methods used, both DDX3X overexpression and DDX3X loss correlate with patient outcomes in cancer, leading to classification of DDX3X as both a tumor suppressor and an oncogene²⁷⁴⁻²⁷⁶. To further complicate matters, several studies that identified DDX3X dysregulation in patient tumors found that this dysregulation did not correlate to patient prognosis²⁷⁷⁻²⁸⁰. Thus, the causative nature of DDX3X dysregulation in driving tumorigenesis remains unclear.

As noted above, DDX3X overexpression can nucleate the formation of stress granules²²⁰, and stress granules have been histologically observed in a variety of tumors^{62,196,197,201}. Thus, we propose that DDX3X overexpression may lead to sequestration of DDX3X within stress granules, potentially mirroring the effects of DDX3X loss, and leading to DDX3X's seemingly conflicting roles as both a tumor suppressor and an oncogene. Furthermore, DDX3X-mediated regulation of gene expression (both transcriptionally and post-transcriptionally as

described above) and cellular signaling may lead to tissue-specific effects and outcomes, further explaining the wide variety of phenotypes seen following DDX3X disruption. Regardless, it is clear that cellular DDX3X levels must be properly maintained to prevent disease.

DDX3X overexpression is linked to several cancers with varying effects on patient prognosis. In gallbladder cancer, DDX3X overexpression is an independent indicator of poor patient survival that correlates with increased tumor size, stage, and metastasis²⁸¹. Similarly, DDX3X overexpression in pancreatic ductal adenocarcinoma correlates with decreased patient survival^{282,283}. In breast cancer samples, DDX3X was found to be overexpressed compared to adjacent normal tissue; however, less than half of studies showed significant correlation between DDX3X overexpression and patient outcomes in breast cancer^{277,284-287}. DDX3X is also overexpressed in prostate cancer samples; however, no clear association between DDX3X overexpression and patient outcomes in prostate cancer has been identified^{280,288,289}.

In other organ systems, cancer-associated DDX3X underexpression has been shown to correlate with poor prognosis. In HPV-associated and non-small cell lung cancer, DDX3X is underexpressed in p53-inactivated tumors and correlates with decreased patient survival^{290,291}. In renal cell carcinoma, decreased DDX3X expression is an independent predictor of poor patient outcomes²⁹². Similarly, in melanoma DDX3X is frequently lost via nonsense mutations, leading to altered translation of DDX3X-dependent transcripts and decreased relapse-free survival²²³.

For several cancer types, both DDX3X over- and underexpression have been identified in patient samples, and the prognostic value of these findings varies with the clinical context. Several studies have linked DDX3X overexpression to poor prognosis and survival in colorectal cancer²⁹³⁻²⁹⁷; however, the exact role of DDX3X in colorectal cancer remains unclear as a conflicting study demonstrated that DDX3X underexpression correlated with worse patient outcomes²⁸⁵. Similarly, in head and neck squamous cell carcinomas (HNSCC) and oral squamous cell carcinomas (OSCC), DDX3X tumor levels vary with the clinical setting. DDX3X overexpression is associated with chemoresistance in OSCC tumors²⁹⁸; however, DDX3X underexpression has also been associated with decreased patient survival^{299,300}. In smoking patients, DDX3X overexpression correlates with decreased patient survival in HNSCC, while in non-smoking patients, DDX3X underexpression correlates with decreased patient survival^{256,301}. Finally, both DDX3X over- and underexpression have been identified in hepatocellular carcinoma, with underexpression being more common in HBV-positive patients^{251,302,303}.

Frequent DDX3X mutations occur in a variety of hematological malignancies. A variety of both missense and nonsense/truncating mutations occur in chronic lymphocytic leukemia³⁰⁴⁻³⁰⁹. The prognostic value of these recurrent mutations is yet to be defined³⁰⁴⁻³⁰⁹. Missense and truncating mutations also frequently occur in a variety of B cell lymphomas^{222,310-313}. While the prognostic value of these recurrent mutations has not been clearly defined for all B-cell lymphoma subtypes, DDX3X mutation is associated with significantly

reduced patient survival in the setting of diffuse large B-cell lymphoma (3.4 year median survival for DDX3X-mutated patients vs. 17.6 year median survival for DDX3X-wildtype patients)²²². Finally, DDX3X nonsense and missense mutations also recurrently occur in natural killer/T-cell lymphomas, with mixed results regarding the prognostic value of DDX3X mutational status^{278,314-316}.

Finally, DDX3X is recurrently mutated in the pediatric brain tumor medulloblastoma. The majority of these mutations are missense mutations within the helicase core that primarily occur in adult SHH-subtype tumors and pediatric WNT-subtype tumors^{279,317-322}. Several of these missense mutations overlap with mutations occurring in DDX3X syndrome and have also been shown to reduce DDX3X helicase activity *in vitro* and induce aberrant stress granules in human cells, similar to observations for mutations in DDX3X syndrome^{61,62,224,230,233}. However, the mechanistic/pathogenic function of these aberrant granules in tumorigenesis is currently less clearly defined than in DDX3X syndrome, though studies in mice have shown that DDX3X likely plays a tumor-suppressive role in the setting of medulloblastoma^{240,318}.

Further studies with larger patient cohorts and measurement of several confounding variables are required to fully elucidate the molecular effects of DDX3X deregulation in promoting tumorigenesis and cancer progression.

3.3.3 DDX3X in viral infections

Unsurprisingly, given its extensive involvement in innate immune signaling (**Fig. 3.4**), DDX3X has been identified as a frequent target or co-opted host factor of diverse viruses³²³. DDX3X knockdown has been shown to reduce viral

replication of diverse viruses, including positive-sense RNA viruses (murine norovirus, west nile virus, Japanese encephalitis virus, enterovirus 71, and SARS-CoV-2), ambisense RNA viruses (Lassa and Junin arenaviruses), double-stranded DNA viruses (herpes simplex 1 and human cytomegalovirus), and retroviruses (HIV-1)³²⁴⁻³³⁴. DDX3X's pro-viral role for the majority of these viruses is thought to involve DDX3X-mediated promotion of viral translation^{255,326-328,330,335-337}.

Hepatitis C virus (HCV, positive-sense RNA virus) also co-opts DDX3X for its replication. DDX3X interacts with both the 3'-UTR of HCV RNA and the nucleocapsid core protein³³⁸⁻³⁴². Interactions with the 3'-UTR and core protein redistribute DDX3X from stress granules to the lipid droplets where HCV replication takes place³³⁸⁻³⁴². This co-opting of DDX3X is required for HCV replication³⁴¹. Interactions between DDX3X and the core protein further promote viral survival by disrupting interactions between DDX3X and the antiviral signaling protein MAVS, leading to reduced interferon production³⁴².

DDX3X has also been shown to have antiviral effects during infection. DDX3X knockdown promotes replication of Hepatitis B virus (HBV, DNA virus), though the exact antiviral role of DDX3X during HBV infection remains unclear³⁴³⁻³⁴⁵. DDX3X knockdown also promotes replication of dengue virus (positive-sense RNA flavivirus), which produces a capsid protein that directly binds DDX3X's helicase core to interfere with innate immune signaling^{346,347}. DDX3X also plays an antiviral role during influenza A virus (negative-sense RNA virus) infection^{348,349}. While two proteins produced by influenza A virus, NS1 and NP,

interact directly with DDX3X, the exact effects of these interactions on the immune response remain unclear^{348,349}. Finally, vaccinia virus (DNA poxvirus) produces a virulence factor (K7) that directly binds DDX3X to disrupt interferon production²⁶⁵.

Although the effect of DDX3X deregulation on viral regulation and immune signaling have been investigated, the effects of these DDX3X-virus interactions on DDX3X helicase activity and associated host RNA metabolism have to our knowledge never been studied. Since DDX3X promotes translation of several pro-inflammatory transcripts^{257,350} and associates with antiviral stress granules^{206,207,220}, DDX3X's biological functions outside of the interferon signaling cascade may also be important aspects of the host immune response to viral infection. Thus, these uninvestigated "other functions" are also likely manipulated by viral interactions with DDX3X.

While DDX3X's involvement in a wide variety of viral infections makes it an attractive host target for the development of new broad-spectrum antiviral therapies^{323,351}, our lack of understanding about how viruses alter DDX3X's host functions makes it difficult to predict which aspects of DDX3X activity are ideal for pharmacological inhibition. In my thesis work, I have begun to address this lack of knowledge by characterizing the effects of the viral protein K7 (produced by vaccinia virus) on DDX3X's helicase activity and biological functions. In chapter 4, I measure the impact of K7 binding on DDX3X RNA unwinding and ATP hydrolysis activities *in vitro*, as well as characterize the molecular mechanism underlying these effects. In chapter 5, I investigate K7's effects on DDX3X's

ability to form phase-separated protein condensates *in vitro*, as well as DDX3X's association with stress granules in human cells. Chapter 6 then shows the effects of K7 expression on DDX3X's role in translation, as well as K7's effects on cell viability and growth. Finally, in chapter 7 I summarize other studies where I tested the ability of small molecules and metabolites to modulate LLPS.

Chapter 4

The viral protein K7 impacts DDX3X enzymatic activity by binding to DDX3X's disordered N-terminus

4.1 Introduction

Vaccinia virus (VACV) is the DNA poxvirus used in the live vaccine against smallpox and frequently studied for its potential use as a delivery vector for oncolytic/anti-cancer vaccines and vaccination against other infectious diseases (HIV, tuberculosis, etc.)³⁵²⁻³⁵⁴. VACV consists of a large (~200 kb) dsDNA genome³⁵². About half of this genome encodes conserved orthopoxvirus proteins involved in the process of viral replication, which occurs in the cytoplasm of the host cell³⁵². The other half of the genome encodes non-essential virulence factors, proteins that facilitate the virus's ability to infect a particular host, evade the immune response, and damage the host (e.g. cause symptoms, organ damage, mortality, etc.)^{352,355-357}. Virulence factors produced by VACV target and counteract many aspects of the host immune response, including the complement system, interferon production and signaling, cytokine production and signaling, apoptosis, and natural killer cell activity³⁵². Although many VACV virulence factors target similar host pathways, the majority are non-redundant and significantly reduce virulence *in vivo* when deleted from the virus³⁵².

K7 is a virulence factor that is produced early during infections and conserved among orthopoxviruses^{265,358}, including several strains of monkeypox virus^{359,360}. Both K7 mRNA and protein are detectable as early as 2 hr post-infection with VACV, and K7 protein levels increase up to 24 hr post-

infection^{265,358}. Deletion of K7 does not affect viral replication in tissue culture models, but does reduce VACV virulence *in vivo*³⁵⁸. Following intradermal infection, mice infected with VACV lacking K7 developed smaller lesions³⁵⁸. When mice were infected intranasally, VACV lacking K7 produced less symptoms/weight loss and was cleared more rapidly than wildtype virus³⁵⁸. Inspection of the infected intrapulmonary tissues revealed increased immune cell infiltration and cytolysis of infected cells in the absence of K7, indicating reduced immune evasion³⁵⁸.

Two independent affinity-purification mass spectrometry studies identified a combined total of 78 host proteins that interact with K7 in HeLa or HEK293T cells^{361,362}. 7 proteins have been validated to interact with K7 using low-throughput methods: coatamer (vesicle transport), retromer (membrane receptor recycling), CHEVI (endosomal trafficking), Spir-1 (actin nucleator with roles in immune signaling), TRAF6 (immune signaling), IRAK2 (immune signaling), and DDX3X^{265,361,363-365}. In both high-throughput K7-binding screens, DDX3X was identified as either the most or second most enriched protein^{361,362}.

K7 binds DDX3X *in vitro* with affinities in the range of $K_d = 0.1-1 \mu\text{M}$ ^{364,365}. Pull-down studies mapped K7 binding to residues 81 to 90 (81-KSSFFSDRGS-90) in DDX3X's disordered N-terminal extension, which were subsequently co-crystallized with full-length K7 (**Fig. 4.1**)^{364,365}. Interactions between K7 and DDX3X include hydrophobic contacts, hydrogen bonds, and electrostatic interactions³⁶⁴. Phenylalanines 84 and 85 of DDX3X insert into the hydrophobic cleft on the surface of K7, an interaction that is required for K7 binding to DDX3X

(Fig. 4.1)³⁶⁴. Additional interactions occur via salt bridges between K7 and arginine 88 of DDX3X, hydrogen bonds between K7 and serine 83 of DDX3X, and electrostatic interactions between the negatively-charged K7 (pI = 4.8) and the more positively-charged N-terminal extension of DDX3X (pI = 7.8 for DDX3X residues 1-143)³⁶⁴. Cell-based reporter assays demonstrated that interactions between K7 and DDX3X reduced interferon production²⁶⁵. Other effects of K7 binding on DDX3X function, such as DDX3X helicase activity and its associated roles in RNA metabolism, are unknown.

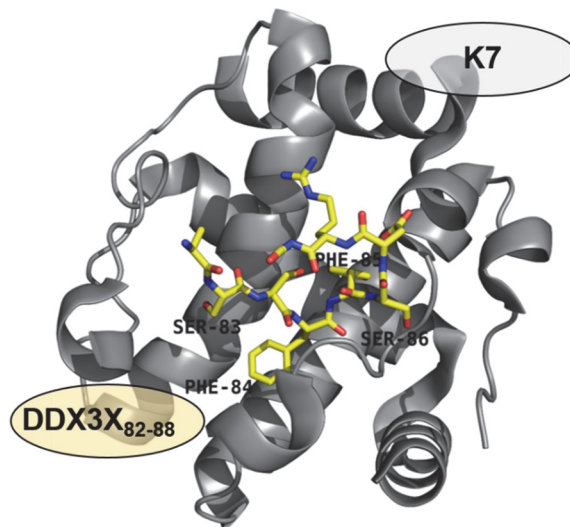


Figure 4.1. K7 binds DDX3X. Crystal structure of DDX3X residues 82-88 (DDX3X₈₂₋₈₈) bound to full-length K7. K7 is depicted in gray ribbon and DDX3X₈₂₋₈₈ is depicted by yellow sticks. PDB: 3JRV. Modified from³⁶⁴ with permission.

In this chapter, I measured K7's impact on DDX3X's RNA duplex unwinding and ATP hydrolysis activities *in vitro*. I determined the functional affinity for the K7-DDX3X interaction and identified K7-mediated changes in DDX3X's functional affinities for its two substrates: RNA and ATP. My data shows that K7 binding inhibits DDX3X by reducing functional RNA binding,

raising important questions about the biological impact of this inhibition on DDX3X's role in facilitating translation initiation.

4.2 K7 inhibits RNA unwinding by DDX3X

Recombinant His-K7 and DDX3X were purified to near homogeneity from *E. coli* (Fig. 4.2).

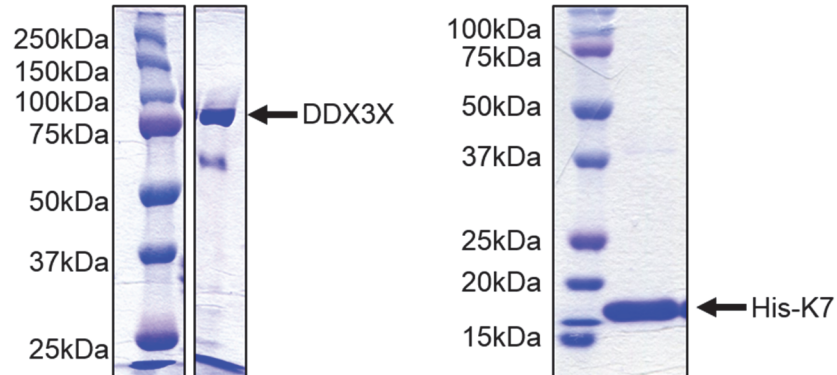


Figure 4.2. Purification of DDX3X and K7. Coomassie stained gels showing recombinant DDX3X following tag removal (left-hand gel) and recombinant His-K7 (right-hand gel). Both proteins were purified from *E. coli* using nickel affinity chromatography followed by ion exchange chromatography.

I then measured the impact of K7 on the RNA helicase activity of DDX3X by performing RNA unwinding assays with these purified proteins. I measured ATP-dependent RNA unwinding under pre-steady state conditions, using a well characterized substrate²¹ with a 16 bp duplex and a 25 nt single-stranded region 3' to the duplex (R16/41-3) (Fig. 4.3A). The pre-steady state reaction conditions allow the detection of inhibition or stimulation of protein-RNA binding, protein-ATP binding, and unwinding steps³⁶⁶.

K7 did not unwind RNA in the absence of DDX3X (Fig. 4.3B). K7 markedly reduced RNA unwinding by DDX3X (Fig. 4.3B,C). Apparent unwinding rate constants (k'_{unw}) decreased in a hyperbolic fashion with increasing

concentrations of K7 (**Fig. 4.3D**). Because K7 interacts with DDX3X outside the catalytic core of DDX3X^{265,364,365}, I fitted the resulting functional binding isotherm with a model for non-competitive inhibition and obtained an apparent inhibition constant for K7 of $K_i = 155 \pm 42$ nM (**Fig. 4.3D**). This value suggests that DDX3X and K7 interact during the unwinding reaction with a functional affinity similar to the affinities previously reported for the direct equilibrium binding of K7 to DDX3X^{364,365}.

I then probed whether the inhibition of the unwinding activity by DDX3X was due to binding of K7 to DDX3X, or due to non-specific effects of K7, such as competition for ATP or RNA. I measured the effect of K7 on the RNA unwinding activity of a DDX3X construct without the N- and C-terminal extensions (Δ DDX3X), which lacks the K7 binding site^{230,364}. This construct unwound RNA with a lower apparent unwinding rate constant (k'_{unw}) than full-length DDX3X, consistent with previous reports²³⁰. K7 had no detectable effect on the RNA unwinding activity of the Δ DDX3X construct (**Fig. 4.3E**). These data confirm that K7 inhibits the unwinding activity of DDX3X through direct interaction with DDX3X.

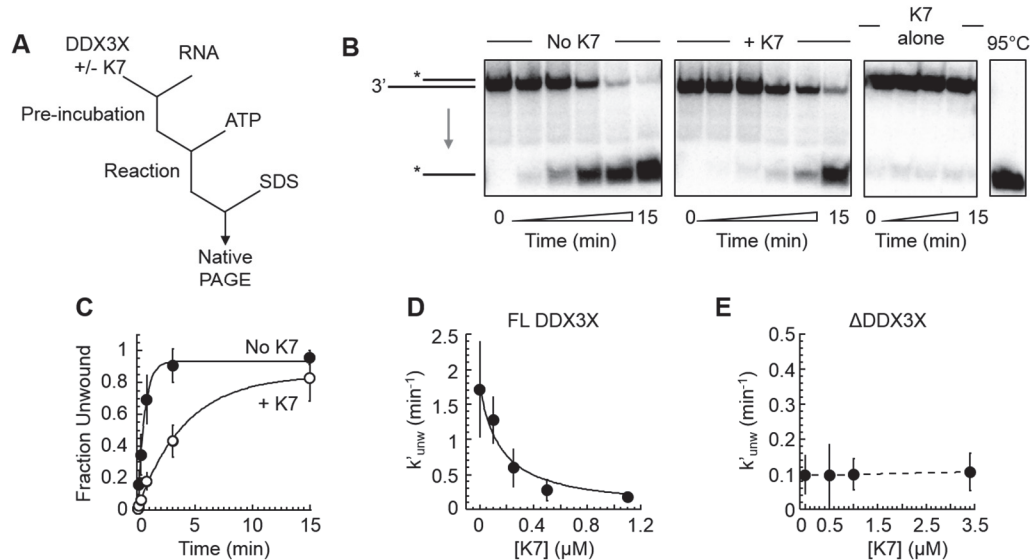


Figure 4.3. RNA unwinding by DDX3X in the presence of K7. (A) Experimental scheme for DDX3X pre-steady state unwinding reactions. **(B)** Representative PAGE for RNA unwinding reactions in the absence and presence of 1.1 μM K7 or in the presence of K7 alone without DDX3X. Cartoons indicate duplex RNA and unwound single strand, asterisk marks radioactivity. **(C)** RNA unwinding time course ($[\text{DDX3X}] = 400 \text{ nM}$) in absence and presence of 1.1 μM K7. Lines show the fits to the first order rate equation (No K7: $k'_{\text{unw}} = 1.64 \pm 0.12 \text{ min}^{-1}$, 1.1 μM K7: $k'_{\text{unw}} = 0.20 \pm 0.02 \text{ min}^{-1}$, $R^2 = 0.99$). **(D)** Inhibition of DDX3X ($[\text{DDX3X}] = 400 \text{ nM}$) unwinding by K7. Line shows the fit to a noncompetitive inhibition model ($K_i = 155 \pm 42 \text{ nM}$, $k_{\text{unw}}^{\text{max}} = 2.88 \pm 0.25 \text{ min}^{-1}$, $R^2 = 0.96$). **(E)** Truncated DDX3X ($[\Delta\text{DDX3X}] = 500 \text{ nM}$) unwinding rate constants in the presence of K7. Dashed line marks trend. For all reactions shown: $[\text{ATP}] = 2 \text{ mM}$ and $[\text{RNA}] = 0.5 \text{ nM}$. Error bars represent standard deviation from $n \geq 3$ replicates.

4.3 K7 inhibits RNA-dependent ATPase activity of DDX3X

I next tested whether K7 impacted the RNA-stimulated ATP hydrolysis activity of DDX3X by performing thin layer chromatography (**Fig. 4.4A,B**). I did not detect either ATP hydrolysis by DDX3X in the absence of RNA or ATP hydrolysis by K7 in the absence of DDX3X (**Fig. 4.4B**). Addition of K7 reduced observed hydrolysis rates for DDX3X-mediated ATP hydrolysis (**Fig. 4.4C**). Apparent initial hydrolysis rates (v_0) decreased in a hyperbolic fashion with increasing concentrations of K7 (**Fig. 4.4D**). Fitting of the resulting functional

binding isotherm to a modified Michaelis-Menten equation yielded an apparent inhibition constant $K_i = 135 \pm 57$ nM (**Fig. 4.4D**). This value is, within error, similar to the apparent inhibition constant obtained from the RNA unwinding measurements (**Fig. 4.3D**). This observation suggests that K7 impacts a reaction step that is common to both, RNA-stimulated ATPase and RNA unwinding reactions. K7 had no detectable effect on the RNA-stimulated ATP hydrolysis activity of Δ DDX3X (**Fig. 4.4E**), indicating that K7 inhibits this activity also through direct interaction with DDX3X.

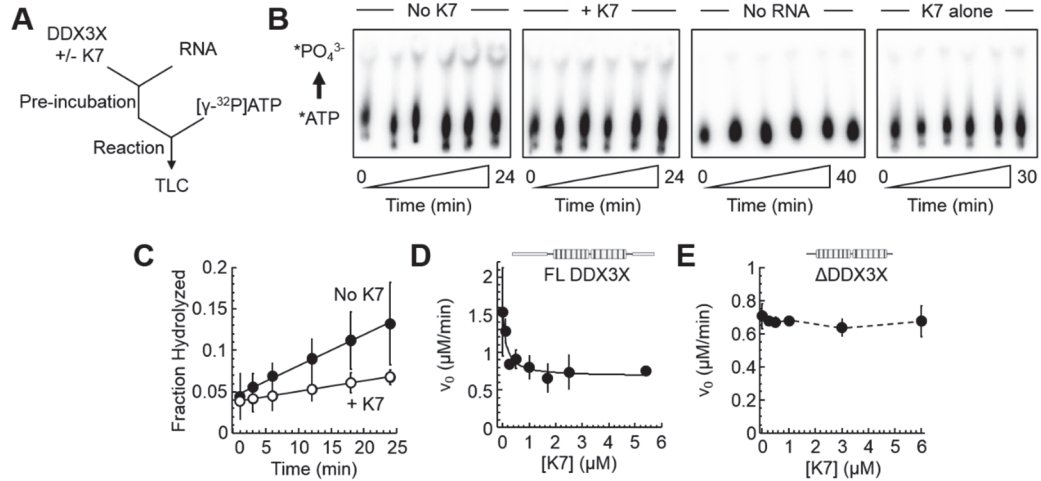


Figure 4.4. ATP hydrolysis by DDX3X in the presence of K7. (A) Experimental scheme for ATP hydrolysis. **(B)** Representative thin layer chromatography (TLC) plates for DDX3X in the absence and presence of K7, DDX3X in the absence of RNA, and K7 in the absence of DDX3X. **(C)** ATP hydrolysis time course ([DDX3X] = 400 nM) in absence and presence of 1.7 μM K7. Lines show the fit to a linear equation (No K7: $v_0 = 1.88$ $\mu\text{M}/\text{min}$, 1.7 μM K7: $v_0 = 0.63$ $\mu\text{M}/\text{min}$, $R^2 = 0.99$). **(D)** Inhibition of DDX3X ATP hydrolysis by K7. Line shows fit to a modified Michaelis-Menten equation ($K_i = 135 \pm 57$ nM, $v_0^{\text{max}} = 1.56 \pm 0.09$ $\mu\text{M}/\text{min}$, $R^2 = 0.99$). **(E)** Truncated DDX3X ([Δ DDX3X] = 500 nM) ATP hydrolysis rate constants in the presence of K7. Dashed line marks trend. For all reactions shown: [ATP] = 0.5 mM and [RNA] = 2 μM . Error bars represent standard deviation from $n \geq 3$ replicates.

4.4 K7 diminishes functional RNA binding by DDX3X

I then sought to identify which reaction step in the RNA-stimulated ATPase and ATP-stimulated RNA unwinding reactions was affected by K7. To accomplish this, I measured whether and how K7 impacted the functional affinities of DDX3X ($K_{1/2}$) for its two substrates, ATP and RNA. To determine the functional affinity of DDX3X for RNA ($K_{1/2}^{\text{RNA}}$), we measured RNA unwinding rate constants (k'_{unw}) as described in **Fig. 4.3**, with increasing DDX3X and constant ATP concentrations (**Fig. 4.5A**). As expected, the resulting functional binding isotherm was sigmoidal with a Hill coefficient $H = 4.3 \pm 0.8$ (**Fig. 4.5A**), indicating oligomerization of DDX3X²¹. Addition of K7 (500 nM) caused a marked reduction in the functional RNA affinity ($K_{1/2}^{\text{RNA}}$) of DDX3X, to an extent that saturating concentrations of DDX3X were not experimentally attainable (**Fig. 4.5A**). These data indicate that K7 inhibits functional RNA binding by DDX3X.

To determine the functional affinity of DDX3X for ATP ($K_{1/2}^{\text{ATP}}$), I measured RNA unwinding rate constants (k'_{unw}), as described above, with increasing ATP and constant DDX3X (200 nM) and RNA (0.5 nM) concentrations (**Fig. 4.5B**). Again, as expected, the resulting functional binding isotherm was sigmoidal with a Hill coefficient $H = 1.8 \pm 0.4$ (**Fig. 4.5B**). This observation indicates that DDX3X utilizes two molecules of ATP during RNA unwinding. Addition of K7 (500 nM) reduced the maximum unwinding rate constant ($k_{\text{unw}}^{\text{max}}$) (**Fig. 4.5B**). However, the functional ATP affinity ($K_{1/2}^{\text{ATP}}$) was not significantly altered (**Fig. 4.5B**). These observations indicate that K7 does not affect ATP binding by DDX3X.

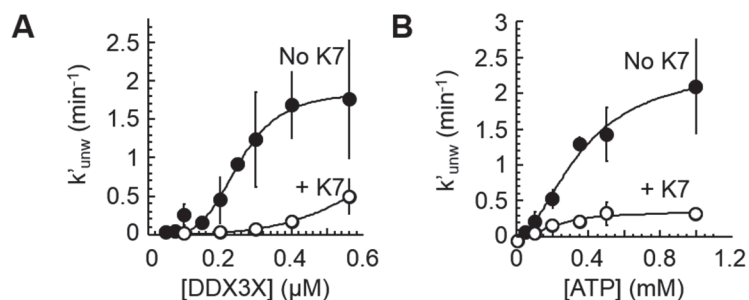


Figure 4.5. Dependence of RNA unwinding rate constants on DDX3X and ATP concentrations in the presence of K7. (A) Dependence of RNA unwinding rate constants on DDX3X concentration in the absence and presence of K7 ($[\text{K7}] = 500 \text{ nM}$, $[\text{ATP}] = 2 \text{ mM}$, $[\text{RNA}] = 0.5 \text{ nM}$). Lines show the fit to the Hill equation (No K7: $k_{unw}^{\text{max}} = 1.86 \pm 0.12 \text{ min}^{-1}$, $K_{1/2}^{\text{RNA}} = 253.88 \pm 12.94 \text{ nM}$, $H = 4.3 \pm 0.8$, $R^2 = 0.98$). No meaningful fit was obtained in the presence of K7 due to an inability to saturate the experiment with experimentally-obtainable DDX3X concentrations. (B) Dependence of RNA unwinding rate constants on ATP concentration in the absence and presence of K7 ($[\text{K7}] = 500 \text{ nM}$, $[\text{DDX3X}] = 200 \text{ nM}$, $[\text{RNA}] = 0.5 \text{ nM}$). Lines show the fit to the Hill equation (No K7: $k_{unw}^{\text{max}} = 2.39 \pm 0.30 \text{ min}^{-1}$, $K_{1/2}^{\text{ATP}} = 0.36 \pm 0.07 \text{ mM}$, $H = 1.8 \pm 0.4$, $R^2 = 0.98$; 500 nM K7: $k_{unw}^{\text{max}} = 0.34 \pm 0.04 \text{ min}^{-1}$, $K_{1/2}^{\text{ATP}} = 0.23 \pm 0.04 \text{ mM}$, $H = 2.2 \pm 0.6$, $R^2 = 0.97$). Error bars represent standard deviation from $n \geq 3$ replicates.

Collectively, our results show that K7 inhibits functional RNA binding but not ATP binding by DDX3X. Since RNA binding is required for both, RNA unwinding and RNA-stimulated ATPase activity, this mode of K7 function explains the observed inhibition of both activities (Figs. 4.3, 4.4). Most likely, K7 binding to the intrinsically disordered N-terminus of DDX3X^{364,365} interferes with the formation of the DDX3X oligomer that is required for effective RNA unwinding^{21,28}.

4.5 Discussion

As shown here, K7 binding to DDX3X inhibits RNA duplex unwinding and RNA-stimulated ATP hydrolysis. The reduction of DDX3X's functional RNA affinity ($K_{1/2}^{\text{RNA}}$) in the presence of K7 indicates that reduced RNA binding

accounts for K7's inhibition of both DDX3X RNA unwinding and ATPase activities. Given that the disordered termini are involved in the formation of the functional DDX3X trimer²⁸, K7 likely reduces DDX3X's functional RNA affinity ($K_{1/2}^{\text{RNA}}$) by reducing formation of the functional oligomer.

Although the relationship between DDX3X concentration and RNA unwinding rate constants (k'_{unw}) appears to remain sigmoidal in the presence of K7 (**Fig. 4.5A**), indicating formation of an oligomer to unwind RNA even in the presence of K7, the DDX3X concentrations required to form the oligomer are significantly increased. This observation suggests that the DDX3X-K7 complex is not able to unwind RNA duplexes, so K7 reduces the effective DDX3X concentration in the reaction. However, reduced oligomerization of DDX3X, reduced RNA binding, or a combination of the two could all lead to the observed reduction in functional RNA affinity ($K_{1/2}^{\text{RNA}}$) upon K7 binding.

The minimal unwinding unit of DDX3X that lacks the full N- and C-terminal extensions (ΔDDX3X) also exhibits a sigmoidal relationship between enzyme concentration and RNA unwinding rate constants; however, the functional RNA affinity is significantly higher ($K_{1/2}^{\text{RNA}} = 950 \pm 150 \text{ nM}$)²⁹ than for full-length DDX3X ($K_{1/2}^{\text{RNA}} = 254 \pm 13 \text{ nM}$). This data is consistent with a scenario in which formation of the functional oligomer is reduced by truncation of the N- and C-terminal extensions. Formaldehyde crosslinking followed by western blotting of both recombinant full-length DDX3X and ΔDDX3X demonstrated formation of oligomers by both proteins (**Fig. 4.6**); however, consistent with the

reduced functional RNA affinity ($K_{1/2}^{RNA}$) of Δ DDX3X, Δ DDX3X formed fewer oligomers at higher protein concentrations when compared to full-length DDX3X.

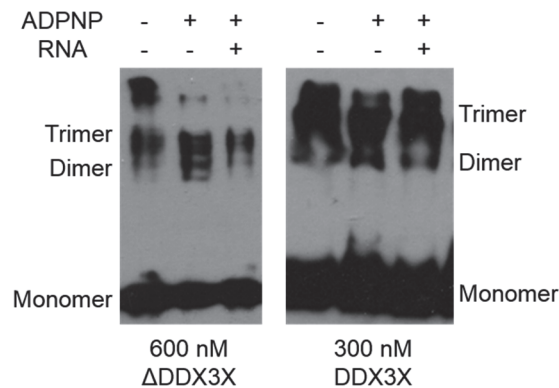


Figure 4.6. Oligomerization of full-length and truncated DDX3X. 600 nM Δ DDX3X and 300 nM DDX3X were crosslinked with formaldehyde for 30 min in the presence and absence of 2 μ M RNA duplex (R16/41-3) and/or 0.5 mM ADPNP. Proteins were resolved by SDS-PAGE and western blotting against DDX3X was performed.

Since functional RNA binding does not always correlate directly with physical RNA binding (e.g. the helicase could still bind RNA without unwinding it), I started dissecting K7's potential effects on RNA binding and/or DDX3X oligomerization by first measuring K7's impact on DDX3X oligomerization as visualized by formaldehyde crosslinking (**Fig. 4.7**). Similar to previous observations with Ded1p²⁸, DDX3X primarily formed dimers and trimers in the presence of RNA and ADPNP but formed even higher molecular weight oligomers in the absence of RNA (**Fig. 4.7**). Addition of K7 led to the appearance of a new band, indicating formation of the K7-DDX3X complex; however, no clear decrease in DDX3X oligomers could be visualized (**Fig. 4.7**). Given the semi-quantitative nature of formaldehyde crosslinking and the large excess of free

monomeric DDX3X remaining after crosslinking (**Fig. 4.7**), this result does not rule out K7-mediated prevention of DDX3X oligomerization.

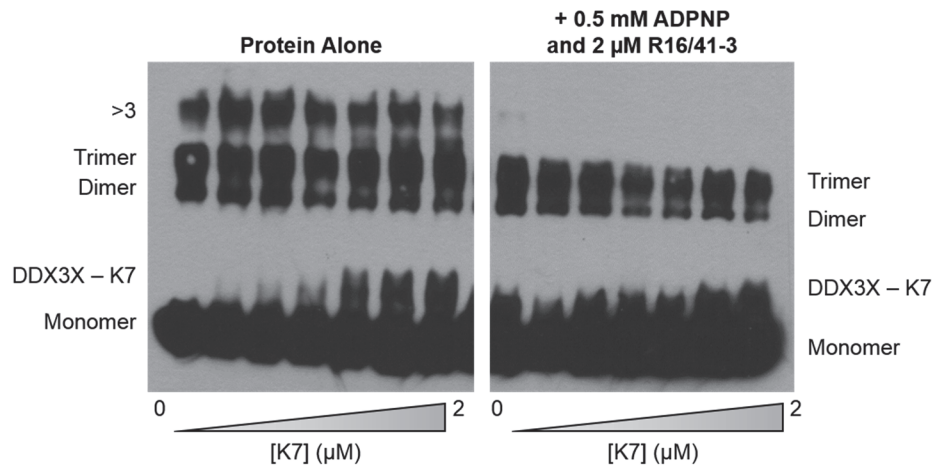


Figure 4.7. K7 effects on DDX3X oligomerization. 200 nM DDX3X was crosslinked with formaldehyde for 30 min in the presence of 0-2 μM K7 +/- 2 μM RNA duplex (R16/41-3) and 0.5 mM ADPNP. Proteins were resolved by SDS-PAGE and western blotting against DDX3X was performed.

As I have not measured physical interactions between DDX3X and RNA in the presence of K7, reduced RNA binding when K7 is present also remains a possibility. Since K7 is a negatively-charged protein³⁶⁴, its binding to DDX3X could potentially reduce interactions between DDX3X and negatively-charged RNA. Additionally, if neither physical RNA binding or oligomerization are disrupted by K7, K7 binding may primarily interfere with the strand separation step, though the parallel reduction in RNA-stimulated ATPase activity (**Fig. 4.4**), which does not require strand separation, makes this scenario less likely.

In the next chapter I provide additional *in vitro* evidence supporting the idea that K7 binding reduces DDX3X oligomerization and then correlate these *in vitro* studies with cellular studies of DDX3X's ability to form stress granules.

Chapter 5

The viral protein K7 impacts DDX3X condensate formation *in vitro* and in human cells

5.1 Introduction

Vaccinia virus (VACV) infection is initiated by binding and fusion of virion with the host cell membrane³⁶⁷. This fusion event releases a viral core into the host cell cytoplasm³⁶⁷. This viral core contains the viral dsDNA genome and transcriptional enzymes required to start transcription of the viral genome³⁶⁷. VACV transcription occurs in 3 stages: (i) transcription of early mRNAs encoding proteins required for viral DNA replication, recruitment of the host cell translation machinery, and immune evasion, (ii) transcription of intermediate mRNAs encoding proteins that regulate expression of late viral transcripts, and (iii) transcription of late mRNAs encoding proteins required to form new virions³⁶⁷⁻³⁶⁹. Early-stage mRNAs are ribosome-bound within the first 2-3 hr of infection, and intermediate/late mRNAs are ribosome-bound within 4-8 hr of infection³⁶⁸.

VACV transcription, translation of viral mRNAs, and subsequent virion assembly occurs within viral factories, discrete perinuclear sites in the host cell cytoplasm that are surrounded by a host-derived endoplasmic reticulum membrane³⁷⁰. While VACV encodes its own transcriptional machinery, VACV is dependent on the host cell translation machinery and encodes several proteins that recruit the host translation machinery to viral factories³⁶⁹. Like other viruses that rely on the host translational machinery to produce viral proteins, VACV has developed several strategies to block the phosphorylation of eIF2 α that leads to

inhibition of translation initiation and stress granule formation within the host cell³⁶⁹. The K3L protein produced by VACV acts as a PKR pseudosubstrate and competes for eIF2 α binding to PKR, thereby reducing eIF2 α phosphorylation by PKR^{369,371}. In parallel, the E3L protein produced by VACV binds dsRNA produced during viral replication to delay and reduce PKR activation via host cell sensing of dsRNA^{369,371}. When VACV lacking the E3L protein is expressed, antiviral granules (AVGs), RNPs resembling stress granules, form adjacent to viral factories and suppress viral replication^{369,372}.

AVGs contain many of the same proteins found in stress granules (G3BP1, TIA1, eIF3b, etc.) and also form downstream of eIF2 α phosphorylation, but lack the 40S ribosomal subunits and translationally-repressed host mRNAs found within stress granules^{369,372,373}. Additionally, while stress granules are dissolved/blocked by stabilization of polysomes following cycloheximide treatment, cycloheximide is less effective at dissolving AVGs, further differentiating them from canonical stress granules^{369,372,373}. While the expression of the viral protein E3L largely prevents AVG formation, some AVGs do form in cells infected with VACV^{369,372}.

Given the numerous parallel strategies employed by VACV to block eIF2 α phosphorylation and the downstream formation of AVGs/stress granules³⁶⁹, as well as K7's binding to the disordered N-terminal extension required for DDX3X association with stress granules³⁶⁴, I wondered if K7 binding to DDX3X would represent another strategy for VACV to block AVG/stress granule formation. To test this question, I measured the impact of recombinant K7 on recombinant

DDX3X's ability to form protein condensates *in vitro*. I then characterized the effect of K7 expression on the formation of stress granules in human cells. Finally, I tested whether mutation of the well-defined K7 binding motif in DDX3X's N-terminus³⁶⁴ would reduce K7's impact on DDX3X association with stress granules.

5.2 K7 inhibits condensate formation by DDX3X *in vitro*

The disordered N-terminus of DDX3X is required for the association of DDX3X with stress granules, which form via liquid-liquid phase separation (LLPS)²²⁰. I therefore tested whether K7 binding to DDX3X's N-terminus affected the formation of DDX3X condensates *in vitro*.

To visualize and quantify DDX3X condensates, I mixed purified DDX3X with a small fraction of fluorescently labelled DDX3X and, after incubation, deposited the samples on microscope slides³⁷⁴. Recombinant full-length DDX3X spontaneously formed circular condensates at room temperature (**Fig. 5.1**), consistent with previous reports of LLPS for Ded1p and DDX3X *in vitro*^{217,218}. Addition of K7 resulted in a reduced number and size of DDX3X condensates (**Fig. 5.1**). This reduction became more pronounced with increasing concentrations of K7. Large condensates were depleted at lower K7 concentrations, smaller ones at higher K7 concentrations (**Fig. 5.1**). These data indicate that K7 interferes with the formation of DDX3X condensates *in vitro*.

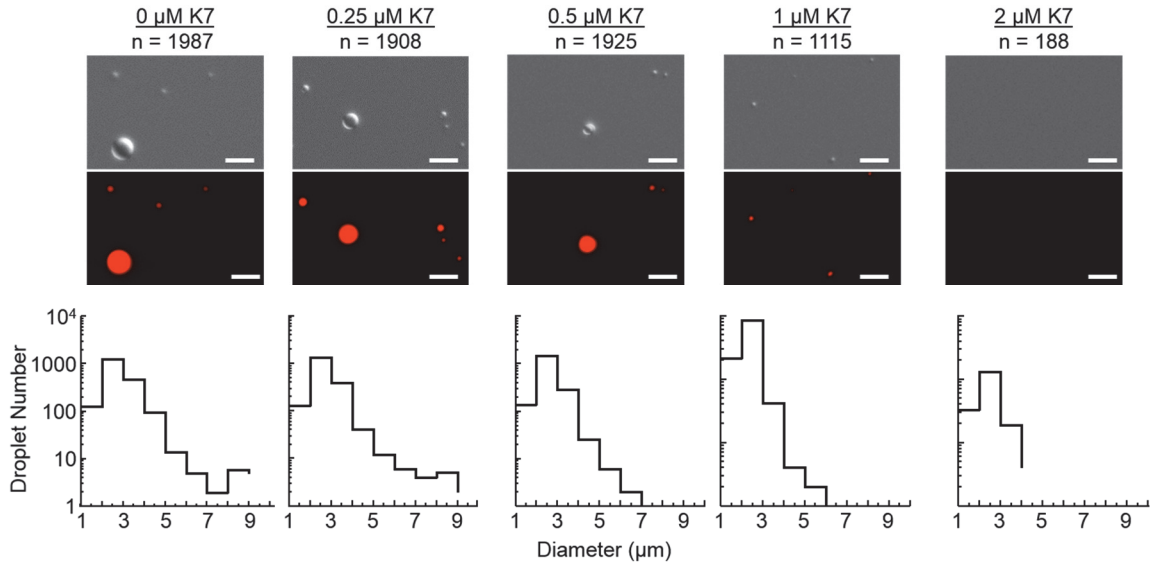


Figure 5.1. Formation of recombinant DDX3X condensates in the presence of K7. 2 μM DDX3X was incubated with 25 nM Alexa Fluor 647-labeled DDX3X in the absence or presence of 0.25-2 μM K7 for 2 hours at room temperature. 10 μL of each reaction was spotted onto microscope slides, topped with coverslips, and imaged by differential interference contrast microscopy (top images) and fluorescence microscopy (bottom images). Scale bar indicates 10 μm . 20 fluorescence images from each condition were quantified using the nucleus counter tool in ImageJ. n indicates the total number of droplets quantified. Histograms show the distribution of diameters for quantified droplets.

Since no RNA or ATP was present in our measurements, our findings imply that K7 reduces condensate formation of DDX3X by interfering with protein-protein interactions involving the N-terminus. These observations are consistent with our notion that K7 impedes oligomerization of DDX3X and thereby inhibits unwinding and RNA-dependent ATPase activities.

5.3 K7 reduces DDX3X association with cellular stress granules

I next wondered whether K7 inhibited the recruitment of DDX3X to stress granules in cells, which, as noted above, has previously been shown to depend on the N-terminus²²⁰. I measured formation of stress granules in human HCT 116 colon cancer cells following treatment with sodium arsenite, an inducer of

oxidative stress that results in robust stress granule formation³⁷⁵. K7 was introduced transiently via plasmids that co-express myc-tagged K7 and GFP or, as a control, GFP and myc tag alone, to facilitate identification of transfected cells for quantification. Stress granules in GFP-positive cells were visualized by immunostaining for DDX3X or the stress granule marker G3BP1³⁷⁶.

Without K7, DDX3X-positive stress granules readily formed in both, untransfected (**Fig. 5.3**) and GFP- transfected cells (**Fig. 5.2**). K7 expression increased the number of cells without stress granules and decreased the number of stress granules in cells, reflected by a decrease in the number of cells with multiple (> 2) stress granules, compared to measurements without K7 (**Fig. 5.2D**). These observations indicate that K7 expression reduces association of DDX3X with stress granules (**Fig. 5.2**). Similar results were also obtained when only myc-tagged K7 or myc tag were expressed in HCT 116 cells in the absence of GFP (**Fig. 5.3**), indicating that GFP expression did not impact the observed outcomes.

I also examined the impact of K7 on the formation of stress granules marked by the canonical stress granule marker G3BP1 (**Fig. 5.2E-G**). Here, K7 caused a smaller reduction in G3BP1-positive granules, compared to the effect on DDX3X-positive granules (**Fig. 5.2G**). It is possible that K7 affects G3BP1-positive stress granules through depletion of DDX3X, which is considered a constitutive stress granule component²²⁰.

The markedly smaller effect of K7 on G3BP1-positive granules, compared to DDX3X-positive granules, indicates that the observed effect of K7 on DDX3X

association with stress granules is not due to an impact of K7 on the formation of stress granules independent of K7's interactions with DDX3X. Our data show that K7 preferentially interferes with DDX3X association to stress granules. These observations indicate that K7 can modulate the interaction of DDX3X with biomolecular condensates in cells.

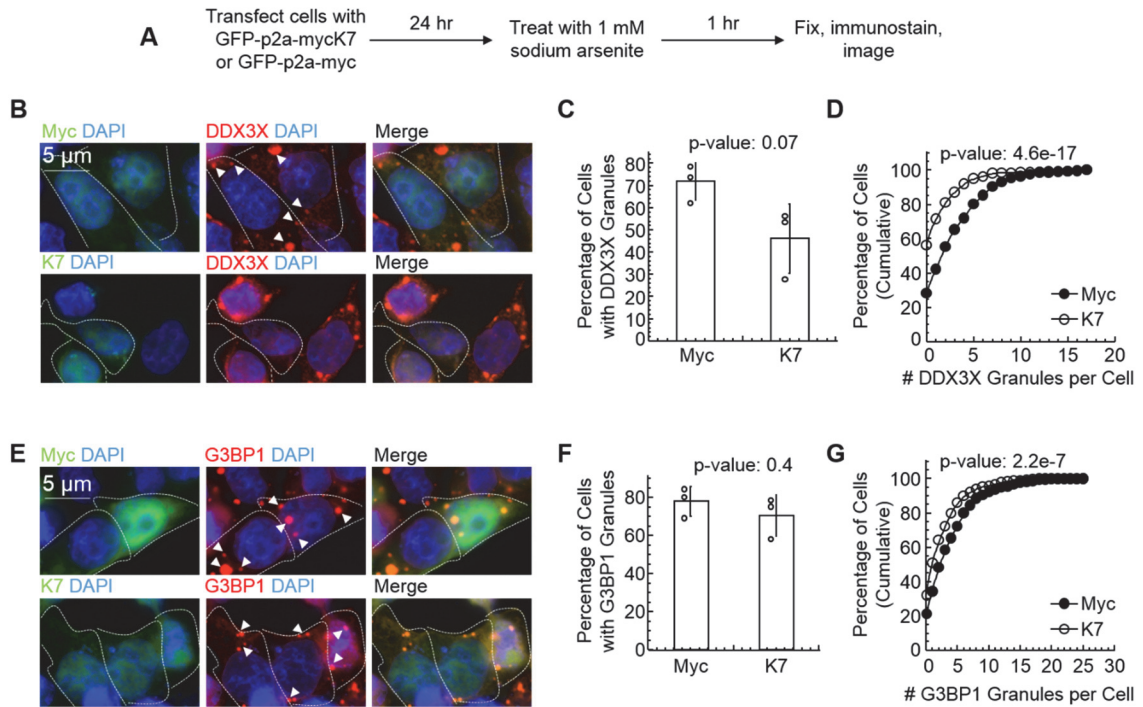


Figure 5.2. Stress granule formation in K7-expressing HCT 116 cells. (A) Timeline of transfection, sodium arsenite treatment, and immunostaining. (B) Representative immunofluorescence images stained for DDX3X in red. DAPI nuclear stain is shown in blue and GFP-positivity is shown in green. (C) Bar graph depicting percentage of cells with DDX3X-positive stress granules. Error bars represent standard deviation from $n \geq 3$ biological replicates (8 images analyzed per replicate, each replicate ≥ 100 cells). p-value from student's two-tailed t-test. (D) Cumulative distribution of all 3 pooled biological replicates ($n = 389$ cells for K7 expression and $n = 432$ cells for myc tag expression) showing the number of DDX3X-positive stress granules forming per cell. p-value from student's two-tailed t-test. (E) Representative immunofluorescence images stained for G3BP1 in red. DAPI nuclear stain is shown in blue and GFP-positivity is shown in green. (F) Bar graph depicting percentage of cells with G3BP1-positive stress granules. Error bars represent standard deviation from $n \geq 3$ biological replicates (8 images analyzed per replicate, each replicate ≥ 100 cells). p-value from student's two-tailed t-test. (G) Cumulative distribution of all 3 pooled

biological replicates (n = 416 cells for K7 expression and n = 438 cells for myc tag expression) showing the number of G3BP1-positive stress granules forming per cell. p-value from student's two-tailed t-test.

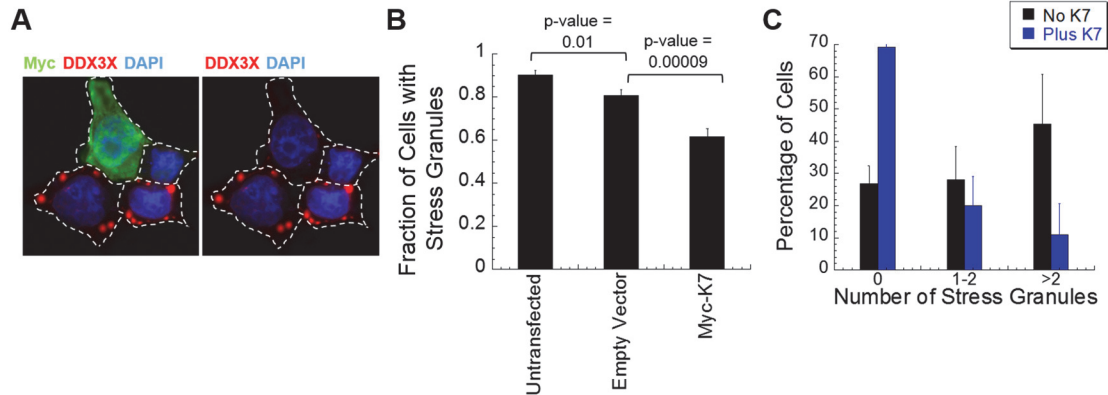


Figure 5.3. Stress granule formation in cells expressing K7 without GFP. (A) Representative fluorescent images showing DDX3X immunostaining in red, myc tag (K7) immunostaining in green, and DAPI nuclear stain in blue. (B) Bar graph showing fraction of cells with DDX3X-positive stress granules. (C) Bar graph showing the number of stress granules per cell in K7-negative and K7-positive cells. Error bars represent standard deviation from n ≥ 3 biological replicates.

5.4 K7 reduces condensate formation by mutant DDX3X in cells

I next probed whether the impact of K7 on DDX3X in cells depended on its interaction with the N-terminus, as seen *in vitro* (Fig. 4.3, 4.4). To accomplish this, I examined the effect of K7 on the formation of aberrant cellular DDX3X condensates that form when certain mutations are present in DDX3X^{62,224}. Several of these mutations are associated with disease phenotypes and impair the catalytic activities of DDX3X^{62,224,230,233}. I focused on measuring the impact of K7 on the formation of aberrant granules formed by DDX3X^{R534H}, a mutation in the helicase motif VI that has been identified in medulloblastoma (an aggressive pediatric brain cancer), in DDX3X syndrome (a neurodevelopmental disorder), and in lymphoma (an immune cell cancer)^{61,222,224,230}. The DDX3X^{R534H} mutation inhibits RNA unwinding by the enzyme *in vitro*²³⁰.

To visualize aberrant DDX3X granules, I co-expressed GFP-tagged DDX3X^{R534H} and myc-tagged K7 or empty myc tag in HCT116 cells. As a control, I also expressed wild-type GFP-tagged DDX3X. Placement of a p2a self-cleaving peptide³⁷⁷ between the K7 (or empty myc tag) and the DDX3X segment resulted in stoichiometric co-expression of myc-tagged K7 and GFP-tagged wild type DDX3X and DDX3X^{R534H} (**Fig. 5.4**).

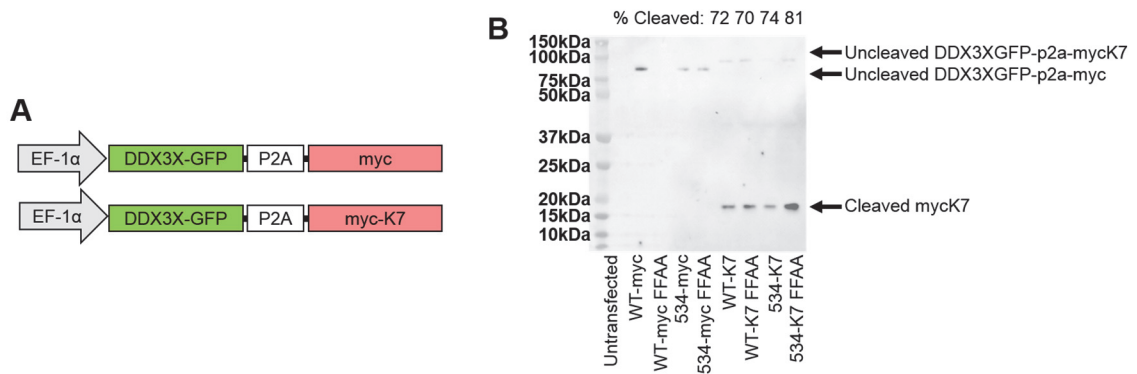


Figure 5.4. Co-expression of GFP-tagged DDX3X and myc-tagged K7 in human cells. (A) Schematic of plasmid design used to co-express GFP-tagged DDX3X and myc-tagged K7 downstream of EF-1 α promoter via usage of a p2a self-cleaving peptide. (B) HCT 116 cells were transfected with plasmids shown in (A) encoding either wildtype DDX3X or DDX3X^{R534H}. The K7 binding site in DDX3X was also mutated (FFAA). Western blotting was performed against the myc tag. 70-81% cleavage at the p2a peptide was observed.

Expression of wild-type DDX3X-GFP (and empty myc tag) in the background of endogenously expressed DDX3X induced GFP-positive foci (**Fig. 5.5**). This outcome is expected, as DDX3X overexpression is known to promote the formation of stress granules²²⁰. Expression of GFP-tagged DDX3X^{R534H} (and empty myc tag), at levels similar to wild-type GFP-tagged DDX3X, markedly increased the formation of aberrant foci, compared to the measurements with wild-type GFP-tagged DDX3X (**Fig. 5.5**). These results are consistent with previous reports^{61,224}.

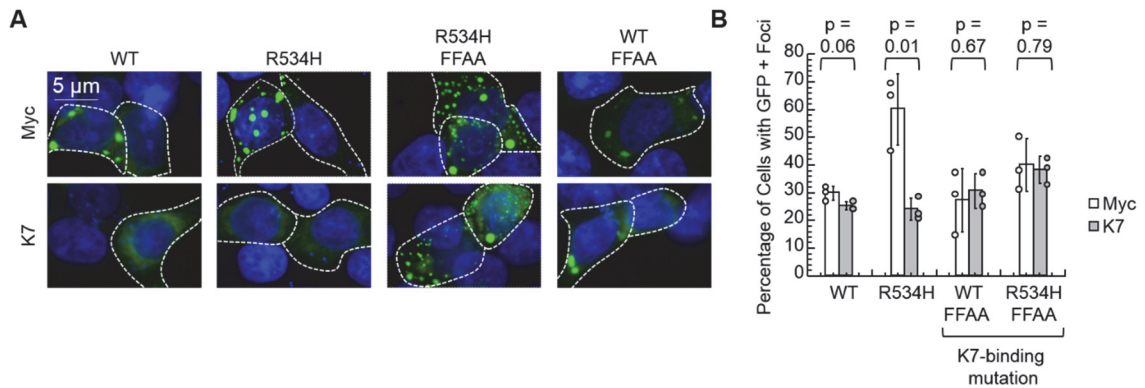


Figure 5.5. Formation of granules with mutant DDX3X in K7-expressing cells. (A) HCT 116 cells were transfected with plasmids utilizing a p2a self-cleaving peptide to co-express GFP-tagged wildtype DDX3X (WT) or DDX3X^{R534H} (R534H) with either myc-tagged K7 or empty myc tag. The K7 binding site was also mutated (FFAA). Representative microscopy images are shown. GFP is shown in green, and DAPI nuclear stain is shown in blue. (B) Bar graph showing the percentage of GFP-positive cells that formed GFP-positive (DDX3X-positive) foci. Error bars represent standard deviation from $n \geq 3$ biological replicates ($n = 115$ cells for each replicate). p-values obtained via student's two-tailed t-test.

To examine the impact of K7 on the formation of these aberrant DDX3X foci, I co-expressed myc-tagged K7 with GFP-tagged DDX3X and GFP-tagged DDX3X^{R534H}. Co-expression of K7 did not change the protein level of GFP-tagged DDX3X^{R534H} or GFP-tagged wild-type DDX3X, compared to the experiments without K7 (Fig. 5.6). K7 expression reduced the number of cells with GFP-positive foci when co-expressed with wild-type-DDX3X, compared to the experiment without K7 (Fig. 5.5). I observed an even larger reduction of GFP-positive foci with DDX3X^{R534H}, compared to the experiment without K7 (Fig. 5.5). These observations show that K7 interferes with the formation of aberrant DDX3X foci in cells.

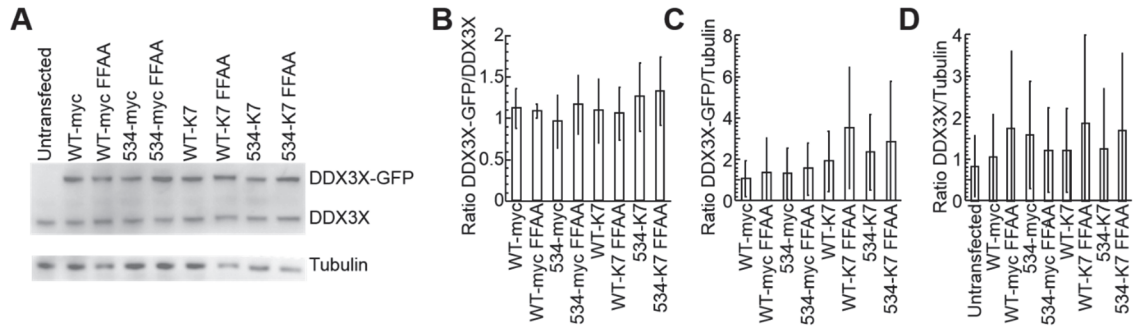


Figure 5.6. Expression of mutant GFP-tagged DDX3X in human cells. (A) HCT 116 cells were transfected with plasmids utilizing a p2a self-cleaving peptide to co-express wildtype DDX3X or DDX3X^{R534H} with either myc-tagged K7 or empty myc tag. The K7 binding site was also mutated (FFAA). Western blotting was performed against DDX3X and tubulin. **(B)** Quantification of western blots to determine level of DDX3X-GFP relative to endogenous DDX3X. **(C)** Quantification of western blots to determine level of DDX3X-GFP relative to tubulin. **(D)** Quantification of western blots to determine level of endogenous DDX3X relative to tubulin. Error bars represent standard deviation from $n \geq 3$ biological replicates.

I then tested whether this interference was due to direct interactions between K7 and DDX3X. To this end, I mutated phenylalanines 84 and 85 in the K7 binding site in the DDX3X N-terminus into alanines. Mutation of phenylalanines 84 and 85 had been previously reported to eliminate K7 binding to DDX3X *in vitro*³⁶⁴. Inclusion of this FFAA mutation did not impact wild-type DDX3X or DDX3X^{R534H} expression and did not alter the formation of aberrant foci (**Fig. 5.5, 5.6**). However, the impact of K7 on the formation of aberrant DDX3X^{FFAA/ R534H} foci was eliminated (**Fig. 5.5**). This observation indicates that K7 interacts with the N-terminus of DDX3X in cells and that this interaction is critical for the inhibition of aberrant DDX3X foci by K7.

5.5 Discussion

As shown in this chapter, K7 binding to DDX3X inhibits the formation of DDX3X-containing condensates *in vitro* and in human cells. K7's ability to

prevent the formation of DDX3X condensates in the absence of RNA and ATP provides further evidence that K7 binding likely prevents DDX3X oligomerization, as proposed in Chapter 4.

K7's stronger inhibition of DDX3X recruitment to stress granules compared to G3BP1 recruitment to stress granules suggests that K7 preferentially targets DDX3X over other stress granule components, consistent with my finding that K7 binding to DDX3X is required for K7 to reduce mutant DDX3X granule formation (**Fig. 5.5**). Additionally, my data suggests that while DDX3X is considered an essential stress granule factor²²⁰, loss of DDX3X is not sufficient to totally inhibit stress granule formation.

The formation of G3BP1-positive stress granules following sodium arsenite treatment in K7-expressing cells is consistent with prior studies where VACV-infected cells treated with sodium arsenite formed G3BP1-positive stress granules³⁷⁸. However, in this prior study the level of G3BP1-positive stress granule induction was not quantified relative to uninfected cells, so a slight decrease in G3BP1-positive stress granules, as seen in my data (**Fig. 5.2**), would not have been detected³⁷⁸. Since DDX3X association with stress granules occurs downstream of eIF2 α phosphorylation, VACV targeting of DDX3X by K7 and VACV inhibition of eIF2 α phosphorylation by E3L and K3L³⁶⁹ may work synergistically to prevent stress granule/AVG formation. Thus, K7 binding to DDX3X may represent one of many parallel pathways used by VACV to reduce stress granule/AVG formation.

This multipronged approach to reduce and/or manipulate stress granule formation is employed by several other viruses that target DDX3X. For example, the NS1 protein produced by influenza A virus binds to DDX3X and reduces its association with stress granules formed during viral infection, but also inhibits the upstream phosphorylation of eIF2 α ^{348,379}. Similarly, hepatitis C virus redistributes DDX3X and other stress granule components (G3BP1, etc.) from stress granules to viral replication sites^{338,380}. Thus, in addition to the benefit of targeting DDX3X to reduce innate immune signaling as described in Chapter 3 (**Fig. 3.4**), viral targeting of DDX3X also benefits viruses by manipulating the formation of antiviral stress granules.

Finally, one of the most exciting findings in my thesis is K7's ability to disrupt mutant DDX3X granules. Formation of these granules is pathogenic during the development of DDX3X syndrome²²⁴, and likely also contributes to the development of several cancers^{61,62,222,230,240}. Thus, K7's well-defined binding site in DDX3X's N-terminus constitutes an ideal target for the development of granule-modulating therapeutics to be used in the treatment of DDX3X syndrome and the various cancers where granule-inducing DDX3X mutations occur (medulloblastoma, lymphoma, etc.^{61,62,222,230,240}). The next chapter describes K7's effects on cell growth/viability and the role of DDX3X in translation initiation.

Chapter 6

The viral protein K7 has minimal effects on global translation

6.1 Introduction

As described in Chapter 3, both DDX3X and its yeast homolog Ded1p facilitate translation of structured mRNAs^{59-61,63,64,116,219,255}. Ded1p was shown to facilitate scanning by remodeling the structured 5'-UTRs of mRNAs, thereby preventing translation from upstream alternative translation initiation sites⁵⁹. Several lines of evidence indicate that DDX3X functions similarly to promote translation in human cells^{60,61,255-257}.

As shown in Chapter 4, the vaccinia virus (VACV) protein K7 inhibits DDX3X's RNA helicase activity *in vitro*. Given that DDX3X's helicase activity allows it to remodel structured mRNAs, I wondered if K7 would also inhibit DDX3X's promotion of translation on structured mRNAs. Additionally, DDX3X associates with eIF4E, an eIF4F subunit, via its N-terminal residues 38-44^{220,381}. These residues are near the K7 binding interface (DDX3X residues 81-90)³⁶⁴. Thus, K7 binding to DDX3X could potentially compete for eIF4E binding and reduce DDX3X association with the translation initiation complex.

VACV employs several mechanisms to co-opt the host translational machinery for viral protein synthesis³⁶⁹, as detailed in section 5.1. VACV also produces several enzymes that degrade host mRNAs³⁸². Both of these effects combine to globally reduce host protein synthesis, while increasing viral protein synthesis³⁸². However, ribosome profiling performed in VACV-infected cells revealed that several host proteins are upregulated during VACV infection³⁸³.

The majority of these translationally upregulated proteins had short unstructured 5'-UTRs and were involved in the oxidative phosphorylation pathway³⁸³, which VACV has previously been shown to depend on for increased ATP usage during productive infection³⁶⁹. VACV transcripts also contain short, low complexity 5'-UTRs and are translationally upregulated during viral infection^{382,383}, suggesting that selective enhancement of both viral translation and the translation of host oxidative phosphorylation proteins occurs via similar mechanisms sparing translation of mRNAs with short 5'-UTRs.

As noted above, DDX3X preferentially promotes translation of transcripts with structured 5'-UTRs, which includes several transcripts encoding pro-inflammatory proteins upregulated during the immune response^{60,257}. Thus, VACV's inhibition of DDX3X RNA helicase activity by K7 binding may serve to prevent translation of these and other structured host transcripts, without impacting translation of transcripts with short 5'-UTRs (oxidative phosphorylation mRNAs, viral mRNAs, etc.). To test K7's impact on global translation we employed two parallel approaches: transfection of K7 into HCT 116 cells followed by (i) polysome profiling or (ii) puromycin labeling of nascent polypeptides.

6.2 K7 does not impact DDX3X association with the ribosome

As noted above, both K7 and eIF4E interact with DDX3X's N-terminal extension^{220,364,381}. Interactions between eIF4E and DDX3X likely play a role in mediating DDX3X's association with the translation initiation complex. To test whether K7 binding interferes with DDX3X's association with the translation machinery in human cells, I transfected cells with plasmids utilizing a p2a self-

cleaving peptide³⁷⁷ to co-express stoichiometric amounts of GFP and myc-tagged K7 or GFP and myc tag alone as a transfection control (**Fig. 6.1**).

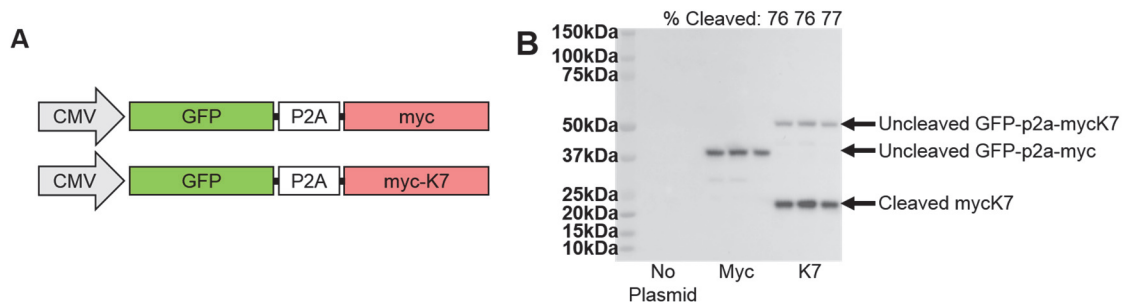


Figure 6.1. Co-expression of GFP and myc-tagged K7 in human cells. (A) Schematic of plasmids utilizing a p2a self-cleaving peptide to co-express GFP and myc-tagged K7 or myc tag alone downstream of a CMV promoter. **(B)** Plasmids shown in **(A)** were transfected into HCT 116 cells. Western blotting against the myc tag was performed. ~76% cleavage at the p2a peptide was observed.

These transfections resulted in approximately 30-50% GFP-positive cells for both the K7-expressing cells and the transfection control (myc tag-expressing) cells (**Fig. 6.2**). Polysome traces generated from the K7-transfected cells did not differ from the transfection control (myc tag-expressing) cells (**Fig. 6.2**), suggesting that K7 expression does not globally inhibit host cell translation. Western blotting for DDX3X in each fraction of the polysome revealed enrichment of DDX3X in the 40S fractions, consistent with its role in translation initiation. No significant difference in DDX3X distribution across the polysome trace could be observed when comparing K7-transfected cells to myc tag-transfected control cells (**Fig. 6.2**).

Although no significant changes in polysome number or DDX3X association with actively translating complexes could be detected following transfection with K7-expressing plasmids (**Fig. 6.2**), it is unclear whether this result is due to an actual lack of effect from K7 binding or due to the high

background of cells (over half the measured population) that do not express K7 following transfection.

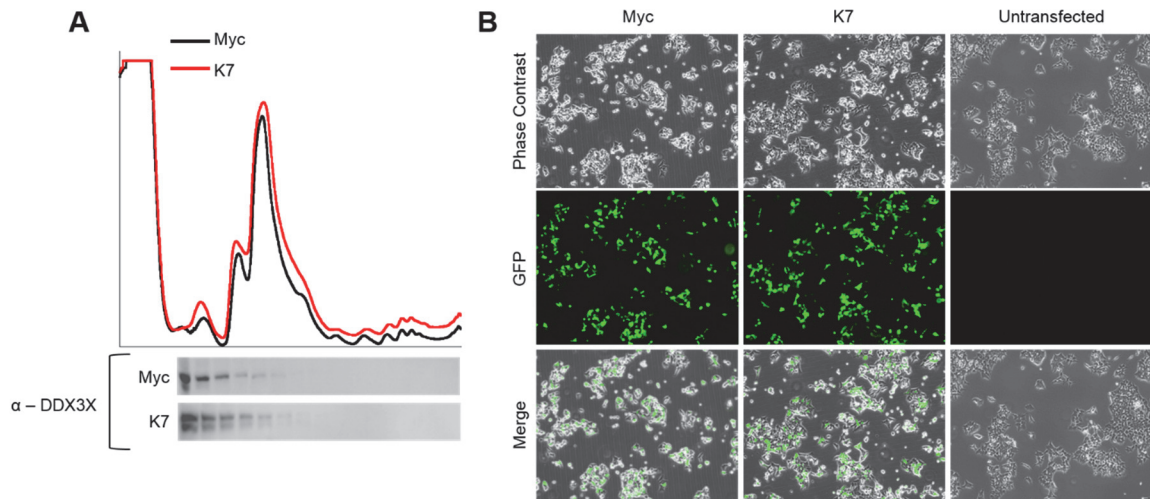


Figure 6.2. Impact of K7 on DDX3X association with translating ribosomes. (A) Polysome traces obtained from cells co-expressing GFP and myc-tagged K7 or GFP and myc tag alone. Proteins from each fraction were precipitated and run on SDS-PAGE. Western blotting was performed against DDX3X. Polysome traces were generated by Brittany Stawicki. n = 1 biological replicate. (B) Representative microscope images showing the transfection efficiency (percentage of GFP-positive cells) at the time of cell lysis.

6.3 K7 slightly reduces global translation

To overcome the limitations of transient transfection where less than 50% of cells express K7, I decided to measure translation using puromycin labeling. Puromycin is incorporated into nascent polypeptides, and the level of puromycin incorporation can be quantified via flow cytometry, western blot, or immunofluorescence using anti-puromycin antibodies³⁸⁴. By performing immunofluorescence against puromycin, I was able to measure the level of translation in only the GFP-positive (K7-expressing or myc tag-expressing control) transfected cells, thereby reducing the background signal from the non-expressing cells. Quantification of the puromycin signal in GFP-positive cells

revealed that K7 expression caused a small but statistically significant decrease in global translation relative to myc tag control cells (puromycin signal intensity in K7-expressing cells was reduced by approximately 14% compared to control transfected cells) (**Fig. 6.3**). This result is consistent with the largely unchanged polysome traces (**Fig. 6.2**) and growth rate (**Fig. 6.4**) observed following K7 transfection. These results suggest that K7 binding either does not inhibit DDX3X function during translation or that DDX3X is only required for translation of a few transcripts in HCT 116 cells, as has recently been reported^{60,223}.

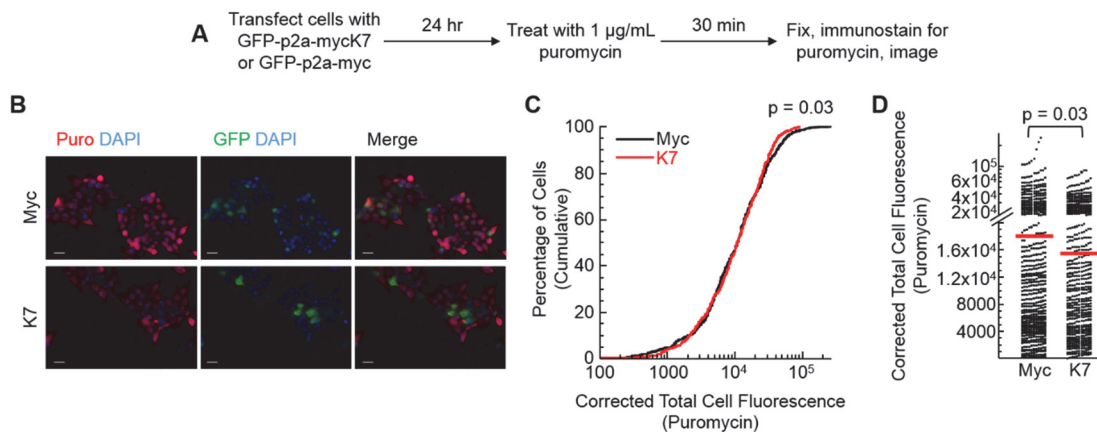


Figure 6.3. Global translation in K7-expressing cells. (A) Timeline for transfection, puromycin labeling, and immunostaining of HCT 116 cells (B) Representative microscope images taken at 40X showing GFP (co-expressed with myc-tagged K7 or myc tag control) in green, DAPI nuclear stain in blue, and puromycin immunostaining in red. Scale bar represents 20 μm . (C,D) The corrected total cell fluorescence (puromycin intensity) for each GFP-positive cell was quantified in ImageJ for $n = 3$ biological replicates (8 images taken at 40X analyzed per replicate). All 3 replicates were pooled ($n = 603$ total cells for myc-tagged K7 co-expression and $n = 637$ total cells for myc tag control co-expression) and the cumulative distribution of puromycin staining intensities (C) was plotted. The 3 pooled biological replicates were also plotted as a scatterplot (D). Each dot represents the corrected total cell fluorescence (puromycin intensity) measured for one cell. Break in the y-axis represents a switch from linear scale for the bottom half of the plot to log scale for the top half of the plot. Red bars mark the average corrected total cell fluorescence (puromycin intensity). P-value from student's two-tailed t-test.

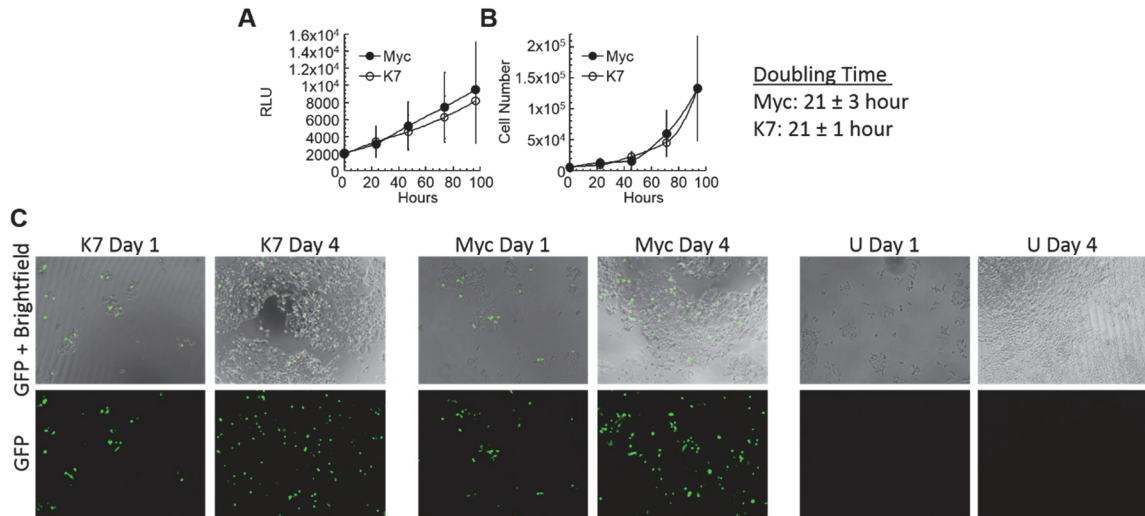


Figure 6.4. Viability and growth of K7-expressing cells. (A) CellTiter-Glo viability measurements were performed on HCT 116 cells transfected with plasmids co-expressing GFP and myc-tagged K7 or GFP and myc tag. (B) HCT 116 cells were plated then transfected with plasmid co-expressing GFP and myc-tagged K7 or GFP and myc tag. Cell number was counted each day. Doubling times were calculated from the resulting growth curve. (C) Representative microscope images showing the level of GFP-positivity (myc-tagged K7/myc tag expression) over the duration of the experiment.

To test the requirement of DDX3X for global translation in HCT 116 cells, we obtained HCT 116 cells exclusively expressing degron-tagged DDX3X from Dr. Stephen Floor's laboratory at University of California San Francisco⁶⁰. Dr. Floor's laboratory performed ribosome profiling on these cells before and after inducibly depleting degron-tagged DDX3X to reveal that DDX3X is required for efficient translation of 808 structured transcripts in HCT 116 cells (out of 19,965 measured transcripts)⁶⁰. My labmate Brittany Stawicki generated polysome traces from these cells before and after DDX3X depletion, as confirmed by western blotting (Fig. 6.5). Consistent with Dr. Floor's ribosome profiling study⁶⁰, the polysome traces were largely similar in the presence and absence of DDX3X (Fig. 6.5). This finding mirrors our results following K7-mediated inhibition of DDX3X helicase activity (Fig. 6.2, 6.3). However, immunofluorescence of the

cells expressing degron-tagged DDX3X revealed that the CRISPR knock-in of the tag onto DDX3X's C-terminus largely altered DDX3X localization and caused the formation of cytoplasmic DDX3X foci, as opposed to the diffuse cytoplasmic distribution of wildtype untagged DDX3X (**Fig. 6.6**). Thus, DDX3X function during translation may be partially inhibited by the presence of the degron-tag, reducing the effect observed upon depletion of degron-tagged DDX3X. However, RNAi-mediated knockdown of DDX3X in HEK293T cells performed in parallel by Dr. Floor's laboratory negatively impacted translation from an even smaller number of transcripts (230 out of 19,965 detected transcripts), suggesting that the altered localization of degron-tagged DDX3X did not reduce the effect of DDX3X depletion⁶⁰.

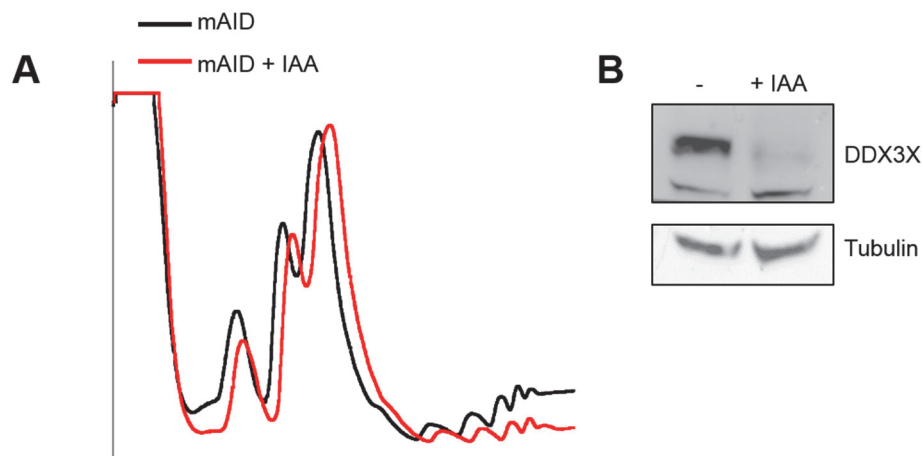


Figure 6.5. Global translation in DDX3X-depleted cells. (A) Polysome traces obtained from degron-tagged DDX3X cells before DDX3X depletion (mAID, in black) and after DDX3X depletion (mAID + IAA, in red). mAID is the name of the degron system used. IAA is the hormone used to induce depletion of degron-tagged DDX3X. Polysome traces were generated by Brittany Stawicki. (B) Western blotting against DDX3X in cells harvested before (-) and after (+ IAA) DDX3X depletion. n = 1 biological replicate.

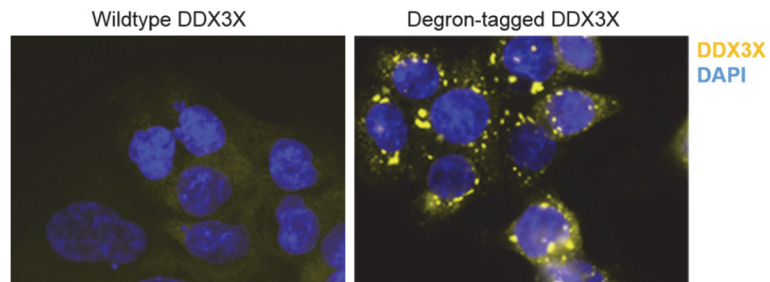


Figure 6.6. Localization of degron-tagged DDX3X. Representative microscope images of wildtype HCT 116 cells (untagged DDX3X, left panel) and HCT 116 cells where endogenous DDX3X has been tagged with a C-terminal degron tag (degron-tagged DDX3X, right panel). DDX3X immunostaining is shown in yellow and DAPI nuclear stain is shown in blue.

6.4 Discussion

The helicase Ded1p is thought to facilitate translation of the majority of yeast transcripts by associating with the translation initiation complex and remodeling mRNA secondary structures^{59,63,64}. DDX3X also associates with the translation initiation complex and promotes translation of structured mRNAs^{60,61,255-257}; however, several studies suggest that DDX3X is required for efficient translation from only a subset of human transcripts, in contrast to Ded1p's more widespread role^{60,223}. Similarly, although RNAi-mediated knockdown of DDX3X in several melanoma cell lines reduced global translation by nearly 50% as measured by [³⁵S] labeling, only about 400 transcripts (out of ~40,000 detected transcripts) were found to have reduced translational efficiency via ribosome profiling²²³. Furthermore, ribosome profiling performed on the dissected brain cortices of embryonic mice identified only 147 transcripts that had reduced translational efficiency in DDX3X conditional knockout mice²⁴¹. Thus, it

seems likely that DDX3X is not required for efficient translation of the majority of mammalian transcripts. However, reduced translation of DDX3X-dependent transcripts has biologically relevant effects during neurogenesis and tumorigenesis^{223,241}.

Several pro-inflammatory mRNAs, including STAT1 (an interferon-activated transcription factor), Rac1 (required for phagocytosis), and TAK1 (involved in cytokine signaling) require DDX3X for efficient translation²⁵⁷. Based on our data, we cannot draw any conclusions as to whether or not K7-mediated inhibition of DDX3X impacts these pro-inflammatory DDX3X-dependent transcripts, though it's likely that reduction of these proteins would be beneficial for VACV infection. To test these transcript-specific translational changes, we could generate a stable K7-expressing cell line wherein all cells express K7 and the background non-expressing cells observed after transient transfection are eliminated. We could then perform polysome profiling followed by RT-qPCR to see if K7 binding inhibits translation of specific DDX3X-dependent transcripts.

Collectively, our data demonstrates that K7 expression in human cells does not drastically reduce global translation or impact growth rates for HCT 116 human colon cancer cells. This is consistent with studies from other cell lines that found only a subset of transcripts depended on DDX3X for efficient translation^{60,223}. Additional studies are needed to determine whether K7-mediated inhibition of DDX3X *in vitro* correlates with reduced translation of DDX3X-dependent transcripts.

Chapter 7

Modulation of DDX3X condensate formation by small molecules

7.1 Introduction

In addition to protein-protein interactions that modulate the formation of biomolecular condensates via LLPS, such as the interaction between K7 and DDX3X described here or the multivalent protein-protein interactions that underlie condensate formation, various small molecules (such as metabolites) also influence the properties and dynamics of biomolecular condensates¹⁵⁰. Given that dysregulation of biomolecular condensates occurs in various cancers and neurodegenerative diseases, multiple efforts are underway to identify and develop small molecules that can be used to therapeutically modulate biomolecular condensates³⁸⁵⁻³⁸⁸. Traditional approaches to regulate biomolecular condensates via protein binding pocket-ligand interactions include the use of small molecules to control the phosphorylation status of eIF2 α and 4EBP-1 and thereby regulate stress granule formation, small molecules that alter the microtubule/cytoskeleton components that traffic biomolecular condensates within the cell, and small molecules that regulate enzymes that add/remove condensate-regulating post-translational modifications to proteins^{385,386}.

Alternatively, the physicochemical properties of biomolecular condensates can be targeted directly. For example, 1,6-hexanediol alters hydrogen bonding and hydrophobic interactions to nonspecifically disrupt LLPS and biomolecular condensates³⁸⁶. Similarly, TMAO (trimethylamine N-oxide) is a chemical chaperone that stabilizes protein structures and inhibits progression of TDP-43

condensates into pathological fibrils³⁸⁹. Cell-based high throughput screens have identified small molecules that disrupt stress granules by targeting RNA-RBP interactions underlying stress granule formation or by altering the properties of condensate-associated proteins^{390,391}. Several small molecules that directly bind to disordered protein regions have also been identified³⁹²⁻³⁹⁵, raising the possibility of specifically targeting protein IDRs to manipulate LLPS and biomolecular condensates.

In my previous thesis chapters, I demonstrated the ability of protein-protein interactions between the viral protein K7 and DDX3X's N-terminal IDR to prevent DDX3X LLPS. In this chapter, I present work showing that the small molecule bis-ANS (4,4'-dianilino-1,1'-binaphthyl-5,5'-disulfonic acid) and various free amino acids also regulate LLPS by DDX3X and its yeast homolog Ded1p.

7.2 Bis-ANS exerts biphasic effects on liquid-liquid phase separation

This section was adapted from Nat Commun, Babinchak WM, Dumm BK, Venus S, Boyko S, Putnam AA, Jankowsky E, Surewicz WK, Small molecules as potent biphasic modulators of protein liquid-liquid phase separation (2020) under the terms of the Creative Commons License (<http://creativecommons.org/licenses/by/4.0/>).

Bis-ANS is a fluorescent bivalent naphthalene sulfonate (**Fig. 7.1**) used to monitor protein aggregates and exposed hydrophobic patches of proteins³⁹⁶.

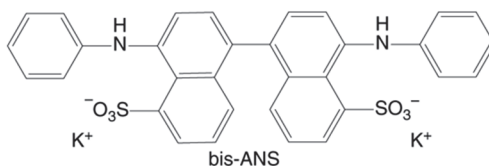


Figure 7.1. Chemical structure of bis-ANS (4,4'-dianilino-1,1'-binaphthyl-5,5'-disulfonic acid). Figure is adapted from³⁹⁶ under the terms of the Creative Commons License (<http://creativecommons.org/licenses/by/4.0/>).

Bis-ANS promotes LLPS by TDP-43's low complexity domain *in vitro* at ratios <2:1 bis-ANS to protein, but reduces/dissolves TDP-43 low complexity domain condensates at ratios >2:1 bis-ANS to protein³⁹⁶. This effect mirrors typical reentrant phase transitions induced by RNA: RNA at low concentrations promotes LLPS, while RNA at high concentrations inhibits LLPS³⁹⁶. However, unlike typical reentrant phase transitions driven by electrostatic interactions between RNA and protein, interactions between bis-ANS and protein are primarily hydrophobic, not electrostatic³⁹⁶. Dr. Michael Babinchak tested the generalizability of these findings by measuring the effect of bis-ANS on the LLPS of FUS, tau, and Ded1p (the yeast homolog of DDX3X) (**Fig. 7.2**). He found that the effects of bis-ANS on all three proteins mirrored those observed with the low complexity domain of TDP-43³⁹⁶. Thus, the interactions between bis-ANS and disordered proteins are nonspecific and generalizable to numerous proteins that undergo LLPS.

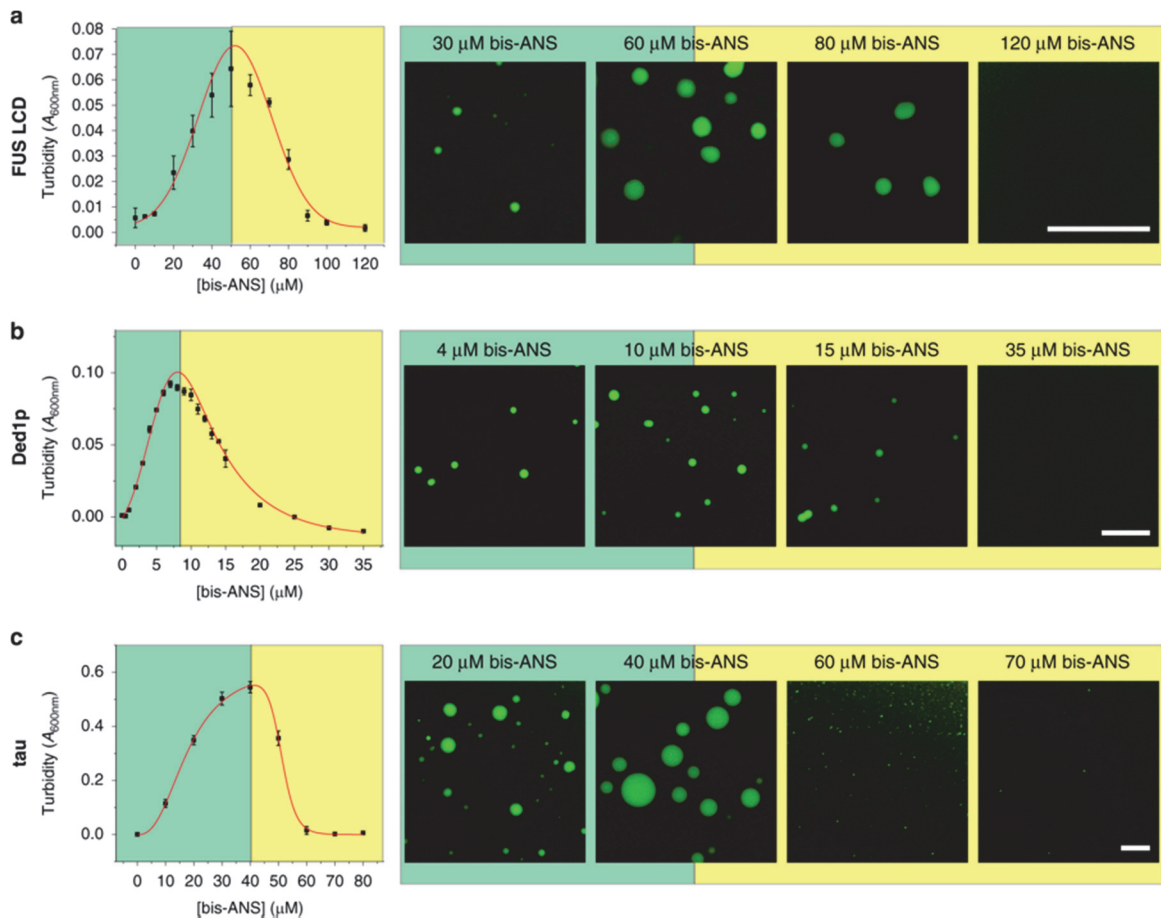


Figure 7.2. Impact of bis-ANS on LLPS. Turbidity curves and representative fluorescence microscopy images of (a) 20 μM FUS low complexity domain, (b) 1 μM Ded1p, and (c) 10 μM tau in the presence of bis-ANS. Scale bars indicate 10 μm . Error bars indicate standard deviation from 3 technical replicates. Experiments were performed by Dr. Michael Babinchak. Figure is adapted from³⁹⁶ under the terms of the Creative Commons License (<http://creativecommons.org/licenses/by/4.0/>).

We then tested the effect of bis-ANS on LLPS in cells. Ben Dumm found that bis-ANS was nontoxic at concentrations $< 400 \mu\text{M}$ (**Fig. 7.3A**) and that bis-ANS interacts with and fluorescently labels numerous hydrophobic structures within the cell (**Fig. 7.3B**)³⁹⁶. Due to this nonspecific staining, we decided to use immunofluorescence against the canonical stress granule protein G3BP1 to quantify changes in stress granule dynamics upon treatment with bis-ANS. I

treated HCT 116 colon cancer cells with 500 μ M sodium arsenite for 30 min, then washed out the sodium arsenite, added fresh media containing 250 μ M bis-ANS dissolved in PBS (or media with PBS alone) and fixed/immunostained cells 60, 90, and 120 min after removing the sodium arsenite (**Fig. 7.3C**). 20 images from each condition were analyzed using the Cell Counter feature in ImageJ. We found that presence of bis-ANS stabilized stress granules and increased the time for them to dissolve after removal of stress (typically 90 minutes in the absence of bis-ANS vs. > 120 minutes in the presence of bis-ANS) (**Fig. 7.3D,E**)³⁹⁶. Of note, bis-ANS treatment alone did not induce the presence of stress granules, confirming that bis-ANS treatment stabilized pre-formed stress granules (**Fig. 7.4**)³⁹⁶.

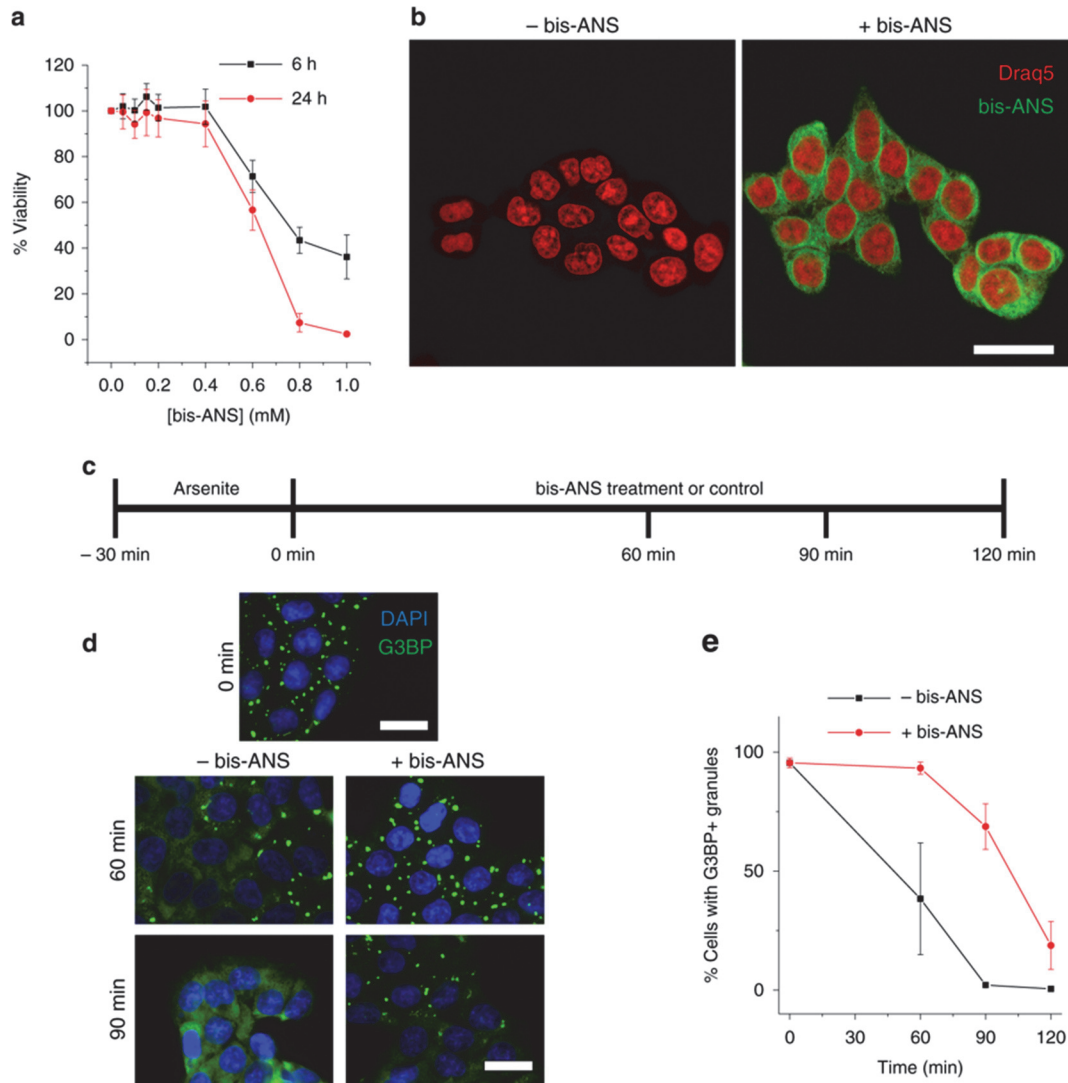


Figure 7.3. Impact of bis-ANS on stress granules. (a) HCT 116 viability upon treatment with bis-ANS for 6 or 24 hr as determined by MTT assay. Error bars represent standard deviation from $n = 5$ technical replicates across 2 biological replicates. Experiments were performed by Ben Dumm. (b) Live-cell images of HCT 116 cells before and after 1 hr treatment with 250 μM bis-ANS (green). Nuclei were stained with Draq5 (red). Scale bar represents 20 μm . Experiments were performed by Ben Dumm. (c) Timeline for treatment of HCT 116 cells with sodium arsenite and/or 250 μM bis-ANS. (d) Representative microscope images following sodium arsenite washout and bis-ANS treatment. Stress granule marker G3BP1 is stained in green and DAPI nuclear stain is shown in blue. (e) 20 images from each condition were analyzed using the Cell Counter tool in ImageJ. The percentage of cells containing G3BP1-positive stress granules at each time point are shown. Scale bars represent 20 μm . Error bars represent standard deviation from $n = 3$ biological replicates. Figure is adapted from³⁹⁶ under the terms of the Creative Commons License (<http://creativecommons.org/licenses/by/4.0/>).

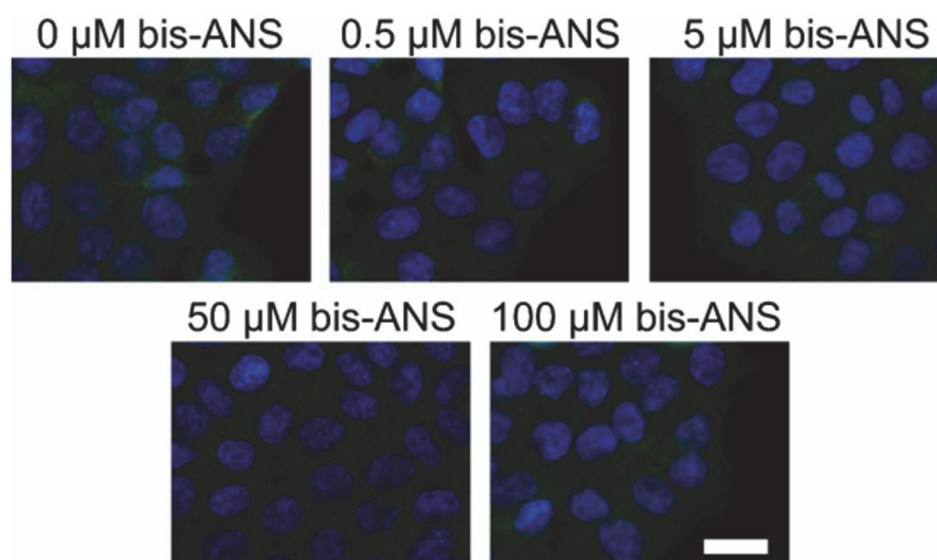


Figure 7.4. Treatment with bis-ANS does not induce stress granule formation. HCT 116 cells were treated with bis-ANS for 2 hr, then fixed and immunostained against G3BP1 (green). DAPI nuclear stain is shown in blue. Scale bar represents 20 μm . Figure is adapted from³⁹⁶ under the terms of the Creative Commons License (<http://creativecommons.org/licenses/by/4.0/>).

These findings represent an exciting development in our understanding of using small molecules to regulate the physicochemical properties of protein condensates. Bis-ANS utilizes predominantly hydrophobic interactions along its bivalent aromatic groups to promote LLPS at low concentrations and inhibit LLPS at high concentrations *in vitro*³⁹⁶. In the cell, bis-ANS was found to stabilize stress granules, indicating that these LLPS-modulating effects also occur in a physiological setting³⁹⁶. Lack of stress granule dissolution in the presence of bis-ANS likely indicates that the effective concentration within the cell was relatively low (LLPS-promoting)³⁹⁶. The physicochemical characterization of bis-ANS and its interactions with proteins that undergo LLPS³⁹⁶ provides useful insight for the design of new condensate-modulating therapies.

7.3 Amino acids regulate Ded1p/DDX3X liquid-liquid phase separation

Portions of this section were adapted with permission from Cell Rep, Krokowski D, Jobava R, Szkop KJ, Chen CW, Fu X, Venus S, Guan BJ, Wu J, Gao Z, Banaszuk W, Tchorzewski M, Mu T, Ropelewski P, Merrick WC, Mao Y, Sevval AI, Miranda H, Qian SB, Manifava M, Ktistakis NT, Vourekas A, Jankowsky E, Topisirovic I, Larsson O, Hatzoglou M, Stress-induced perturbations in intracellular amino acids reprogram mRNA translation in osmoadaptation independently of the ISR (2022).

Cellular conditions including temperature, pH, osmolytes, and metabolites can all influence the behavior of biomolecular condensates¹⁵⁰. Recently, ATP was found to act as a hydrotrope to promote protein solubility, with high ATP concentrations (~ 8 mM) inhibiting protein LLPS *in vitro*³⁹⁷. Interestingly, in unpublished work from our laboratory, Dr. Andrea Putnam found that 2 mM ATP promoted the formation of Ded1p protein condensates *in vitro* in the presence of the crowding agent PEG, suggesting that ATP may have varied roles depending on its concentration and the presence of other molecules. Regardless, several biomolecular condensates are responsive to cellular ATP concentrations³⁹⁸.

Other metabolites in the cell, such as carbohydrates and amino acids, can similarly act as stabilizing osmolytes that promote protein folding and solubility³⁹⁹. However, the effects of these osmolytes on LLPS have not been well characterized. To address this question, I measured the ability of Ded1p to form protein condensates *in vitro* in the presence of various amino acids. 100 mM proline, glutamine, leucine, and asparagine all reduced the formation of Ded1p condensates (**Fig. 7.5**). Given that proline has previously been found to reduce protein aggregation *in vitro*⁴⁰⁰, we chose to further examine proline's effects. Proline concentrations above 200-400 mM nearly abolished the formation of Ded1p and DDX3X condensates *in vitro* (**Fig. 7.6**). While these concentrations

are significantly higher than the free proline concentration in human cells (~ 50-100 μM in HEK293T cells⁴⁰¹), these findings suggest that proline may regulate protein LLPS in addition to its anti-aggregation effects. This effect is of particular interest in the setting of osmotic and oxidative stress, where intracellular amino acid levels (including proline) increase to protect the cell and promote stress adaptation⁴⁰¹⁻⁴⁰³. This increase in intracellular amino acids is driven in part by the amino acid transporter SNAT2 that gets upregulated during osmotic stress⁴⁰⁴. Inhibition of SNAT2 reduces the stress-induced increase in intracellular amino acid concentrations and also prolongs the presence of stress granules during osmotic stress⁴⁰⁴. These cellular results mirror our *in vitro* findings where high proline concentrations reduced liquid-liquid phase separation by DDX3X, suggesting that increases in intracellular amino acids during the stress response may play a role in the dissolution of stress-induced condensates.

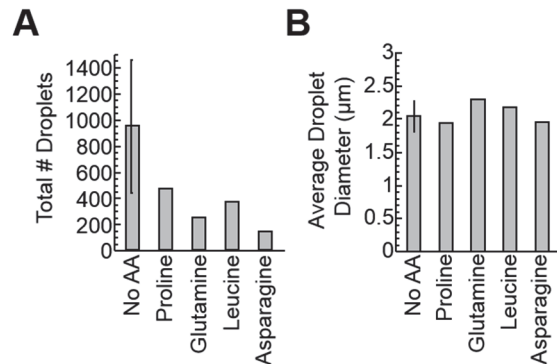


Figure 7.5. Effect of free amino acids on Ded1p condensate formation. 4 μM Ded1p was incubated with 100 mM of various amino acids (or no amino acid (no AA)) for 1 hr at 25 $^{\circ}\text{C}$. 10 μL of each reaction was then spotted on a microscope slide, covered with a coverslip, and imaged at 20X. 20 images from each condition were quantified using the nucleus counter tool in ImageJ. **(A)** Total # of droplets quantified from 20 images. $n = 1$ technical replicate except for no AA, which has 3 replicates (error bars represent 1 standard deviation). **(B)** Average diameter of droplets quantified. $n = 1$ technical replicate except for no AA, which has 3 replicates (error bars represent 1 standard deviation).

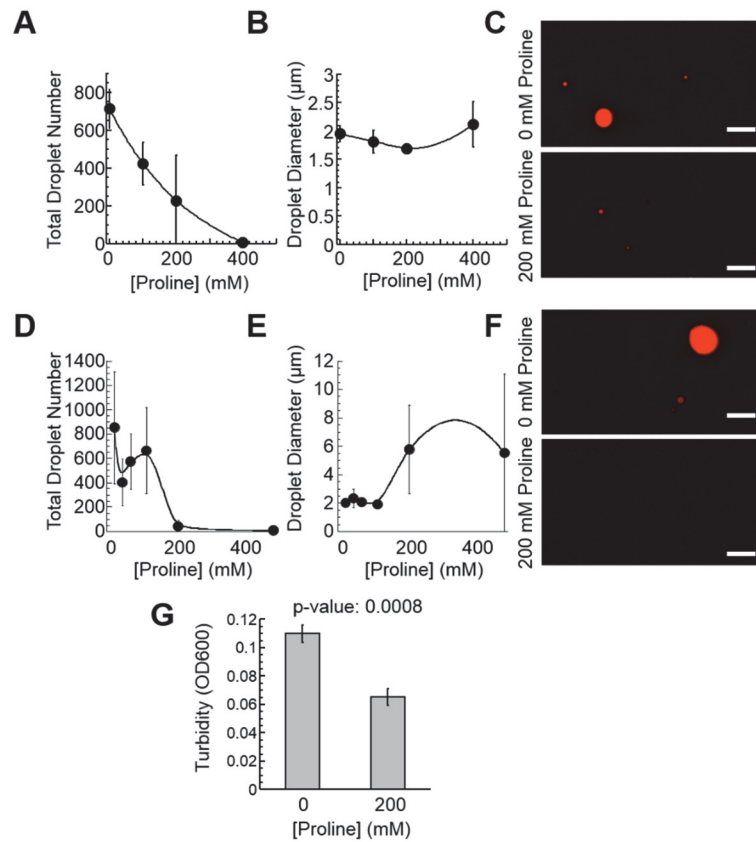


Figure 7.6. Impact of proline on DDX3X and Ded1p condensate formation. 2 μM DDX3X (**A**, **B**, **C**) or 4 μM Ded1p (**D**, **E**, **F**, **G**) was incubated with various concentrations of proline for 1-2 hr at 25 °C. 10 μL of each reaction was then spotted on a microscope slide, covered with a coverslip, and imaged at 20X. 20 images from each condition were quantified using the nucleus counter tool in ImageJ. (**A**) DDX3X: Total # of droplets quantified from 20 images. Error bars represent standard deviation from $n \geq 3$ replicates. (**B**) DDX3X: Average diameter of droplets quantified. Error bars represent standard deviation from $n \geq 3$ replicates. (**C**) DDX3X: Representative fluorescence images. Scale bar represents 10 μm . (**D**) Ded1p: Total # of droplets quantified from 20 images. Error bars represent standard deviation from $n \geq 3$ replicates. (**E**) Ded1p: Average diameter of droplets quantified. Error bars represent standard deviation from $n \geq 3$ replicates. (**F**) Ded1p: Representative fluorescence images. Scale bar represents 10 μm . (**G**) Turbidity (OD₆₀₀) measurements for 2 μM Ded1p incubated with or without 200 mM proline for 1 hour at 25 °C. Error bars represent standard deviation from $n \geq 3$ replicates. P-value derived from student's two-tailed t-test.

7.4 Discussion

Here I have identified additional modulators of DDX3X/Ded1p LLPS: bis-ANS and free amino acids. Bis-ANS is a bivalent small molecule that interacts with hydrophobic regions of proteins to modulate LLPS³⁹⁶. At low concentrations bis-ANS promotes LLPS, while at high concentrations bis-ANS dissolves condensates (**Fig. 7.2**)³⁹⁶. This dual property is appealing in the setting of therapeutics, as the goal is to disrupt pathological condensates without impacting physiological condensates. Dr. Michael Babinchak performed studies with a variety of similar small molecules to identify the bivalent nature of bis-ANS as key for its LLPS-modulating properties³⁹⁶. This study provides important insights for the design of condensate-modulating therapeutics.

Biomolecular condensates are heavily involved in the cellular responses to changing environmental stimuli¹⁵⁰. Thus, biomolecular condensates are responsive to changes in the cellular environment¹⁵⁰. During osmotic and oxidative stress, mammalian cells increase their intracellular concentrations of free amino acids, especially proline⁴⁰¹⁻⁴⁰³. These free amino acids function as osmolytes to promote protein stability and solubility³⁹⁹. Here we show that high concentrations of free amino acids can reduce the formation of DDX3X and Ded1p protein condensates *in vitro* (**Fig. 7.5, 7.6**). We note that the amino acid concentrations used in our *in vitro* studies are significantly higher than measured *in vivo* concentrations of free amino acids⁴⁰⁵. However, recent work from Dr. Maria Hatzoglou's laboratory indicates that increases in intracellular amino acids promote the dissolution of stress granules during cellular adaptation to osmotic

stress⁴⁰⁴. This work provides preliminary evidence that changing concentrations of free amino acids within the cell may modulate the formation of biomolecular condensates. Interestingly, the four amino acids we tested *in vitro* all exhibited similar inhibitory effects on Ded1p condensate formation, even though we tested both charged and hydrophobic amino acids (**Fig. 7.5**), suggesting that the total concentration of free amino acids in a cell may have more of an effect on LLPS than the concentrations of individual amino acids. However, additional studies testing physiological amino acid concentrations and combinations of several amino acids are required to fully elucidate the effect of changing amino acid concentrations on biomolecular condensate formation.

Chapter 8

Summary and future directions

In this work, I've characterized the effects of K7 binding on DDX3X activity. K7 is a viral protein produced by vaccinia virus that binds to DDX3X's disordered N-terminal extension³⁶⁴. In Chapter 4, I demonstrated that K7 binding to DDX3X inhibits DDX3X RNA unwinding and ATPase activities by reducing DDX3X's functional RNA affinity *in vitro*. In Chapter 5, I showed that K7 binding disrupts DDX3X's ability to undergo LLPS *in vitro*, as well as DDX3X's ability to associate with stress granules in human cells. I also performed proof of principle experiments to demonstrate that K7 binding to DDX3X's N-terminus can inhibit the formation of pathogenic granules formed by disease-associated DDX3X mutants. In Chapter 6, I showed that K7 expression in HCT 116 cells reduces global translation by approximately 14% and does not impair cell growth. Finally, in Chapter 7, I identified additional small molecules (bis-ANS) that can modulate protein LLPS and biomolecular condensates. Here, I will discuss additional questions raised by this work and potential avenues to address them.

8.1 K7's therapeutic potential in DDX3X-associated diseases

As shown in Chapter 5, K7 binding to the SFFS motif in DDX3X's N-terminus inhibits the formation of pathogenic DDX3X-containing granules. This finding provides proof of concept that targeting DDX3X's IDRs is a potential strategy to treat diseases associated with the aberrant formation of DDX3X-containing granules. However, several questions still remain. Aberrant formation of stress granules following mutant DDX3X expression has been shown to

globally reduce translation of both DDX3X-dependent and DDX3X-independent transcripts, resulting in reduced translation of more transcripts than those affected by simple loss of DDX3X⁶⁰. This finding potentially explains how DDX3X missense mutants act in a dominant negative manner in the context of DDX3X syndrome²²⁴. Aberrant DDX3X granules contain rRNA and other RBPs, thus granule-inducing missense mutations may sequester wildtype DDX3X, RNAs, and other proteins in granules, leading to more severe phenotypes than those seen from the loss of DDX3X alone (nonsense mutations)²²⁴. Thus, disrupting the formation of these granules may prevent this sequestration of RNAs and proteins, reducing the effects of DDX3X missense mutations.

Based on our data, it remains unclear whether K7 expression can disrupt pre-formed DDX3X granules, as K7 was expressed either prior to applied stress or at the same time as mutant DDX3X. In order to test K7's ability to dissolve pre-formed DDX3X granules we could perform a combination of cellular and *in vitro* experiments. Developing a cell line with doxycycline-inducible K7 expression would enable temporal control of when K7 is expressed in cells. Thus, K7 expression could be induced after mutant DDX3X is present or exogenous stress is applied; however, doxycycline induction usually requires several hours for protein expression to be detectable. Additionally, it is currently unknown whether mutant DDX3X-containing granules are as dynamic as physiological stress granules. By the time K7 is adequately expressed following doxycycline induction, the mutant granules may have progressed to a more solid state that is not as easily dissolved. Performing fluorescence recovery after photobleaching

(FRAP) experiments on live cells expressing GFP-tagged wildtype or mutant DDX3X would provide a direct readout of how dynamic and reversible wildtype and mutant DDX3X granules are over time. These same experiments could also be performed following exposure to sodium arsenite, to determine if mutant DDX3X recruitment to physiological stress granules alters their dynamics.

Alternatively, K7's ability to dissolve pre-formed DDX3X protein condensates could be assessed *in vitro*. The disappearance of DDX3X condensates could be monitored via microscopy after the addition of K7 or protein storage buffer. In preliminary experiments I performed, addition of buffer alone significantly reduced the number of condensates present, making it difficult to determine any K7-specific effects on pre-formed DDX3X droplets. Thus, further optimization of the K7/buffer addition technique is required.

The yeast homolog Ded1p undergoes robust LLPS *in vitro*²¹⁷ and purifies much more easily than DDX3X. Therefore, Ded1p could be used to optimize the technical conditions for measuring K7-mediated dissolution of pre-formed DDX3X droplets. The SFFS motif in DDX3X's N-terminus is conserved in Ded1p (**Fig. 8.1**). Thus, K7 is able to bind Ded1p (**Fig. 8.2**) and inhibit its RNA unwinding activity (**Fig. 8.3**), similar to our results with DDX3X (Chapter 4). In preliminary experiments, K7 also reduced the average fluorescence intensity of Ded1p protein condensates *in vitro*, similar to observed effects on DDX3X protein condensates (**Fig. 8.4**). Thus, the effects of K7 binding are similar for DDX3X and Ded1p.

DDX3X 81- **KSSFFSDRGS** -90
 Ded1p 53- **GGSFFSNRR** -62

Figure 8.1. Sequence alignment between DDX3X and Ded1p N-terminus. Sequence conservation between the K7 binding motif (SFFS) in DDX3X's N-terminus (residues 81 to 90) and the N-terminus of the yeast homolog Ded1p.

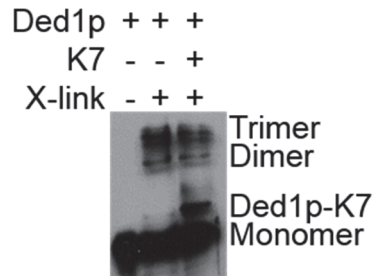


Figure 8.2. K7 binds Ded1p. 1 μM Ded1p was crosslinked with formaldehyde for 30 min with 2 μM RNA duplex (R16/41-3) and 0.5 mM ADPNP in the presence or absence of 2.8 μM K7. Proteins were resolved by SDS-PAGE and western blotting against Ded1p was performed.

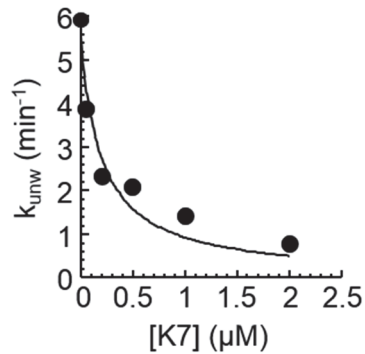


Figure 8.3. Impact of K7 on RNA unwinding by Ded1p. Pre-steady state RNA unwinding reactions with Ded1p were performed as in Figure 4.3. $[\text{Ded1p}] = 300 \text{ nM}$, $[\text{RNA}] = 0.5 \text{ nM}$, $[\text{ATP}] = 2 \text{ mM}$. Plot shows inhibition of Ded1p-mediated RNA duplex unwinding in the presence of K7 fit to a noncompetitive inhibition model. $K_i = 201 \pm 64 \text{ nM}$, $k_{\text{unw}}^{\text{max}} = 11.43 \pm 1.02 \text{ min}^{-1}$, $R^2 = 0.96$. $n = 1$ technical replicate.

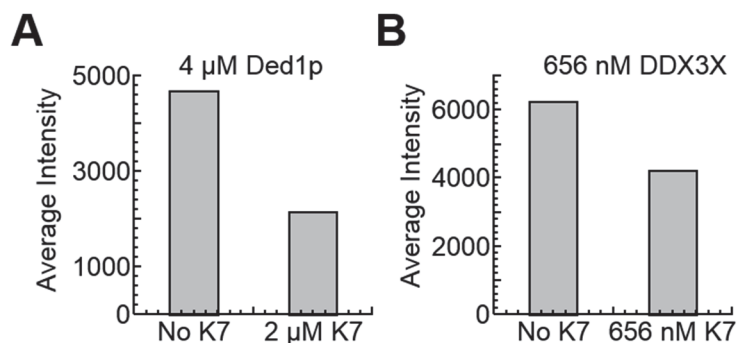


Figure 8.4. Impact of K7 on Ded1p condensate formation. (A) 4 μM Ded1p and 25 nM AF647-labelled Ded1p were incubated with or without 2 μM K7 for 1 hr at room temperature. 10 μL of each reaction was spotted on a microscope slide, covered with a coverslip, and imaged. 20 fluorescence images from each reaction were quantified using the nucleus counter tool in ImageJ. The average fluorescence intensity of droplets in each condition is shown. n = 1 technical replicate. (B) 656 nM DDX3X and 50 nM AF647-labelled DDX3X were incubated with or without 656 nM K7 for 1 hr at room temperature. 10 μL of each reaction was spotted on a microscope slide, covered with a coverslip, and imaged. 20 fluorescence images from each reaction were quantified using the nucleus counter tool in ImageJ. The average fluorescence intensity of droplets in each condition is shown. n = 1 technical replicate.

Given that Ded1p purifies more easily than DDX3X, Ded1p condensate formation can be studied with higher helicase concentrations (4 μM Ded1p maximum experimentally-obtainable concentration versus 2 μM DDX3X maximum experimentally-obtainable concentration). Turbidity measurements (OD₆₀₀) are more easily performed with the higher Ded1p concentrations. Therefore, optimization of K7/buffer addition could be easily performed using Ded1p coupled with the rapid readout of turbidity measurements. These optimized conditions could then be used to monitor K7-mediated dissolution of Ded1p and/or DDX3X condensates via microscopy.

Another open question is whether K7's inhibition of mutant DDX3X granules prevents the global translation inhibition associated with granule

formation⁶⁰. To answer this question, we could utilize the plasmids generated in Chapter 5 that co-express myc-tagged K7 or myc tag with wildtype/mutant DDX3X. We could perform puromycin labeling on these cells and measure the level of translation inhibition resulting from mutant DDX3X expression, as well as whether prevention of mutant granules by K7 co-expression restores global translation. Based on previous publications^{60,62}, formation of granules by DDX3X mutants should result in larger reductions in global translation than the reductions we observed following K7 expression (**Fig. 6.3**), since translation of both DDX3X-dependent and DDX3X-independent transcripts is negatively impacted by granule formation. This would be an exciting experiment that would test K7's ability to potentially disrupt some of the pleiotropic effects resulting from sequestration of cellular components in granules formed by disease-associated DDX3X mutants. K7 could then be used to directly test whether disruption of mutant granules and associated translation defects partially restores neurodevelopment and/or prevents tumorigenesis in mutant DDX3X models^{224,240,241}.

To use K7 as a potential therapeutic and/or to guide the development of DDX3X inhibitors that target the N-terminus, it would be helpful to identify the minimum portion of K7 required to bind and inhibit DDX3X. Structural studies demonstrated that the two phenylalanines in DDX3X's N-terminus interact with the hydrophobic cleft on K7's surface³⁶⁴. Additionally, K7's negative charge (pI = 4.8) further promotes interaction between K7 and DDX3X's positively charged N-terminus (pI = 7.8)³⁶⁴. D28 and D31 of K7 interact with R88 in DDX3X's N-

terminus near the two phenylalanines inserted into K7's hydrophobic cleft (81-KSSFFSDRGS-90)³⁶⁴. D31 of K7 also forms a hydrogen bond with S83 immediately preceding the two phenylalanines in DDX3X's N-terminus³⁶⁴. Mutation of D28 and D31 in K7 to alanines abolishes K7 binding to DDX3X³⁶³. Thus, a truncated K7 containing these residues could potentially be sufficient to inhibit DDX3X. Expression of various K7 truncations in human cells would allow determination of the minimal peptide required to inhibit mutant DDX3X granule formation. Purification of truncated K7 would allow testing of its ability to inhibit DDX3X helicase activity and condensate formation *in vitro*.

Finally, the generalizability of K7's effects to other DDX3X mutants beyond the DDX3X^{R534H} mutant studied in Chapter 5 is an additional consideration for K7's utility as a potential therapeutic. Preliminary studies indicate that K7 co-expression also inhibits the formation of granules by DDX3X^{G325E} and DDX3X^{G302V} (**Fig. 8.5**), two granule-inducing mutants identified in medulloblastoma⁶².

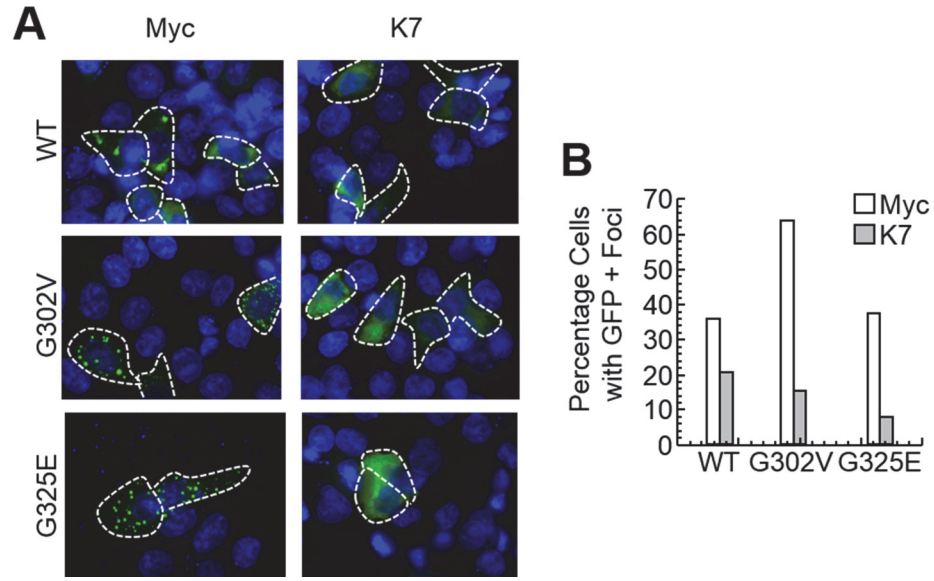


Figure 8.5. Impact of K7 on aberrant granules formed by DDX3X^{G302V} and DDX3X^{G325E}. HCT 116 cells were transfected with plasmids co-expressing GFP-tagged wildtype or mutant DDX3X with myc-tagged K7 or myc tag alone. 20 images from each condition were quantified using the Cell Counter tool in ImageJ. **(A)** Representative microscope images for each condition. **(B)** Percentage of cells with GFP-positive (DDX3X-positive) foci in each condition. n = 1 biological replicate

8.2 Viral benefits of preventing DDX3X association with stress granules

While our studies in Chapter 5 demonstrate that K7 prevents DDX3X's association with stress granules, it remains unclear the exact benefit this has during the viral life cycle. Vaccinia virus (VACV) encodes several proteins to prevent formation of antiviral granules (AVGs)⁴⁰⁶, as described in Chapter 5; however, since antiviral granules differ from canonical stress granules, it's unknown if DDX3X localizes to these structures. Performing immunofluorescence against DDX3X and other AVG-associated proteins (such as G3BP1⁴⁰⁶) in cells infected with VACV lacking the E3L (viral protein that prevents AVG formation⁴⁰⁶) and K7 proteins, would allow determination of DDX3X's localization to AVGs.

Comparison of DDX3X localization in this setting with DDX3X localization following infection with VACV lacking only E3L would determine whether K7 expression prevents DDX3X association with AVGs. Additionally, K7-specific effects on AVGs could be determined by quantifying AVG formation in the following settings: (i) VACV lacking E3L and K7 (robust AVG formation in the absence of E3L and no K7-mediated inhibition of DDX3X), (ii) VACV lacking E3L (robust AVG formation in the absence of E3L in the presence of usual K7 effects), (iii) VACV lacking K7 (effects of K7 only), and (iv) wildtype VACV (normal prevention of AVG formation).

As detailed in Chapter 3, DDX3X interacts with several immune signaling proteins (IKK ϵ , TBK1, TRAF3, and MAVS, **Fig. 3.4**) to promote induction of interferon production^{264,266-268}. K7 binding to DDX3X disrupts this promotion of interferon induction²⁶⁵. Interestingly, mutation of the two phenylalanines required for DDX3X to bind K7 also disrupts DDX3X's ability to promote interferon induction in the absence of K7³⁶⁴, suggesting that the two phenylalanines targeted by K7 may be required for DDX3X binding to one or several immune signaling proteins. Interactions between DDX3X and TRAF3 occur via residues 139-172 in DDX3X's N-terminus, approximately 60 residues away from the K7 binding site^{268,364}. IKK ϵ also interacts with DDX3X's N-terminus, though the exact residues responsible are unknown²⁶⁵. The interaction sites for MAVS and TBK1 are unknown^{264,268}. Using pull-downs to test the ability of DDX3X^{FFAA} to bind TRAF3, IKK ϵ , MAVS, and TBK1 would determine whether the two phenylalanines bound by K7 are required for DDX3X binding to immune signaling

proteins. If these phenylalanines are required, K7 may compete with these signaling proteins for DDX3X binding, thereby reducing DDX3X-mediated promotion of interferon signaling.

It has been suggested that DDX3X may serve as a scaffold for the formation of immune signaling complexes²⁶⁸, explaining DDX3X's binding to proteins involved in several sequential steps of the immune signaling cascade (**Fig. 3.4**). Many immune signaling proteins are also known to localize to stress granules²⁰⁷. This raises the question as to whether DDX3X acts as a scaffold by facilitating recruitment of immune signaling proteins to stress granules, where their close proximity to each other may increase immune signaling. If DDX3X does serve as a scaffold and recruitment of immune signaling proteins to stress granules promotes the immune response, then viral disruption of DDX3X association with stress granules could potentially reduce immune signaling. TRAF3 and TBK1 both localize to stress granules induced by oxidative stress, G3BP1 overexpression, and infection with infectious bronchitis virus (IBV)^{407,408}. MAVS and IKK ϵ also localize to stress granules formed in IBV-infected cells⁴⁰⁸. These studies primarily categorized stress granules by the presence of G3BP1 foci^{407,408}, and did not characterize the RNA content of the granules or the ability of cycloheximide-mediated polysome stabilization to disrupt them. The timing of granule association for each of these proteins following applied stress or infection was also not characterized.

The assembly and disassembly of stress granules (and the analogous antiviral granules described in Chapter 5) involves a complex network of dynamic

protein-RNA interactions^{150,369,372,373}. Careful time-resolved studies to visualize the association and dissociation of numerous proteins and RNAs within these granules following infection are required to fully understand this complex interaction network. It remains unclear whether DDX3X association with stress granules is required for DDX3X's promotion of type I interferon signaling; however, given the existing evidence, it seems likely that recruitment of DDX3X and other proteins involved in type I interferon signaling to stress granules promotes interferon induction by concentrating these signaling complexes together. Thus, VACV disruption of DDX3X association with stress granules may underlie K7's ability to disrupt DDX3X-mediated promotion of antiviral innate immune signaling.

Finally, DDX3X association with stress granules prevents DDX3X interaction with the NLRP3 inflammasome, leading to reduced inflammasome activation and reduced cell death in response to stress/infection²²¹. Interestingly, the NLRP3 inflammasome is activated by bacterial, viral, and fungal infections⁴⁰⁹. Could K7 binding to DDX3X also prevent DDX3X association with the inflammasome and the subsequent death of VACV infected cells? DDX3X associates with the inflammasome primarily through its structured helicase core²²¹. Immunofluorescence experiments in macrophages (cells with high levels of the inflammasome) following K7 expression and inflammasome activation (commonly achieved via LPS treatment) would detect K7-mediated changes in DDX3X association with the inflammasome. If K7 prevents DDX3X association with the inflammasome (in addition to inhibiting DDX3X association with stress

granules), K7 binding could block both DDX3X-mediated cell death and the downstream effects of DDX3X association with stress granules.

Formation of stress granules is known to reduce apoptosis⁴¹⁰; however, preliminary studies I conducted failed to detect a change in cell death upon exposure to sodium arsenite in the presence of K7 (**Fig. 8.6**). These results are not conclusive, as I utilized propidium iodide staining to detect cell death following transient transfection, and propidium iodide is less sensitive to apoptosis than it is to non-apoptotic cell death⁴¹¹. Additionally, these experiments were performed without co-expression of GFP, so the quantification included both K7-expressing and K7 non-expressing cells. Alternative approaches to identify whether K7-mediated disruption of stress granules leads to increased apoptosis would be to stain cells with specific markers of apoptotic cell death, such as annexin V⁴¹¹, following sodium arsenite treatment. Alternatively, I could perform CellTiter-Glo experiments as in Chapter 6 (**Fig. 6.4**) in K7-expressing cells following treatment with sodium arsenite. This would allow detection of reduced cell metabolism (correlating with reduced cell viability) in K7-expressing cells where stress granule formation is inhibited.

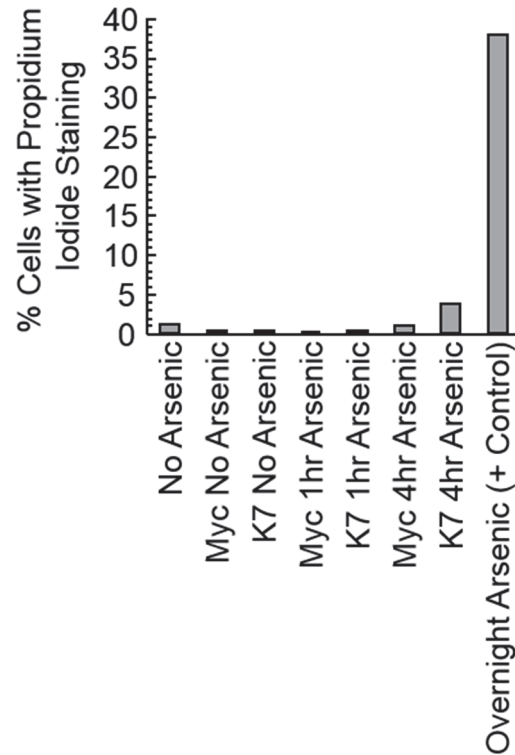


Figure 8.6. Preliminary test of whether K7 expression alters cell survival during stress. HCT 116 cells were transfected with plasmids expressing myc-tagged K7 or myc tag alone then treated with 1 mM sodium arsenite (arsenic) for the indicated times. Cells were then incubated with 1 μ g/mL propidium iodide for 15 min and imaged. 5 images from each condition were quantified for the percentage of cells stained with propidium iodide (dead cells). n = 1 biological replicate.

Ultimately, additional microscopy experiments utilizing a variety of conditions detailed here will further identify the downstream effects of K7-mediated inhibition of DDX3X association with stress granules. These approaches can also be used to dissect the overlapping contributions of DDX3X localization to stress granules and binding to immune signaling complexes during the induction of interferon production.

8.3 Effect of K7 on DDX3X-dependent translation

In Chapter 6, I demonstrated that K7 expression reduced global translation by approximately 14% in HCT 116 cells (**Fig. 6.3**); however, it remains unclear whether these effects are mediated by inhibition of DDX3X or not. DDX3X promotes translation of a subset of structured transcripts in a variety of human cells^{60,223,256,257}, with several of these transcripts encoding pro-inflammatory and immune-associated proteins²⁵⁷. To test K7's effects on translation of these DDX3X-dependent transcripts, a stable K7-expressing cell line would be helpful. This cell line would allow measurement of K7-mediated effects on translation using polysome profiling and RT-qPCR without the added noise from non-expressing background cells present following transient transfection (see Chapter 6). RT-qPCR to identify changes in the association of DDX3X-dependent transcripts with polysomes following K7 expression would then provide clear measurement of how K7-mediated inhibition of DDX3X impacts DDX3X-dependent translation. These stable cell lines would also be ideal for conclusively identifying any K7-mediated changes in DDX3X association with the active translation machinery following K7 binding (compared to the results in **Fig. 6.2** following transient transfection of K7 and measurement of the bulk population including $\geq 50\%$ cells that did not express K7).

8.4 Effects of other viral proteins that bind DDX3X

In addition to K7 protein produced by VACV, several other viral proteins directly bind to DDX3X. Hepatitis C virus core protein binds DDX3X's C-terminal intrinsically disordered extension and disrupts interactions between DDX3X and

the immune signaling protein MAVS³⁴². DDX3X is also redistributed from stress granules to viral replication centers (lipid droplets) during hepatitis C virus infection, and this redistribution may be mediated in part by binding of the core protein³³⁸⁻³⁴². Influenza A virus NS1 and NP proteins both interact with DDX3X's disordered termini³⁴⁸. Interactions with NS1 are suggested to disrupt DDX3X-mediated formation of stress granules; however, these findings are complicated by NS1's inhibitory effects on the upstream phosphorylation of eIF2 α , which disrupts stress granule formation independent of DDX3X³⁴⁸. Dengue virus capsid protein interacts with DDX3X's conserved helicase core to disrupt innate immune signaling^{346,347}.

All three of these established protein-protein interactions between viral proteins and DDX3X have been demonstrated to interfere with the innate immune response; however, the extent of their effects on other DDX3X functions are unclear. For both influenza A virus and hepatitis C virus some evidence suggests that viral protein binding modulates DDX3X's ability to associate with stress granules^{338-342,348,349}, suggesting some similarity to the effects of vaccinia virus K7 protein. However, the effects of these viral proteins on DDX3X association with stress granules when the viral protein is expressed in the absence of other viral proteins have not been examined. Similar experiments to the ones I performed in Chapter 5, where each viral protein is transiently transfected into human cells prior to the induction of stress, would provide further insight into the effects of these viral proteins on DDX3X association with stress granules.

Given that many of these viral proteins bind to DDX3X's C-terminal extension or helicase core, they may have different effects than K7 (binds to the N-terminal extension³⁶⁴) on DDX3X helicase activity and translation. Puromycin labeling could be used to measure the effects of these viral proteins on translation following their transient transfection in human cells, as I did with K7 in Chapter 6. Purification of these viral proteins would enable measurement of their effect on DDX3X *in vitro* helicase activity; however, these experiments would not be straightforward. Dengue capsid protein, hepatitis C virus core protein, and influenza A NS1 and NP proteins all bind RNA⁴¹²⁻⁴¹⁵. This RNA binding activity would complicate the kinetic analysis of their effects on DDX3X, as the inhibitory effects of their competition for RNA binding would need to be accounted for. Additionally, hepatitis C virus core protein and dengue capsid protein have membrane-interacting domains, which decrease the ease with which they can be purified^{412,413}. We attempted to purify hepatitis C virus core protein from *E. coli* under denaturing conditions with limited success; thus, we were unable to measure its effects on DDX3X RNA helicase activity *in vitro*.

Identifying the shared and divergent effects of other viral proteins on DDX3X activity would further inform efforts to develop anti-viral therapeutics that target the host protein DDX3X. While *in vitro* kinetic analysis of these effects will be more difficult than for the K7 protein, cellular experiments using transient transfections should be straightforward. In this way, the effects of other viral proteins on translation and DDX3X association with stress granules can be

measured, providing insight into potential shared mechanisms of viruses that target DDX3X.

8.5 Effect of post-translational modifications

DDX3X is extensively modified post-translationally, with over 90 identified modifications, 12 of which have been verified using low throughput methods (**Fig. 8.7**)⁴¹⁶. Many of these modifications occur within the N-terminal disordered extension, and thereby are likely to regulate DDX3X LLPS. This relationship has already been demonstrated for acetylation of several lysines within DDX3X's N-terminus⁴¹⁷. DDX3X acetylation disrupts DDX3X LLPS *in vitro*, and deacetylation of DDX3X by HDAC6 is required for stress granule maturation in mammalian cells⁴¹⁷.

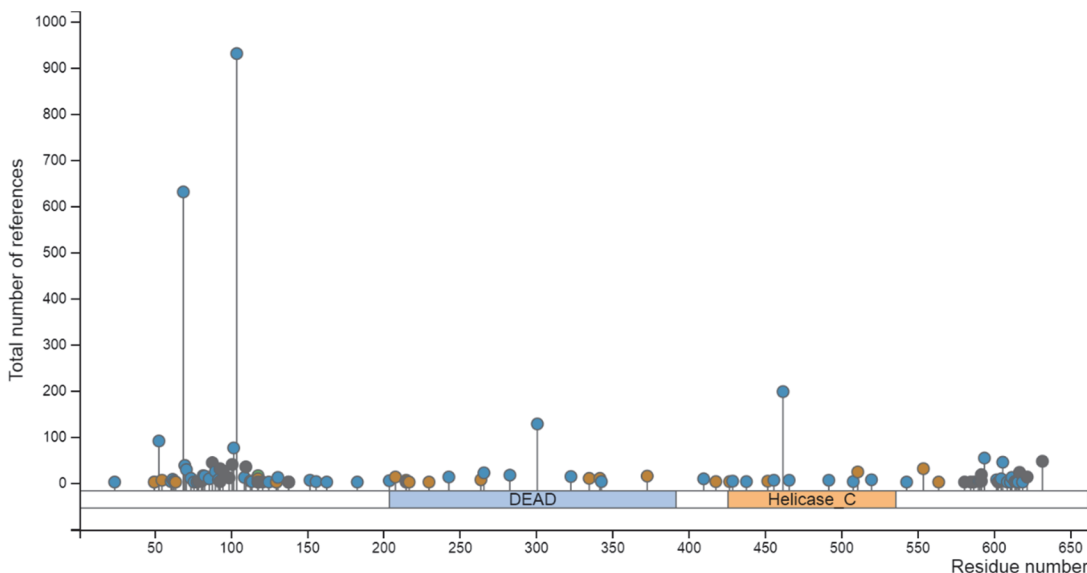


Figure 8.7. Map of identified post-translational modifications on DDX3X. Blue circles = phosphorylation, green circles = acetylation, orange circles = ubiquitylation, purple circles = other. Plot generated by PhosphoSitePlus (www.phosphosite.org)⁴¹⁶.

Several post-translational modifications occur within the K7 binding motif in DDX3X's N-terminus (81-KSSFFSDRGS-90): ubiquitylation and methylation of

K81; phosphorylation of S82, S83, S86, and S90; and methylation of R88⁴¹⁶. As noted in section 8.1, D28 and D31 in K7 are required for K7 binding to DDX3X, and these two residues interact with S83 and R88 in DDX3X's N-terminus³⁶⁴. The post-translational modifications identified on these residues may therefore alter K7 binding to DDX3X.

Additionally, phosphorylation of S82, S83, and S86 in DDX3X's N-terminus were confirmed in a low throughput study²⁶⁶. Phosphorylation of these serine residues is carried out by IKK ϵ upon DDX3X binding²⁶⁶. IKK ϵ also phosphorylates S102 of DDX3X²⁶⁶. Phosphorylation of S82, S83, and S86 did not impact interferon induction; however, phosphorylation of S102 was required for IRF3 binding to IKK ϵ /DDX3X and the subsequent induction of interferons²⁶⁶. Phosphodeficient (S82A, S83A, S86A) and phosphomimetic (S82D, S83D, S86D) mutants of DDX3X can be used to further investigate the role phosphorylation of these residues plays in DDX3X binding to other immune signaling proteins (TRAF3, MAVS, etc.), as well as DDX3X's ability to undergo LLPS and associate with stress granules.

8.6 Determining the exact mechanism behind K7-mediated inhibition of DDX3X

As demonstrated in Chapter 4, K7 inhibits DDX3X RNA helicase activity *in vitro* by reducing DDX3X's functional RNA affinity. This reduced functional RNA affinity could be the result of several mechanisms: reduced formation of the active DDX3X oligomer, reduced binding of RNA by DDX3X, or reduced ability to perform the strand separation step. As discussed in Chapter 4, given the known

role of DDX3X's disordered termini in promoting oligomerization, it is likely that K7 reduces DDX3X oligomerization. This idea is further supported by the finding that K7 inhibits formation of DDX3X protein condensates in the absence of RNA and ATP, as shown in Chapter 5 (**Fig. 5.1**). However, formaldehyde crosslinking of DDX3X did not show a clear decrease in oligomer formation following binding to K7 (**Fig. 4.7**). Thus, reduced RNA binding and/or impaired strand separation upon K7 binding are still possible.

Given the semi-quantitative nature of formaldehyde crosslinking, changes in DDX3X oligomerization in the presence of K7 could alternatively be detected via sucrose gradient centrifugation or gel filtration of purified proteins to separate monomeric from oligomeric forms of DDX3X. Changes in RNA binding in the presence of K7 can be measured by using UV crosslinking to irreversibly bind DDX3X to radiolabeled RNA. Subsequent polyacrylamide gel electrophoresis would allow separation of bound from unbound RNA and the quantification of any reduced RNA binding in the presence of K7. Finally, the strand separation step of DDX3X can be directly measured by performing single cycle pre-steady state unwinding reactions, as previously described³⁸. Performing these reactions in the absence and presence of K7 would allow determination of K7's effects on the strand separation step.

8.7 DDX3X oligomerization as a precursor to liquid-liquid phase separation

As discussed above, our studies indicate that K7 likely disrupts both DDX3X oligomerization and DDX3X LLPS, suggesting that the same protein-protein interactions involved in DDX3X oligomerization are also involved in

mediating DDX3X LLPS. Dynamic protein oligomerization has been suggested as a precursor/route to LLPS, though the exact molecular progression from monomer to protein condensate remains unclear¹⁵⁰. Another emerging idea in the field is that increased ATPase activity of RNA helicases (such as DDX3X) leads to dissolution of phase-separated protein condensates and biomolecular condensates²¹⁰. This relationship is best defined for stimulation of Dhh1p ATPase activity upon binding of its cofactor Not1p²¹⁰. This interaction leads to dissolution of Dhh1p protein condensates *in vitro* and P-bodies in yeast²¹⁰. Not1p is an MIF4G-containing helicase cofactor similar to eIF4G, a cofactor of Ded1p²¹⁰. eIF4G also dissolves Ded1p condensates *in vitro*, and this finding was used to suggest the generalizability of ATPase stimulation leading to condensate dissolution²¹⁰, even though eIF4G does not significantly increase Ded1p ATPase activity *in vitro*¹¹⁶.

Our findings that K7 inhibits both DDX3X ATPase activity and LLPS is contradictory to the above idea. However, disruption of LLPS via disrupting helicase oligomerization is potentially a more consistent explanation of *in vitro* findings. While eIF4G does not stimulate Ded1p ATPase activity *in vitro*, it does prevent Ded1p oligomerization^{28,116}. Similarly, while it's unknown whether the yeast Dhh1p functions as an oligomer, the *Xenopus* homolog Xp54 has been suggested to form oligomers⁴¹⁸. Studies investigating the oligomeric status of Dhh1p and Not1p's effects on this oligomerization would provide additional insight into the role of oligomerization in mediating helicase LLPS. Likely, it is a combination of both RNA remodeling activity (coupled with ATP hydrolysis) and

protein oligomerization that contribute to the ability of RNA helicases to regulate biomolecular condensates.

Chapter 9

Materials and Methods

9.1 Protein purification

9.1.1 DDX3X

DDX3X was expressed from pET-SUMO plasmid (generated by Kaba Tandjigora) in BL21 (DE3) *E. coli* induced with 0.5 mM isopropyl β -D-1-thiogalactopyranoside for 4 hr at 37 °C (induce expression at OD₆₀₀ ~0.6). Bacteria were lysed on ice by sonication in 1X lysis buffer (1X buffer Y(50 mM NaH₂PO₄ pH 6.0, 300 mM NaCl, 30% glycerol) + 0.5% IGEPAL CA-630, 5 mM imidazole, 1 mM PMSF, and EDTA-free protease inhibitor (Roche, 04693159001)) then clarified by centrifugation at 15,000 rpm for 45 min at 4 °C. Lysates were bound to Ni-NTA-agarose overnight in the presence of 25 μ g/mL RNase A at 4 °C, then washed with 4-5 column volumes wash buffer 1 (1X buffer Y + 1M NaCl, 5 mM imidazole, 1% IGEPAL CA-630, 0.4 mM PMSF), wash buffer 2 (1X buffer Y + 30 mM imidazole, 1% IGEPAL CA-630, 0.4 mM PMSF), and wash buffer 3 (1X buffer Y + 60 mM imidazole, 1% IGEPAL CA-630, 0.4 mM PMSF). DDX3X was then eluted with 1X buffer Y + 350 mM imidazole, 1% IGEPAL CA-630, 0.4 mM PMSF. DDX3X-containing fractions were pooled and diluted three-fold with 1X buffer Z (100 mM Tris-Cl pH 8.0, 1 mM EDTA, 50% glycerol, 0.1% Triton X-100, 2 mM DTT) and incubated with SUMO protease overnight at 4 °C to remove the His-SUMO tag. Cleaved protein was then bound to either phosphocellulose resin or a GE HiTrap 1 mL heparin column and washed with 10 column volumes of wash buffer 1 (1X buffer Z + 50 mM NaCl)

and wash buffer 2 (1X buffer Z + 100 mM NaCl) to remove excess SUMO protease. DDX3X was then eluted with 1X buffer Z + 200 mM NaCl (phosphocellulose elution) or 1X buffer Z + 300 mM NaCl (GE HiTrap heparin elution). Purified protein was pooled, concentrated using a 10 kDa centrifugal filter unit (Millipore, UFC8010), flash frozen, and stored at -80 °C.

9.1.2 Truncated DDX3X (Δ DDX3X)

E. coli expression plasmid encoding codon-optimized His₆-MBP (maltose-binding protein)-DDX3X₁₃₂₋₆₀₇ was a gift from Dr. Jennifer Doudna. Δ DDX3X purification was performed by Kaba Tandjigora, with slight modifications from the published protocol²³⁰. His₆-MBP-DDX3X₁₃₂₋₆₀₇ was expressed in BL21 Star *E. coli* induced with 1 mM isopropyl β -D-1-thiogalactopyranoside overnight at 18 °C. Bacteria were lysed on ice by sonication in lysis buffer (500 mM NaCl, 0.5% IGEPAL CA-630, 10 mM imidazole, 20 mM HEPES pH 7.5, 0.05% β -mercaptoethanol), then clarified by centrifugation at 15,000 rpm for 45 min at 4 °C. Lysates were bound to Ni-NTA-agarose for 1 hr at 4 °C, then washed using 4-5 column volume washes with low salt wash buffer (500 mM NaCl, 20 mM imidazole, 20 mM HEPES pH 7.5, 0.05% β -mercaptoethanol) and high salt wash buffer (1 M NaCl, 20 mM imidazole, 20 mM HEPES pH 7.5, 0.05% β -mercaptoethanol). Δ DDX3X was then eluted with buffer containing 500 mM NaCl, 250 mM imidazole, 100 mM Na₂SO₄, 9.5 mM NaH₂PO₄, 40.5 mM Na₂HPO₄, 0.05% β -mercaptoethanol. Δ DDX3X-containing fractions were dialyzed overnight at 4 °C with TEV protease to remove the His₆-MBP tag in buffer containing 200 mM NaCl, 20 mM HEPES pH 7, 40% glycerol, 0.25 mM

DTT. Cleaved protein was then diluted four-fold with no salt heparin buffer (20 mM HEPES pH 7, 40% glycerol, 0.25 mM DTT) and bound to GE HiTrap 1mL heparin column. Column was then washed with 10 column volumes high salt heparin buffer (200 mM NaCl, 20 mM HEPES pH 7, 40% glycerol, 0.25 mM DTT), then eluted with buffer containing 400 mM NaCl, 20 mM HEPES pH 7, 40% glycerol, 0.25 mM DTT. Purified protein was pooled, flash frozen, and stored at -80 °C.

9.1.3 Ded1p

Ded1p was purified by Dr. Andrea Putnam as previously described²¹⁹. pET22b+6x-His-Ded1p was expressed in BL21 (DE3) *E. coli* induced overnight with 0.5 mM isopropyl β -D-1-thiogalactopyranoside at 28 °C (induce expression at OD₆₀₀ ~0.5). Bacteria were lysed by sonication in 1X lysis buffer (1X buffer Y (50 mM NaH₂PO₄ pH 6.0, 300 mM NaCl, 50% glycerol) + 1% IGEPAL CA-630, 5 mM imidazole, 0.4 mM PMSF, protease inhibitor tablet (Roche, 04693159001)) and purified on Ni-NTA-agarose using 4-5 column volumes wash buffer 1 (1X Y + 1 M NaCl, 5 mM imidazole, 1% IGEPAL CA-630, 0.4 mM PMSF), wash buffer 2 (1X Y + 1% IGEPAL CA-630, 30 mM imidazole, 0.4 mM PMSF), and wash buffer 3 (1X Y + 1% IGEPAL CA-630, 60 mM imidazole, 0.5 mM PMSF). Ded1p was eluted with 1X Y + 250 mM imidazole, 1% IGEPAL CA-630, 0.4 mM PMSF. Ded1p containing fractions were pooled and diluted 6-fold in 1X Buffer Z (50 mM Tris pH 8, 1 mM EDTA, 50% glycerol, 0.1% Triton X-100, 2 mM DTT) and bound to phosphocellulose resin. Phosphocellulose was washed with 4-5 column volumes of 1X Z + 100 mM NaCl and 1X Z + 200 mM NaCl then eluted with 1X

Z + 300 mM NaCl. Purified protein was pooled, flash frozen, and stored at -80 °C.

9.1.4 His-K7

pET15b-His₆-K7 was a gift from Dr. Amir R Khan³⁶⁴. His₆-K7 was expressed in BL21 (DE3) *E. coli* induced with 0.5 mM isopropyl β-D-1-thiogalactopyranoside overnight at 16 °C (induce expression at OD₆₀₀ ~0.6). Bacteria were lysed on ice by sonication in 1X lysis buffer (1X buffer Y(50 mM NaH₂PO₄ pH 6.0, 300 mM NaCl, 30% glycerol) + 0.5% IGEPAL CA-630, 15 mM imidazole, 1 mM PMSF, and protease inhibitor tablet (Roche, 04693159001)), then clarified by centrifugation at 15,000 rpm for 45 min at 4 °C. Lysates were bound to Ni-NTA-agarose overnight in the presence of 25 µg/mL RNase A at 4 °C, then washed with 4-5 column volumes wash buffer 1 (1X buffer Y + 1M NaCl, 5 mM imidazole, 1% IGEPAL CA-630, 0.4 mM PMSF), wash buffer 2 (1X buffer Y + 30 mM imidazole, 1% IGEPAL CA-630, 0.4 mM PMSF), and wash buffer 3 (1X buffer Y + 60 mM imidazole, 1% IGEPAL CA-630, 0.4 mM PMSF). His₆-K7 was then eluted with 1X buffer Y + 250 mM imidazole, 1% IGEPAL CA-630, 0.4 mM PMSF. His₆-K7-containing fractions were pooled and diluted 6-fold in 1X buffer Z (100 mM Tris-Cl pH 8.0, 1 mM EDTA, 30% glycerol, 0.1% Triton X-100, 2 mM DTT), then loaded onto a 1 mL Mono Q anion exchange column. Column was washed with 20 column volumes 1X buffer Z + 50 mM NaCl, then eluted with 1X buffer Z + 100 mM NaCl. Purified protein was pooled, flash frozen, and stored at -80 °C.

9.1.5 Tau (adapted from³⁹⁶)

Tau purification was performed by Dr. Witold Surewicz's laboratory as previously described³⁹⁶. Tau was expressed from pET-15b in BL21 (DE3) *E. coli* induced with 1 mM isopropyl 1-thio- β -d-galactopyranoside for 3 hr at 37 °C. Bacteria were lysed on ice by sonication in lysis buffer (20 mM MES, 500 mM NaCl, 1 mM EDTA, 0.2 mM MgCl₂, 5 mM DTT, 1 mM PMSF, protease inhibitor mixture, pH 6.8). Lysates were boiled for 20 minutes, cooled on ice, then clarified by centrifugation at 127,000g for 40 min. The protein was then loaded onto GE Healthcare SP Sepharose HP cation-exchange column and eluted using a linear gradient of NaCl. Tau-containing fractions were pooled, concentrated, and loaded onto a Superdex 75 10/300 GL size-exclusion column. Proteins were eluted with 10 mM HEPES buffer, pH 7.4, containing 100 mM NaCl, 2 mM DTT, 0.1 mM PMSF. Purified protein was pooled, flash frozen, and stored at -80 °C.

9.1.6 FUS low complexity domain (adapted from³⁹⁶)

Purification of the FUS low complexity domain was performed by Dr. Witold Surewicz's laboratory as previously described³⁹⁶. Codon-optimized His-tagged FUS low complexity domain (His-FUS₁₋₁₆₅) was expressed from pRSET-b in Rosetta (DE3) pLysS *E. coli* induced with 1 mM isopropyl 1-thio- β -d-galactopyranoside overnight. Bacterial pellets were resuspended in 50 mM Tris pH 8.0 buffer containing 6 M guanidine-HCl, 250 mM NaCl, 50 mM imidazole, and 5 mM β -mercaptoethanol. Lysate was bound to Ni-NTA resin and washed with 4-5 column volumes of lysis buffer. Protein was then eluted using a linear gradient of 700 mM imidazole. His-FUS₁₋₁₆₅-containing fractions were pooled and

dialyzed overnight in 20 mM CAPS pH 11.0 buffer. Stocks were concentrated, flash frozen, and stored at -80 °C.

9.1.7 SUMO protease

SUMO protease bacterial expression vector pHYRS52 was a gift from Dr. Hideo Iwai (Addgene plasmid # 31122 ; <http://n2t.net/addgene:31122> ; RRID:Addgene_31122). SUMO protease was expressed in BL21 (DE3) *E. coli* induced with 0.5 mM isopropyl 1-thio- β -D-galactopyranoside overnight at 20 °C (induce expression at OD₆₀₀ ~0.6). Bacteria were lysed on ice by sonication in 1X lysis buffer (1X buffer Y(50 mM NaH₂PO₄ pH 6.0, 300 mM NaCl, 30% glycerol) + 0.5% IGEPAL CA-630, 5 mM imidazole, 1 mM PMSF, and protease inhibitor tablet (Roche, 04693159001)), then clarified by centrifugation at 15,000 rpm for 45 min at 4 °C. Lysates were bound to Ni-NTA-agarose overnight in the presence of 25 μ g/mL RNase A at 4 °C, then washed with 4-5 column volumes wash buffer 1 (1X buffer Y + 1M NaCl, 5 mM imidazole, 1% IGEPAL CA-630, 0.4 mM PMSF), wash buffer 2 (1X buffer Y + 30 mM imidazole, 1% IGEPAL CA-630, 0.4 mM PMSF), and wash buffer 3 (1X buffer Y + 60 mM imidazole, 1% IGEPAL CA-630, 0.4 mM PMSF). SUMO protease-containing fractions were pooled and diluted 5-fold in 1X buffer Z (100 mM Tris-Cl pH 8.0, 1 mM EDTA, 30% glycerol, 0.1% Triton X-100, 2 mM DTT), then loaded onto a NAP-25 column for buffer exchange into 1X buffer Z + 100 mM NaCl. Purified protein was pooled, flash frozen, and stored at -80 °C.

9.1.8 Determination of recombinant protein concentration

Recombinant protein concentrations were determined by densitometry (aliquots of purified protein were run on SDS-PAGE with a BSA standard curve).

9.2 RNA unwinding assays

9.2.1 Formation of radiolabeled RNA duplex

RNA oligonucleotides were purchased from DHARMACON.

R16: 3'-CGCAGAAAUGCCACGA-5'

R41: 5'-GCGUCUUUACGGUGCUUAAAACAAAACAAAACAAAACAAA-3'

Radiolabeling and RNA duplex formation was performed as previously described³⁷. R16 was radiolabeled with [γ -³²P] ATP by T4 PNK labeling for 60 min at 37 °C. T4 PNK was inactivated by addition of denaturing gel loading buffer (16% formamide, 0.02% bromophenol blue, 0.02% xylene cyanol) and boiling at 95 °C for 2 min. Sample was then run on a 20% denaturing gel, and band corresponding to radiolabeled R16 was cut out. Radiolabeled R16 was eluted into 600 μ L elution buffer (300 mM sodium acetate, 1 mM EDTA, 0.5% SDS) overnight at 4 °C. Radiolabeled R16 was ethanol precipitated from the elution buffer, and the dried RNA pellet was resuspended in 10 μ L water.

16 bp RNA duplex with 25 nt 3'-ssRNA tail (R16/41-3) was formed by combining radiolabeled R16 with 2 μ L 100 μ M R41 in duplex annealing buffer (100 mM MOPS pH 6.5, 10 mM EDTA, 0.5 M KCl). The mixture was heated to 95 °C then slowly cooled to room temperature. Once at room temperature, sample was added to native gel loading dye (10% glycerol, 0.05% bromophenol blue, 0.05% xylene cyanol) and run on 15% non-denaturing PAGE. The band

corresponding to R16/41-3 duplex was cut out and eluted in 600 μ L elution buffer overnight at 4 °C. R16/41-3 was ethanol precipitated from the elution buffer, and the dried RNA pellet was resuspended in 10 μ L duplex buffer (10 mM MOPS pH 7.0, 50 mM KCl, 0.1 mM MgCl₂). Radiolabeled duplex concentration was determined via scintillation counting. The calculated current specific activity was used to convert from the measured dpms to moles. All necessary calculations are described on PerkinElmer's ($[\gamma\text{-}^{32}\text{P}]$ ATP supplier) radiochemical calculations webpage (<https://www.perkinelmer.com/lab-products-and-services/application-support-knowledgebase/radiometric/radiochemical-calculations.html>).

9.2.2 Pre-steady state RNA unwinding assays

Pre-steady state RNA unwinding assays were performed and quantified as previously described³⁷. Pre-steady state unwinding reaction mixtures (30 μ L) containing 40 mM Tris-HCl pH 8.0, 50 mM NaCl, 0.5 mM MgCl₂, 2 mM DTT, 1 unit/mL RNasin, 0.01% (v/v) IGEPAL CA-630, 8% glycerol, and 0.5 nM radiolabeled substrate were incubated for 15 min at 19 °C with the indicated concentrations of Ded1p, DDX3X, Δ DDX3X, and/or His-K7. Stock ATP/MgCl₂ solutions were also pre-incubated for 15 min at 19 °C. Reactions were performed in a temperature-controlled aluminum heat block at 19 °C. One 3 μ L aliquot (time = 0 min) was removed and mixed with stop buffer (0.1% (w/v) SDS, 50 mM EDTA, 0.01% (w/v) xylene cyanol, 0.01% (w/v) bromophenol blue, 20% glycerol) immediately prior to initiation of the reaction by addition of equimolar ATP/MgCl₂ (2 mM final concentration, unless otherwise stated). At subsequent time points, 3 μ L aliquots were removed, mixed with stop buffer, and stored on ice. Duplex and

single-stranded RNA were separated on 15% non-denaturing PAGE at room temperature at 20V/cm. Gels were dried, and the separated RNAs were visualized with a PhosphorImager. Band intensities were quantified using ImageQuant TL software (GE) and the fraction single-stranded RNA was determined:

$$\text{Fraction ssRNA} = \frac{\text{ssRNA intensity}}{\text{ssRNA intensity} + \text{dsRNA intensity}} \quad (\text{Eq.1})$$

Unwinding time courses were fit to a first order rate equation using Kaleidagraph software:

$$\text{Frac ssRNA} = k'_{unw} * (k'_{unw} + k'_{ann})^{-1} * (1 - e^{-(k'_{unw} + k'_{ann}) * t}) \quad (\text{Eq.2})$$

Frac ssRNA is the fraction of unwound RNA at a given time point, k'_{unw} is the unwinding rate constant, k'_{ann} is the annealing rate constant, and t is time.

9.2.3 Equation fitting

Equation fitting was performed using Kaleidagraph software. Functional RNA and ATP affinities ($K_{1/2}^{\text{RNA}}$, $K_{1/2}^{\text{ATP}}$) were determined by fitting helicase and ATP titrations to the Hill equation:

$$k'_{unw} = \frac{k_{unw}^{\text{max}} * [S]^H}{[S]^H + \left(\frac{K_1}{2}\right)^H} \quad (\text{Eq.3})$$

k'_{unw} is the RNA unwinding rate constant, k_{unw}^{max} is the maximum RNA unwinding rate constant, $[S]$ is the concentration of helicase or ATP, H is the Hill coefficient, and $K_{1/2}$ is the functional binding constant.

Inhibition constants (K_i) for K7 binding were determined by fitting K7 titrations to a model for non-competitive inhibition:

$$k'_{unw} = \frac{((k_{unw}^{max})/(1+(\frac{[I]}{K_i})*[S]))}{[S]+K_{1/2}} \quad (\text{Eq.4})$$

k'_{unw} is the RNA unwinding rate constant, k_{unw}^{max} is the maximum RNA unwinding rate constant, $[I]$ is the inhibitor concentration, K_i is the inhibition constant, $[S]$ is the substrate concentration, and $K_{1/2}$ is the functional binding affinity for S.

9.3 ATP hydrolysis assays

ATP hydrolysis assays were performed as previously described¹⁰³. Steady-state ATP hydrolysis reaction mixtures (20 μ L) containing 40 mM Tris-HCl pH 8.0, 50 mM NaCl, 0.5 mM MgCl₂, 2 mM DTT, 1 unit/mL RNasin, 0.01% (v/v) IGEPAL CA-630, 8% glycerol, and 2 μ M non-radiolabeled R16/41-3 duplex were incubated for 15 min at 19 °C with the indicated concentrations of DDX3X, Δ DDX3X, and/or His-K7. Stock ATP/MgCl₂ solutions containing trace [γ -³²P] ATP were also pre-incubated for 15 min at 19 °C. Reactions were performed in a temperature-controlled aluminum heat block at 19 °C. Reactions were initiated by addition of equimolar ATP/MgCl₂ (0.5 mM final concentration, unless otherwise stated) with trace [γ -³²P] ATP. 1 μ L aliquots were removed and applied to a PEI-cellulose thin-layer chromatography plate. The PEI plate was developed with 0.3 M LiCl and 0.5 M formic acid, then dried. [γ -³²P] ATP and free [³²P] PO₄³⁻ were visualized with a PhosphorImager. Radioactivity intensities were quantified using ImageQuant TL software (GE) and the fraction ATP hydrolyzed was determined:

$$\text{Fraction hydrolyzed ATP} = \frac{PO_4^{3-} \text{ intensity}}{PO_4^{3-} \text{ intensity} + \text{ATP intensity}} \quad (\text{Eq.5})$$

Initial rates of ATP hydrolysis (v_0) were determined by linear least squares fit to the initial phase of the reaction (fraction hydrolyzed ATP < 0.15). Inhibition constants (K_i) for K7 binding were determined by fitting K7 titrations to a modified Michaelis-Menten equation:

$$v_0 = v_0^{max} - (v_x * \left(\frac{[I]}{K_i + [I]}\right)) \quad (\text{Eq.6})$$

v_0 = ATP hydrolysis rate constant, v_0^{max} = maximum ATP hydrolysis rate constant, v_x = minimum ATP hydrolysis rate constant, $[I]$ = inhibitor concentration, K_i = inhibition constant.

9.4 Formaldehyde crosslinking

Formaldehyde crosslinking was performed as previously described^{28,116}. Purified DDX3X, ΔDDX3X, Ded1p, and/or K7 were incubated for 1 hr at 19 °C or 30 °C in the presence or absence of 0.5 mM ADPNP and 2 μM non-radiolabeled R16/41-3, as indicated. Formaldehyde crosslinking was performed by adding 1% (v/v) formaldehyde to each reaction and incubating for 30 min at room temperature. Crosslinking reactions were quenched by adding 0.5 mM tris-glycine pH 6.8, followed by the addition of Laemmli sample buffer. Samples were resolved on 8% SDS-PAGE and immunoblotting against DDX3X (1:1500 DDX3X polyclonal antibody, ThermoFisher PA5-29170) or Ded1p (1:6,000 α-Ded1p, polyclonal antibody raised against full length Ded1p) was performed.

9.5 Liquid-liquid phase separation assays

DDX3X and Ded1p were labeled with Alexa Fluor 647 by incubating 60 μL protein with 5 μL of Alexa Fluor 647 NHS ester, tris(triethylammonium salt) (1 μg/μL in DMSO, ThermoFisher A37573) for 1 hr at room temperature. Excess

dye was removed by passing the labeling reaction through a total of three Zeba spin desalting columns 7K MWCO (ThermoFisher 89882). Concentration of fluorophore-labelled protein was determined by measuring the absorbance at 650 nM (absorption max for Alexa Fluor 647) and using the following equation:

$$c = \frac{Abs}{\epsilon * L} \quad (\text{Eq.7})$$

c is the molar concentration, Abs is the absorbance at 650 nM, ϵ is the molar extinction coefficient ($239,000 \text{ cm}^{-1}\text{M}^{-1}$ for Alexa Fluor 647), and L is the path length in centimeters.

LLPS assays were performed as previously described³⁷⁴. Liquid-liquid phase separation reaction mixtures (20 μL) containing 40 mM Tris-HCl pH 8.0, 50 mM (Ded1p reactions) or 70 mM (DDX3X reactions) NaCl, 0.5 mM MgCl_2 , 2 mM DTT, 1 unit/mL RNasin, 0.01% (v/v) IGEPAL CA-630, and 8% (Ded1p reactions) or 11% (DDX3X reactions) glycerol were incubated for 1 hr (Ded1p reactions) or 2 hr (DDX3X reactions) at room temperature with the indicated concentrations of DDX3X, Ded1p, and/or His-K7. 10 μL of each reaction were spotted on microscope slides, covered with coverslips, and imaged at 20X using a Leica DM6000 upright microscope with a Cy5 filter set (CWRU SOM light microscopy core facility, NIH grant S10-RR021228). 20 fluorescent images per condition per replicate were quantified using the nucleus counter tool of ImageJ with the following parameters: smallest particle size 1 μm , largest particle size 10,000 μm , Otsu thresholding, no smoothing, with background subtraction and watershed filter applied.

Ded1p turbidity measurements were performed by incubating 2 μ M Ded1p for 1 hr at room temperature in 100 μ L helicase reaction buffer (40 mM Tris pH 8.0, 0.5 mM MgCl₂, 0.01% IGEPAL CA-630, 2 mM DTT, 51.75 mM NaCl, 8.6% glycerol). Following incubation, the OD₆₀₀ (turbidity) was measured at room temperature in a Tecan Spark multimode multiplate reader with Te-Cool active temperature regulation.

9.6 Cloning

9.6.1 pEBB.myc-K7 / pEBB.myc

pEBB.myc was generated by performing Q5 mutagenesis (NEB E0554S) to remove HTRA2 coding sequence from pEBB.HTRA2-3xmyc (gift from Dr. Derek Abbott). Fwd primer: 5'-GGATCTACCATGGAGCAAAAGCTCA-3' / Rev primer: 5'-CATGGCGGCTCTAGAGAATCCTCA-3'

pEBB.myc-K7 was generated by PCR amplifying K7 from pET15b-His₆-K7 (gift from Dr. Amir R Khan) with the addition of BamHI and NotI restriction digest sites. Fwd primer: 5'-AATTTGGATCCATGGCGACCAAAGTGGATTATGAAGA-3' / Rev primer: 5'-GGCAGGCGGCCGCTTAGTTCAGTTTTTTTTTCCAGAAACAGG-3'. Resulting PCR product was gel purified using QIAquick gel extraction kit (Qiagen 28706X4). Gel-purified PCR product and pEBB.myc were digested overnight at 37 °C with BamHI and NotI. Digestion products were gel purified using QIAquick gel extraction kit (Qiagen 28706X4) and ligated overnight using 3:1 insert:vector at 16 °C with T4 ligase.

9.6.2 pEBB.DDX3XGFP-p2a-mycK7 / pEBB.DDX3XGFP-p2a-myc

pEBB.DDX3XGFP-p2a-mycK7 was generated by first cloning the DDX3X coding sequence from pET-SUMO-DDX3X into pCW57.GFP-2A-MCS (gift from Dr. Adam Karpf, Addgene plasmid # 71783; <http://n2t.net/addgene:71783> ; RRID:Addgene_71783) via *in vivo* assembly⁴¹⁹. Primers with annealing temperatures of 60 °C and 30 basepair overlaps were designed in Benchling (<https://benchling.com>) to amplify DDX3X coding sequence (fragment 2) and the pCW57.GFP-2A-MCS backbone (fragment 1). PCR reactions were performed using Q5 high-fidelity DNA polymerase (NEB M0491S).

pCW57.DDX3XGFP-2A-MCS Fwd primer fragment 1: 5'-

GTGGGGTAACGGTTCGGAGAGAGCGACGAGAGCGGC-3'

pCW57.DDX3XGFP-2A-MCS Rev primer fragment 1: 5'-

TGCCACATGACTCATGGTGGCGAATTCGCTAGCCA-3'

pCW57.DDX3XGFP-2A-MCS Fwd primer fragment 2: 5'-

AGCGAATTCGCCACCATGAGTCATGTGGCAGTGGAAAATGCG -3'

pCW57.DDX3XGFP-2A-MCS Rev primer fragment 2: 5'-

TCGTCGCTCTCTCCGGAACCGTTACCCCACCAGTCAACCCCC -3'

PCR products were gel purified using QIAquick gel extraction kit (Qiagen 28706X4) and *in vivo* assembly⁴¹⁹ was performed by mixing 5 ng/kb of each fragment together in 5 µL of water and transforming into Stbl3 *E. coli* (ThermoFisher C737303).

pEBB.DDX3XGFP-p2a-mycK7 was then generated using NEB HiFi DNA Assembly MasterMix (NEB E2621S). Primers with annealing temperatures of 60

°C and 30 basepair overlaps were designed in Benchling (<https://benchling.com>) to amplify DDX3XGFP-2A- coding sequence from pCW57.DDX3XGFP-2A-MCS (fragment 2) and the pEBB.mycK7 backbone (fragment 1 and 3, split into 2 fragments at ampicillin resistance cassette). PCR reactions were performed using Q5 high-fidelity DNA polymerase (NEB M0491S).

pEBB.DDX3XGFP-p2a-mycK7 Fwd primer fragment 1: 5'-

GAAAACCCCGGTCCTGGATCTACCATGGAGCAAAGCTCATCT-3'

pEBB.DDX3XGFP-p2a-mycK7 Rev primer fragment 1: 5'-

CGCAAAAAGGGAATAAGGGCGACACGG-3'

pEBB.DDX3XGFP-p2a-mycK7 Fwd primer fragment 2: 5'-

TTCTCTAGAGCCGCCATGAGTCATGTGGCAGTGGAAAATGC-3'

pEBB.DDX3XGFP-p2a-mycK7 Rev primer fragment 2: 5'-

CTCCATGGTAGATCCAGGACCGGGTTTTCTTCCACG-3'

pEBB.DDX3XGFP-p2a-mycK7 Fwd primer fragment 3: 5'-

CCGTGTCGCCCTTATTCCCTTTTTTGCG-3'

pEBB.DDX3XGFP-p2a-mycK7 Rev primer fragment 3: 5'-

TGCCACATGACTCATGGCGGCTCTAGAGAATCCTCACG-3'

pEBB.DDX3XGFP-p2a-myc was generated by performing Q5 mutagenesis (NEB E0554S) to remove the K7 coding sequence. Fwd primer: 5'-TAAGCGGCCGCGACTCTA-3' / Rev primer: 5'-CAGTTTGGTGC CCATGGAT-3'

9.6.3 Generation of DDX3X mutants (R534H, G302V, G325E, FFAA)

Q5 mutagenesis (NEB E0554S) was used to generate DDX3X mutants.

R534H Fwd primer: 5'-ACGGGACATGTAGGAAACC-3'

R534H Rev primer: 5'-ACGACCAATACGATGTACAT-3'

G302V Fwd primer: 5'-GTGGTTTATGTTGGTGCCGATA-3'

G302V Rev primer: 5'-GCAAGGACGAACTCTAGATCG-3'

G325E Fwd primer: 5'-CCACTCCAGAACGTCTAGTGGA-3'

G325E Rev primer: 5'-CTACTAACAAATGGCATCCACG-3'

FFAA Fwd primer: 5'-TCTAGCGCCGCCAGTGATCG-3'

FFAA Rev primer: 5'-CTTCCCTCTTGAATCACTACGAGATCC-3'

9.6.4 pMax.GFP-p2a-mycK7 / pMax.GFP-p2a-myc

pMax.GFP-p2a-mycK7 and pMax.GFP-p2a-myc were generated by first cloning DDX3XGFP-p2a-mycK7 and DDX3XGFP-p2a-myc into Lonza pMax.GFP vector (gift from Dr. Derek Abbott). DDX3XGFP-p2a-mycK7 and DDX3XGFP-p2a-myc were PCR amplified from pEBB.DDX3XGFP-p2a-mycK7 and pEBB.DDX3XGFP-p2a-myc with the addition of NheI and XhoI restriction digest sites. PCR reactions were performed using Q5 high-fidelity DNA polymerase (NEB M0491S). Fwd primer: 5'-

TAAGGAGCTAGCGCCGCCATGAGTCATGTGGC-3' / Rev primer: 5'-

TAAGGACTCGAGACTCTAGAGTCGCGGCCGCTTA-3'

Resulting PCR products were gel purified using QIAquick gel extraction kit (Qiagen 28706X4). Gel-purified PCR products and pMax.GFP were digested overnight at 37 °C with NheI and XhoI. Digestion products were gel purified using QIAquick gel extraction kit (Qiagen 28706X4) and ligated overnight using 3:1 insert:vector at 16 °C with T4 ligase.

pMax.GFP-p2a-mycK7 and pMax.GFP-p2a-myc were then generated by performing Q5 mutagenesis (NEB E0554S) to remove DDX3X coding sequence. Fwd primer: 5'-AACGGTTCCGGAGAGAGCG-3' / Rev primer: 5'-CATGGCGGCGCTAGC-3'

9.7 Immunofluorescence

HCT 116 cells were obtained from ATCC and grown at 37 °C and 5% CO₂ in McCoy's 5A medium, modified, with L-glutamine and sodium bicarbonate (Sigma-Aldrich M9309), supplemented with 5% FBS (ThermoFisher 26140-079) and 100 units/mL penicillin/streptomycin (ThermoFisher 15140122). Cells (~200,000) were plated onto glass coverslips in 6 well tissue culture plates (LPS 703001). 16-24 hr later, each well was transfected with 2 µg of the indicated plasmid using jetPRIME polyplus transfection reagent (VWR 89129-922). 24 hr after transfection cells were treated with 1 mM sodium arsenite for 1 hr or 1 µg/mL puromycin for 30 min, as indicated. Following treatment or ~ 24 hr after transfection for untreated cells, cells were fixed with 4% formaldehyde in phosphate-buffered saline (PBS) for 15 min at room temperature, then washed with PBS three times for 5 min at room temperature. Cells were then blocked for 1 hr at room temperature with 5% goat serum and 0.3% Triton X-100 in PBS and incubated overnight with primary antibody at 4 °C. Cells were then washed with PBS three times for 5 min at room temperature, incubated with secondary antibody for 2 hr at room temperature, washed with PBS three times for 5 min at room temperature, stained for 5 min with 300 nM DAPI in PBS, washed with PBS three times for 5 min at room temperature, then mounted on microscope slides

with Fluoromount-G (SouthernBiotech 0100-01) and stored at 4 °C until imaging. Slides were imaged either at 40X on a ThermoFisher EVOS M5000 imaging system or at 100X on a Leica DM6000 upright microscope (CWRU SOM light microscopy core facility, NIH grant S10-RR021228).

Primary antibodies (diluted in 0.3% Triton X-100, 0.01% (w/v) BSA in PBS): 1:100 anti-DDX3X (rabbit, Bethyl A300-474A); 1:100 anti-G3BP1 (mouse, Sigma-Aldrich WH0010146M1); 1:100 anti-Myc (mouse, ThermoFisher R950-25); 1:100 anti-puromycin (mouse, Sigma-Aldrich MABE343).

Secondary antibodies (diluted in 0.3% Triton X-100, 0.01% (w/v) BSA in PBS): 1:200 anti-mouse IgG CF594 (goat, Sigma-Aldrich SAB4600402-50UL); 1:200 anti-rabbit IgG CF594 (goat, Sigma-Aldrich SAB4600107-50UL); 1:200 anti-mouse IgG1 CF594 (goat, Sigma-Aldrich SAB4600325-50UL); 1:200 anti-mouse IgG1 CF488A (goat, Sigma-Aldrich SAB4600237-50UL); 1:200 anti-rabbit IgG CF647 (goat, Sigma-Aldrich SAB4600352-125UL); 1:200 anti-rabbit IgG CF555 (goat, Sigma-Aldrich SAB4600069-50UL).

9.7.1 Image analysis

For expression of myc-K7 without GFP (**Fig. 5.3**), 30 images from each condition (≥ 330 cells) per replicate ($n \geq 3$ biological replicates) were analyzed for total cell number and number of cells containing stress granules using the Cell Counter tool in ImageJ. Number of stress granules per cell in **Fig. 5.3** were determined by manually selecting individual cells using the Freehand tool in ImageJ, performing Shanbhag automatic thresholding, and using the ImageJ

analyze particles tool (size: 5-infinity μm^2 , circularity: 0-1) to detect stress granules.

For co-expression of GFP and myc-K7 (**Fig. 5.2**), 8 images from each condition (≥ 100 cells) per replicate ($n = 3$ biological replicates) were analyzed for the number of stress granules per GFP-positive cell in ImageJ. GFP-positive cells were identified by performing triangle auto thresholding. This threshold was then converted to a mask and the watershed function was performed to separate distinct cells in the mask. The analyze particles tool (size: 100-infinity μm^2 , circularity: 0-1) was used to identify individual GFP-positive cells from the mask. This mask was then applied to the DDX3X/G3BP channel to identify GFP-positive cells. A background subtraction with rolling ball radius 5 was performed on the DDX3X/G3BP channel and then the analyze particles tool (size: 0.1-infinity μm^2 , circularity: 0-1) was used to identify granules in each GFP-positive cell.

For identification of GFP-tagged DDX3X foci (**Fig. 5.5**), 115 GFP-positive cells from each condition/replicate ($n = 3$ biological replicates) were analyzed for the number of stress granules per GFP-positive cell in ImageJ. GFP-positive cells were identified by triangle auto thresholding. This threshold was then converted to a mask and the watershed function was performed to separate distinct cells in the mask. The analyze particles tool (size: 100-infinity μm^2 , circularity: 0-1) was used to identify individual GFP-positive cells from the mask. This mask was then applied to the non-thresholded GFP channel to identify GFP-positive cells. A background subtraction with rolling ball radius 1 was performed

on the non-thresholded GFP channel and then the analyze particles tool (size: 0.1-infinity μm^2 , circularity: 0-1) was used to identify granules in each GFP-positive cell. Additional mutants (**Fig. 8.5**) were analyzed for the presence of stress granules using the cell counter tool in ImageJ.

For quantification of puromycin staining intensity (**Fig. 6.3**), 9 images from each condition (≥ 129 cells) per replicate ($n = 3$ biological replicates) were analyzed in ImageJ. GFP-positive cells were identified by triangle auto thresholding. This threshold was then converted to a mask and the watershed function was performed to separate distinct cells in the mask. The analyze particles tool (size: 100-infinity μm^2 , circularity: 0-1) was used to identify individual GFP-positive cells from the mask. This mask was then applied to the puromycin channel to identify GFP-positive cells. The intensity in the puromycin channel for each GFP-positive cell was measured. Corrected total cell fluorescence for puromycin was determined by subtracting the background intensity from the puromycin intensity.

9.8 Western blotting

HCT 116 cells were obtained from ATCC and grown at 37 °C and 5% CO₂ in McCoy's 5A medium, modified, with L-glutamine and sodium bicarbonate (Sigma-Aldrich M9309), supplemented with 5% FBS (ThermoFisher 26140-079) and 100 units/mL penicillin/streptomycin (ThermoFisher 15140122). Cells (~200,000) were plated into 6 well tissue culture plates (LPS 703001) or ~1,000,000 cells were plated into 6 cm tissue culture plates (LPS 705001). 16-24 hr later, 6 well plates were transfected with 2 μg of the indicated plasmid and 6

cm plates were transfected with 4 µg of the indicated plasmid using jetPRIME polyplus transfection reagent (VWR 89129-922). 24 hr after transfection cells were harvested by scraping into 1 mL PBS and spinning at 300 g for 1 min at room temperature. Cell pellets were then resuspended in 100 µL lysis buffer (6 cm plates) or 30 µL lysis buffer (6 well plates) and vortexed briefly. Lysis buffer contained: 50 mM Tris-Cl pH 7.5, 150 mM NaCl, 1mM EDTA, 1% Triton X-100, 1 mM PMSF, and protease inhibitor tablet (Roche, 04693159001). Lysates were clarified by centrifuging 10 min at 13,000 rpm at 4 °C. The total protein concentration in each lysate was measured via Bradford assay (Bio-Rad 5000001), and lysates were mixed with Laemmli sample buffer then boiled for 2 min at 95 °C. 40 µg total protein from each lysate was resolved by SDS-PAGE then transferred to 0.2 µm PVDF membranes for 90 min at 4 °C at 130V using wet/tank transfer in transfer buffer (20% methanol, 0.02% SDS, 190 mM glycine, 25 mM Tris). Membranes were washed twice with PBS for 10 min, then blocked 1 hr at room temperature (10% milk or 5% BSA in PBS + 0.1% tween) and incubated with primary antibody overnight at 4 °C. Membranes were then washed once with PBS + 0.1% tween for 10 min and once with PBS for 10 min, then incubated with secondary antibody for 1 hr at room temperature. Membranes were then washed once with PBS + 0.1% tween for 10 min and once with PBS for 10 min, then treated with SuperSignal West Pico PLUS chemiluminescent substrate (ThermoFisher 34579) and visualized using a Syngene G:Box. Band intensities were quantified using ImageJ.

Primary antibodies: 1:1500 anti-DDX3X in 5% BSA (rabbit, Bethyl A300-474A); 1:1000 anti-myc in 5% milk (rat, Abcam ab206486); 1:2000 anti- β -tubulin in 5% milk (rabbit, Abcam ab15568).

Secondary antibodies: 1:2000 anti-rabbit IgG peroxidase in 5% milk (Sigma-Aldrich, A1949-1VL); 1:2000 anti-rat IgG peroxidase in 5% milk (Sigma-Aldrich, A5795-1ML).

9.9 Polysome profiling

Polysome profiling was performed as previously described⁵⁹ with some modifications. HCT 116 cells were obtained from ATCC and grown at 37 °C and 5% CO₂ in McCoy's 5A medium, modified, with L-glutamine and sodium bicarbonate (Sigma-Aldrich M9309), supplemented with 5% FBS (ThermoFisher 26140-079) and 100 units/mL penicillin/streptomycin (ThermoFisher 15140122). HCT 116 cells expressing degron-tagged DDX3X (gift from Dr. Stephen Floor) were grown under similar conditions. Cells were grown in 15 cm tissue culture plates (LPS 715001). 24 hr after plating, 15 cm plates were transfected with 20-30 μ g DNA using jetPRIME polyplus transfection reagent (VWR 89129-922) or treated with 500 μ M indole-3-acetic acid to induce degradation of degron-tagged DDX3X. Four 15 cm plates were transfected/treated per condition. 24-48 hr after transfection or treatment cells were harvested by scraping all four 15 cm plates into a total of 400 μ L lysis buffer (0.1 M Tris pH 7.4, 1 M NaCl, 0.3 M MgCl₂, 0.61 mg/mL cycloheximide, 1 mM DTT, 1% Triton X-100) on ice. Cells were lysed by drawing through a 27.5 gauge needle 20 times on ice, then clarified by spinning

10 min at 13,000 rpm at 4 °C. Lysates were then flash frozen and stored at -80 °C until sucrose gradient centrifugation.

Clarified lysates were loaded onto 15%-45% sucrose gradients and centrifuged at 41,000 rpm for 2.5 hr at 4 °C. Gradients were fractionated at a pump speed of $S = 0.9$ mL/min using a FoxyJr fractionator with concurrent monitoring of A_{260} to generate traces.

9.9.1 Analysis of polysome-associated proteins

For western blot analysis, 1 volume 20% trichloroacetic acid was added to each fraction and proteins were precipitated overnight at -20 °C. Samples were then centrifuged at 13,000 rpm at 4 °C for 10 min. Pellets were washed with cold 80% acetone then allowed to air dry. Dry pellets were resuspended in Laemmli buffer, boiled, and analyzed via SDS-PAGE.

9.10 Growth curves

HCT 116 cells were obtained from ATCC and grown at 37 °C and 5% CO₂ in McCoy's 5A medium, modified, with L-glutamine and sodium bicarbonate (Sigma-Aldrich M9309), supplemented with 5% FBS (ThermoFisher 26140-079) and 100 units/mL penicillin/streptomycin (ThermoFisher 15140122). Cells (~3000) were plated per well of 96 well plate (LPS 701001). 16 – 24 hr later each well was transfected with 0.1 µg DNA (pMax.GFP-p2a-myck7 or pMax.GFP-p2a-myc) using jetPRIME polyplus transfection reagent (VWR 89129-922). GFP-positivity was monitored daily using a ThermoFisher EVOS M5000 imaging system. Cell number was counted daily using a manual hemocytometer (4

technical replicates per condition per day). 3 biological replicates were completed. Population doubling time was calculated using the following equation:

$$DT = T * \frac{\ln 2}{\ln\left(\frac{X_e}{X_b}\right)} \quad (\text{Eq.8})$$

DT is the doubling time, T is the incubation time, X_e is the cell number at the end of the incubation time, and X_b is the cell number at the beginning of the incubation time.

9.11 CellTiter-Glo

HCT 116 cells were obtained from ATCC and grown at 37 °C and 5% CO₂ in McCoy's 5A medium, modified, with L-glutamine and sodium bicarbonate (Sigma-Aldrich M9309), supplemented with 5% FBS (ThermoFisher 26140-079) and 100 units/mL penicillin/streptomycin (ThermoFisher 15140122). Cells (~3000) were plated per well of 96 well plate (LPS 701001). 16 – 24 hr later each well was transfected with 0.1 µg DNA (pMax.GFP-p2a-myck7 or pMax.GFP-p2a-myc) using jetPRIME polyplus transfection reagent (VWR 89129-922). GFP-positivity was monitored daily using a ThermoFisher EVOS M5000 imaging system. CellTiter-Glo luminescent cell viability assay (Promega G7571) was completed daily (4 technical replicates per day). Luminescence was measured on a Molecular Devices SpectraMax M3. 3 biological replicates were completed.

9.12 MTT assay (adapted from³⁹⁶)

MTT assays were performed by Ben Dumm as previously described³⁹⁶. 20,000 HCT-116 cells/well were seeded onto a 96-well, clear bottom, tissue culture-treated polystyrene plate (Corning Life Sciences; cat. no. 353072) and grown for ~ 48 hr at 37 °C and 5% CO₂ until confluence > 90%. Cells were then

treated with fresh culture medium containing 0 to 1 mM bis-ANS for either 6 or 24 hr. Cell viability was then measured using the Cell Proliferation Kit (MTT, 3-(4,5-dimethylthiazol-2-yl)-2,5-diphenyltetrazolium bromide) (Roche; cat. no. 11465007001) according to the manufacturer-suggested protocol. Absorbance was measured on a Tecan Microplate reader at 600 nm, using a 700 nm reference wavelength. Cell viability was calculated as:

$$\text{Cell viability} = \frac{(OD_{600} - OD_{700})_{\text{treated cells}}}{(OD_{600} - OD_{700})_{\text{untreated cells}}} \quad (\text{Eq.9})$$

2 biological replicates with 2-3 technical replicates each were completed.

9.13 Live cell imaging with bis-ANS (adapted from³⁹⁶)

Live cell imaging was performed by Ben Dumm as previously described³⁹⁶. HCT-116 cells were plated onto 35 mm glass bottom culture dishes (Greiner bio one; cat. no. 627861), and grown overnight to ~ 70% confluence. Cells were treated with bis-ANS dissolved in culture medium, then washed three times with Dulbecco's phosphate-buffered saline (DPBS; Gibco; cat. no. 14190-144), and imaged in Fluorobrite™ Dulbecco's modified eagle medium (Gibco; cat. No. A18967-01). Draq5 (Thermo Scientific; 62254) was added to the imaging media at 1:1000 ratio to stain the nuclei. Cells were imaged with a 40X water immersion objective on the Leica TCS SP8 confocal microscope, using a live-cell incubation chamber to maintain the samples at 37 °C and 5% CO₂. Bis-ANS was excited using a 405 nm laser and emission was collected from 500 to 545 nm, and Draq5 was excited using a 633 nm laser and emission was collected from 675 to 725 nm.

9.14 Propidium iodide staining

HCT 116 cells were obtained from ATCC and grown at 37 °C and 5% CO₂ in McCoy's 5A medium, modified, with L-glutamine and sodium bicarbonate (Sigma-Aldrich M9309), supplemented with 5% FBS (ThermoFisher 26140-079) and 100 units/mL penicillin/streptomycin (ThermoFisher 15140122). Cells (~200,000) were plated per well of 6 well plate (LPS 703001). 16 – 24 hr later each well was transfected with 2 µg DNA (pMax.mycK7 or pMax.myc) using jetPRIME polyplus transfection reagent (VWR 89129-922). 24 hr after transfection cells were treated with 1 mM sodium arsenite for the indicated times. After sodium arsenite treatment, 1 µg/mL propidium iodide was added and cells were incubated for 15 min at 37 °C. Cells were imaged at 20X on a ThermoFisher EVOS M5000 imaging system. 5 images from each condition were analyzed for propidium iodide staining using the cell counter tool in ImageJ.

Appendix 1

Evidence for DEAD-box RNA helicase dysregulation in cancer

(Generated with the help of Soon Yeul Yi)

DEAD-box Helicase	Cancer	Reference PMIDs
EIF4A1/DDX2A	Brain Cancer	33299354, 33807050
	Breast Cancer	25611378
	Cervical Cancer	24844222, 29163714
	Colon/Colorectal Cancer	28466778, 28627973
	Endometrial/Uterine Cancer	22415234
	Gallbladder Cancer	33416145
	Gastric Cancer	32147684, 31190893, 26936591
	Head and Neck Cancer	31807078, 24294361
	Kidney Cancer	33133154, 35117342, 33488680, 33461173
	Leukemia	34127794
	Liver Cancer	16820872
	Lung Cancer	12970751, 12019437
	Lymphoma	29844128, 33037136
	Ovarian Cancer	27836619
	Pancreatic Cancer	34906136
	Sarcoma	26951381
Skin Cancer	27879264, 32971126, 12085193, 9139875	
EIF4A2/DDX2B	Breast Cancer	31308851, 21219636
	Colon/Colorectal Cancer	31088567
	Endometrial/Uterine Cancer	32877461
	Esophageal Cancer	32934744
	Lung Cancer	23867391
	Lymphoma	12738680
	Mesothelioma	14987796
	Ovarian Cancer	27836619
	Sarcoma	26951381
EIF4A3/DDX48	Bladder Cancer	34702726, 33176280
	Brain Cancer	32926734, 30470262

	Breast Cancer	32264877, 34325714, 31187432
	Cervical Cancer	34278492, 33675124
	Colon/Colorectal Cancer	34660182, 26989025, 34253241, 32857753
	Gallbladder Cancer	34727877
	Gastric Cancer	32592202, 29973643, 31637706
	Liver Cancer	31898336, 33750838, 25690035
	Lung Cancer	32281700, 33924522
	Ovarian Cancer	29571014
	Pancreatic Cancer	15796914, 31541081
	Prostate Cancer	34599930, 34696782
DDX6	Brain Cancer	26610392
	Colon/Colorectal Cancer	18769115, 11751426, 10360675
	Gastric Cancer	29987267, 29314290, 23932921, 30959742
	Leukemia	17427874, 12946992
	Liver Cancer	12823589
	Lymphoma	22965301
	Testicular Cancer	29769412
DDX19A	Breast Cancer	24866763
DDX19B	Liver Cancer	34312475
DDX25	Kidney Cancer	33456353
DDX39A	Adrenal Gland Cancer	31188873, 26469522
	Bladder Cancer	22494014
	Liver Cancer	34288818, 29867138
	Lung Cancer	17548965
	Mesothelioma	23749908
	Prostate Cancer	28025139
	Sarcoma	22723667, 22119546
DDX39B	Breast Cancer	33020551
	Colon/Colorectal Cancer	33436563
	Kidney Cancer	34382524
	Ovarian Cancer	32989256
	Prostate Cancer	28025139
DDX20	Bladder Cancer	23322153
	Head and Neck Cancer	34290392

	Liver Cancer	32449268, 22445758, 22898998
	Prostate Cancer	27121695
DDX18	Breast Cancer	25284587, 30302816
	Colon/Colorectal Cancer	32815531
	Esophageal Cancer	33345608
DDX10	Brain Cancer	34797290
	Breast Cancer	23496902
	Leukemia	23522748, 9166830, 20339440, 26004809, 10502319
	Lung Cancer	33973712
	Ovarian Cancer	26713367
	Sarcoma	34797290, 30738579
DDX55	Liver Cancer	32128678
DDX31	Bladder Cancer	29440146
	Brain Cancer	31233712
	Kidney Cancer	23019224
DDX47	Kidney Cancer	33456353
	Leukemia	19654405
DDX49	Liver Cancer	33952717
	Lung Cancer	31749282, 33089952
DDX27	Breast Cancer	34362383
	Colon/Colorectal Cancer	29535419
	Gastric Cancer	25742747
	Liver Cancer	26067772
DDX54	Gastric Cancer	32712782
DDX3X	Brain Cancer	26184164, 30292066, 33405951, 33172502, 24651015, 22832583, 22820256, 22722829
	Breast Cancer	33974127, 28869602, 28761359, 28138868, 27999982, 26087195, 23696831, 33608512
	Cervical Cancer	33535306
	Colon/Colorectal Cancer	31391454, 28761359, 28435452, 27007150, 26892600, 26311743, 26087195
	Gallbladder Cancer	23330003

	Head and Neck Cancer	29921696, 26087195, 25406365, 25056374, 21798893, 31974865, 23410059, 30563911, 24292195
	Kidney Cancer	32326089
	Leukemia	28033648, 34189564, 29358183, 27503198, 26053404, 25382417, 22150006, 30347268, 29674644, 24584351, 23673860
	Liver Cancer	27344963, 16301996, 14985104, 16818630
	Lung Cancer	25820276, 21325288, 23584477
	Lymphoma	34654425, 30733272, 31738823, 31300419, 34437837, 31822801, 26773734, 26192917
	Mesothelioma	27813512, 26928227
	Pancreatic Cancer	26294807, 33386519
	Prostate Cancer	33106406, 30926334, 27634756
	Sarcoma	26364611
	Skin cancer	16818630, 31216476
DDX3Y	Lymphoma	34437837
DDX4	Leukemia	28612512
	Myeloma	28612512
	Ovarian Cancer	18805576, 24727449, 34517544, 29078734, 32847044
DDX53	Breast Cancer	28152297
	Cervical Cancer	30454700, 16819299, 20220142, 11922625
	Endometrial/Uterine Cancer	15897597
	Gastric Cancer	11922625, 12849980
	Head and Neck Cancer	33506900
	Kidney Cancer	11922625
	Leukemia	33101773
Liver Cancer	24174534, 16819299, 28099142, 11922625, 20534591, 17028776	

	Lung Cancer	11922625
	Skin Cancer	28535666, 26863629, 24174534, 28099142, 26883907, 20220142, 20534591, 17341616
DDX43	Brain Cancer	24573400
	Breast Cancer	24755885, 26240276
	Eye Cancer	24899684
	Leukemia	29449695, 24656837, 23495895, 12399967, 22040965
	Lung Cancer	29044003
	Skin Cancer	22393060, 24525737
DDX5	Brain Cancer	32008867, 22810421
	Breast Cancer	34923193, 34936874, 22086602
	Cervical Cancer	28443473
	Colon/Colorectal Cancer	29988738, 17699760, 11753651
	Endometrial/Uterine Cancer	31032220
	Esophageal Cancer	33169694
	Gastric Cancer	28216662
	Head and Neck Cancer	8104427, 19347935
	Liver Cancer	23398123, 30119889
	Leukemia	23108395
	Lung Cancer	26212035
	Myeloma	19171422
	Pancreatic Cancer	33097588
	Skin Cancer	22548649
DDX17	Brain Cancer	32008867
	Breast Cancer	19718048
	Colon/Colorectal Cancer	31510013, 17699760
	Gastric Cancer	34012635
	Liver Cancer	31653828, 23398123
DDX23	Brain Cancer	26121981
	Leukemia	31855738
	Liver Cancer	33990545
	Lung Cancer	28473661
DDX46	Colon/Colorectal Cancer	25680556
	Esophageal Cancer	27176873

	Gastric Cancer	33347858
	Leukemia	27078856
	Sarcoma	27697093
	Skin Cancer	33000271
DDX41	Breast Cancer	32965163
	Leukemia	34644397, 31484648, 26712909, 25920683, 34671111, 34482403, 32868804, 33929502, 34723452, 34390506, 33585199, 30963592, 28031539
	Lung Cancer	34876838
DDX51	Esophageal Cancer	35125830
	Leukemia	17363581
	Lung Cancer	27198888
	Mesothelioma	26928227
DDX56	Brain Cancer	33789112
	Colon/Colorectal Cancer	31390121
	Lung Cancer	34446021
DDX21	Adrenal Gland Cancer	33497018
	Breast Cancer	25260534, 18561318
	Colon/Colorectal Cancer	21304002, 34903139, 35116878
	Gastric Cancer	30322617
	Prostate Cancer	34184132
	Sarcoma	33754909
DDX50	Colon/Colorectal Cancer	34476575
DDX1	Adrenal Gland Cancer	12880964, 32915406, 17028906, 15226335, 8622876, 7731693
	Breast Cancer	21761397, 20499159
	Kidney Cancer	25176654
	Myeloma	34680866
	Ovarian Cancer	25176654
DDX24	Breast Cancer	28223711, 25867071
	Cervical Cancer	28223711
	Gastric Cancer	28223711, 30367141
	Sarcoma	33754909
DDX59	Brain Cancer	31111544
	Lung Cancer	29133145

DDX52	Skin Cancer	34233596
DDX28	Brain Cancer	31907278
DDX26A	Colon/Colorectal Cancer	34508742
	Esophageal Cancer	12527901
	Liver Cancer	25686840, 28899352
	Lung Cancer	10467397, 15254679
	Prostate Cancer	16007164, 29895194, 15254679
	Testicular Cancer	17167184

Bibliography

- 1 Jankowsky, E. RNA helicases at work: binding and rearranging. *Trends Biochem Sci* **36**, 19-29, doi:10.1016/j.tibs.2010.07.008 (2011).
- 2 Pyle, A. M. Translocation and unwinding mechanisms of RNA and DNA helicases. *Annu Rev Biophys* **37**, 317-336, doi:10.1146/annurev.biophys.37.032807.125908 (2008).
- 3 Anantharaman, V., Koonin, E. V. & Aravind, L. Comparative genomics and evolution of proteins involved in RNA metabolism. *Nucleic Acids Res* **30**, 1427-1464, doi:10.1093/nar/30.7.1427 (2002).
- 4 Bourgeois, C. F., Mortreux, F. & Auboeuf, D. The multiple functions of RNA helicases as drivers and regulators of gene expression. *Nat Rev Mol Cell Biol* **17**, 426-438, doi:10.1038/nrm.2016.50 (2016).
- 5 Jankowsky, E. & Fairman, M. E. RNA helicases--one fold for many functions. *Curr Opin Struct Biol* **17**, 316-324, doi:10.1016/j.sbi.2007.05.007 (2007).
- 6 Fairman-Williams, M. E., Guenther, U. P. & Jankowsky, E. SF1 and SF2 helicases: family matters. *Curr Opin Struct Biol* **20**, 313-324, doi:10.1016/j.sbi.2010.03.011 (2010).
- 7 Jarmoskaite, I. & Russell, R. RNA helicase proteins as chaperones and remodelers. *Annu Rev Biochem* **83**, 697-725, doi:10.1146/annurev-biochem-060713-035546 (2014).
- 8 Tanaka, N. & Schwer, B. Characterization of the NTPase, RNA-binding, and RNA helicase activities of the DEAH-box splicing factor Prp22. *Biochemistry* **44**, 9795-9803, doi:10.1021/bi050407m (2005).
- 9 Fiorini, F., Bagchi, D., Le Hir, H. & Croquette, V. Human Upf1 is a highly processive RNA helicase and translocase with RNP remodelling activities. *Nat Commun* **6**, 7581, doi:10.1038/ncomms8581 (2015).
- 10 Johnson, S. J. & Jackson, R. N. Ski2-like RNA helicase structures: common themes and complex assemblies. *RNA Biol* **10**, 33-43, doi:10.4161/rna.22101 (2013).
- 11 Patrick, E. M., Srinivasan, S., Jankowsky, E. & Comstock, M. J. The RNA helicase Mtr4p is a duplex-sensing translocase. *Nat Chem Biol* **13**, 99-104, doi:10.1038/nchembio.2234 (2017).
- 12 Linder, P. & Jankowsky, E. From unwinding to clamping - the DEAD box RNA helicase family. *Nat Rev Mol Cell Biol* **12**, 505-516, doi:10.1038/nrm3154 (2011).
- 13 Fairman, M. E. *et al.* Protein displacement by DExH/D "RNA helicases" without duplex unwinding. *Science* **304**, 730-734, doi:10.1126/science.1095596 (2004).

- 14 Bowers, H. A. *et al.* Discriminatory RNP remodeling by the DEAD-box protein DED1. *RNA* **12**, 903-912, doi:10.1261/rna.2323406 (2006).
- 15 Jankowsky, E., Gross, C. H., Shuman, S. & Pyle, A. M. Active disruption of an RNA-protein interaction by a DExH/D RNA helicase. *Science* **291**, 121-125, doi:10.1126/science.291.5501.121 (2001).
- 16 Ohrt, T. *et al.* Prp2-mediated protein rearrangements at the catalytic core of the spliceosome as revealed by dcFCCS. *RNA* **18**, 1244-1256, doi:10.1261/rna.033316.112 (2012).
- 17 Chen, Y. *et al.* DEAD-box proteins can completely separate an RNA duplex using a single ATP. *Proc Natl Acad Sci U S A* **105**, 20203-20208, doi:10.1073/pnas.0811075106 (2008).
- 18 Rawling, D. C., Fitzgerald, M. E. & Pyle, A. M. Establishing the role of ATP for the function of the RIG-I innate immune sensor. *Elife* **4**, doi:10.7554/eLife.09391 (2015).
- 19 Lassig, C. *et al.* ATP hydrolysis by the viral RNA sensor RIG-I prevents unintentional recognition of self-RNA. *Elife* **4**, doi:10.7554/eLife.10859 (2015).
- 20 Shen, J., Zhang, L. & Zhao, R. Biochemical characterization of the ATPase and helicase activity of UAP56, an essential pre-mRNA splicing and mRNA export factor. *J Biol Chem* **282**, 22544-22550, doi:10.1074/jbc.M702304200 (2007).
- 21 Sharma, D., Putnam, A. A. & Jankowsky, E. Biochemical Differences and Similarities between the DEAD-Box Helicase Orthologs DDX3X and Ded1p. *J Mol Biol* **429**, 3730-3742, doi:10.1016/j.jmb.2017.10.008 (2017).
- 22 O'Day, C. L., Dalbadie-McFarland, G. & Abelson, J. The *Saccharomyces cerevisiae* Prp5 protein has RNA-dependent ATPase activity with specificity for U2 small nuclear RNA. *J Biol Chem* **271**, 33261-33267, doi:10.1074/jbc.271.52.33261 (1996).
- 23 Theissen, B., Karow, A. R., Kohler, J., Gubaev, A. & Klostermeier, D. Cooperative binding of ATP and RNA induces a closed conformation in a DEAD box RNA helicase. *Proc Natl Acad Sci U S A* **105**, 548-553, doi:10.1073/pnas.0705488105 (2008).
- 24 Andreou, A. Z. & Klostermeier, D. Conformational changes of DEAD-box helicases monitored by single molecule fluorescence resonance energy transfer. *Methods Enzymol* **511**, 75-109, doi:10.1016/B978-0-12-396546-2.00004-8 (2012).
- 25 Mallam, A. L. *et al.* Solution structures of DEAD-box RNA chaperones reveal conformational changes and nucleic acid tethering by a basic tail. *Proc Natl Acad Sci U S A* **108**, 12254-12259, doi:10.1073/pnas.1109566108 (2011).

- 26 Putnam, A. A. & Jankowsky, E. DEAD-box helicases as integrators of RNA, nucleotide and protein binding. *Biochim Biophys Acta* **1829**, 884-893, doi:10.1016/j.bbagr.2013.02.002 (2013).
- 27 Srinivasan, S., Liu, Z., Chuenchor, W., Xiao, T. S. & Jankowsky, E. Function of Auxiliary Domains of the DEAH/RHA Helicase DHX36 in RNA Remodeling. *J Mol Biol* **432**, 2217-2231, doi:10.1016/j.jmb.2020.02.005 (2020).
- 28 Putnam, A. A. *et al.* Division of Labor in an Oligomer of the DEAD-Box RNA Helicase Ded1p. *Mol Cell* **59**, 541-552, doi:10.1016/j.molcel.2015.06.030 (2015).
- 29 Song, H. & Ji, X. The mechanism of RNA duplex recognition and unwinding by DEAD-box helicase DDX3X. *Nat Commun* **10**, 3085, doi:10.1038/s41467-019-11083-2 (2019).
- 30 Klostermeier, D. & Rudolph, M. G. A novel dimerization motif in the C-terminal domain of the *Thermus thermophilus* DEAD box helicase Hera confers substantial flexibility. *Nucleic Acids Res* **37**, 421-430, doi:10.1093/nar/gkn947 (2009).
- 31 Marcaida, M. J. *et al.* The Human RNA Helicase DDX21 Presents a Dimerization Interface Necessary for Helicase Activity. *iScience* **23**, 101811, doi:10.1016/j.isci.2020.101811 (2020).
- 32 Xu, L. *et al.* Insights into the Structure of Dimeric RNA Helicase CsdA and Indispensable Role of Its C-Terminal Regions. *Structure* **25**, 1795-1808 e1795, doi:10.1016/j.str.2017.09.013 (2017).
- 33 Yang, Q. & Jankowsky, E. ATP- and ADP-dependent modulation of RNA unwinding and strand annealing activities by the DEAD-box protein DED1. *Biochemistry* **44**, 13591-13601, doi:10.1021/bi0508946 (2005).
- 34 Wu, Y. Unwinding and rewinding: double faces of helicase? *J Nucleic Acids* **2012**, 140601, doi:10.1155/2012/140601 (2012).
- 35 Stampfl, S., Doetsch, M., Beich-Frandsen, M. & Schroeder, R. Characterization of the kinetics of RNA annealing and strand displacement activities of the *E. coli* DEAD-box helicase CsdA. *RNA Biol* **10**, 149-156, doi:10.4161/rna.23475 (2013).
- 36 Young, C. L., Khoshnevis, S. & Karbstein, K. Cofactor-dependent specificity of a DEAD-box protein. *Proc Natl Acad Sci U S A* **110**, E2668-2676, doi:10.1073/pnas.1302577110 (2013).
- 37 Jankowsky, E. & Putnam, A. Duplex unwinding with DEAD-box proteins. *Methods Mol Biol* **587**, 245-264, doi:10.1007/978-1-60327-355-8_18 (2010).
- 38 Putnam, A. & Jankowsky, E. Analysis of duplex unwinding by RNA helicases using stopped-flow fluorescence spectroscopy. *Methods Enzymol* **511**, 1-27, doi:10.1016/B978-0-12-396546-2.00001-2 (2012).

- 39 Sharma, D. & Jankowsky, E. The Ded1/DDX3 subfamily of DEAD-box RNA helicases. *Crit Rev Biochem Mol Biol* **49**, 343-360, doi:10.3109/10409238.2014.931339 (2014).
- 40 Giraud, G., Terrone, S. & Bourgeois, C. F. Functions of DEAD box RNA helicases DDX5 and DDX17 in chromatin organization and transcriptional regulation. *BMB Rep* **51**, 613-622 (2018).
- 41 Yao, W. *et al.* LncRNA CBR3-AS1 promotes osteosarcoma progression through the network of miR-140-5p/DDX54-NUCKS1-mTOR signaling pathway. *Mol Ther Oncolytics* **25**, 189-200, doi:10.1016/j.omto.2022.03.001 (2022).
- 42 Liu, B. *et al.* MYBL2-induced PITPNA-AS1 upregulates SIK2 to exert oncogenic function in triple-negative breast cancer through miR-520d-5p and DDX54. *J Transl Med* **19**, 333, doi:10.1186/s12967-021-02956-6 (2021).
- 43 Tedeschi, F. A., Cloutier, S. C., Tran, E. J. & Jankowsky, E. The DEAD-box protein Dbp2p is linked to noncoding RNAs, the helicase Sen1p, and R-loops. *RNA* **24**, 1693-1705, doi:10.1261/rna.067249.118 (2018).
- 44 Santos-Pereira, J. M. & Aguilera, A. R loops: new modulators of genome dynamics and function. *Nat Rev Genet* **16**, 583-597, doi:10.1038/nrg3961 (2015).
- 45 Rajendran, R. R. *et al.* Regulation of nuclear receptor transcriptional activity by a novel DEAD box RNA helicase (DP97). *J Biol Chem* **278**, 4628-4638, doi:10.1074/jbc.M210066200 (2003).
- 46 Kanno, Y., Serikawa, T., Inajima, J. & Inouye, Y. DP97, a DEAD box DNA/RNA helicase, is a target gene-selective co-regulator of the constitutive androstane receptor. *Biochem Biophys Res Commun* **426**, 38-42, doi:10.1016/j.bbrc.2012.08.027 (2012).
- 47 Calo, E. *et al.* RNA helicase DDX21 coordinates transcription and ribosomal RNA processing. *Nature* **518**, 249-253, doi:10.1038/nature13923 (2015).
- 48 De, I., Schmitzova, J. & Pena, V. The organization and contribution of helicases to RNA splicing. *Wiley Interdiscip Rev RNA* **7**, 259-274, doi:10.1002/wrna.1331 (2016).
- 49 Carmody, S. R. & Wentz, S. R. mRNA nuclear export at a glance. *J Cell Sci* **122**, 1933-1937, doi:10.1242/jcs.041236 (2009).
- 50 Strasser, K. & Hurt, E. Splicing factor Sub2p is required for nuclear mRNA export through its interaction with Yra1p. *Nature* **413**, 648-652, doi:10.1038/35098113 (2001).
- 51 Lund, M. K. & Guthrie, C. The DEAD-box protein Dbp5p is required to dissociate Mex67p from exported mRNPs at the nuclear rim. *Mol Cell* **20**, 645-651, doi:10.1016/j.molcel.2005.10.005 (2005).

- 52 Tran, E. J., Zhou, Y., Corbett, A. H. & Wente, S. R. The DEAD-box protein Dbp5 controls mRNA export by triggering specific RNA:protein remodeling events. *Mol Cell* **28**, 850-859, doi:10.1016/j.molcel.2007.09.019 (2007).
- 53 Awasthi, S. *et al.* DDX49 is an RNA helicase that affects translation by regulating mRNA export and the levels of pre-ribosomal RNA. *Nucleic Acids Res* **46**, 6304-6317, doi:10.1093/nar/gky231 (2018).
- 54 Ren, X. *et al.* Avian Influenza A Virus Polymerase Recruits Cellular RNA Helicase eIF4A3 to Promote Viral mRNA Splicing and Spliced mRNA Nuclear Export. *Front Microbiol* **10**, 1625, doi:10.3389/fmicb.2019.01625 (2019).
- 55 Yedavalli, V. S., Neuveut, C., Chi, Y. H., Kleiman, L. & Jeang, K. T. Requirement of DDX3 DEAD box RNA helicase for HIV-1 Rev-RRE export function. *Cell* **119**, 381-392, doi:10.1016/j.cell.2004.09.029 (2004).
- 56 Aitken, C. E. & Lorsch, J. R. A mechanistic overview of translation initiation in eukaryotes. *Nat Struct Mol Biol* **19**, 568-576, doi:10.1038/nsmb.2303 (2012).
- 57 Li, Q. *et al.* Eukaryotic translation initiation factor 4AIII (eIF4AIII) is functionally distinct from eIF4AI and eIF4AII. *Mol Cell Biol* **19**, 7336-7346, doi:10.1128/MCB.19.11.7336 (1999).
- 58 Pelletier, J. & Sonenberg, N. The Organizing Principles of Eukaryotic Ribosome Recruitment. *Annu Rev Biochem* **88**, 307-335, doi:10.1146/annurev-biochem-013118-111042 (2019).
- 59 Guenther, U. P. *et al.* The helicase Ded1p controls use of near-cognate translation initiation codons in 5' UTRs. *Nature* **559**, 130-134, doi:10.1038/s41586-018-0258-0 (2018).
- 60 Calviello, L. *et al.* DDX3 depletion represses translation of mRNAs with complex 5' UTRs. *Nucleic Acids Res* **49**, 5336-5350, doi:10.1093/nar/gkab287 (2021).
- 61 Oh, S. *et al.* Medulloblastoma-associated DDX3 variant selectively alters the translational response to stress. *Oncotarget* **7**, 28169-28182, doi:10.18632/oncotarget.8612 (2016).
- 62 Valentin-Vega, Y. A. *et al.* Cancer-associated DDX3X mutations drive stress granule assembly and impair global translation. *Sci Rep* **6**, 25996, doi:10.1038/srep25996 (2016).
- 63 Sen, N. D. *et al.* Functional interplay between DEAD-box RNA helicases Ded1 and Dbp1 in preinitiation complex attachment and scanning on structured mRNAs in vivo. *Nucleic Acids Res* **47**, 8785-8806, doi:10.1093/nar/gkz595 (2019).
- 64 Sen, N. D., Zhou, F., Ingolia, N. T. & Hinnebusch, A. G. Genome-wide analysis of translational efficiency reveals distinct but overlapping

- functions of yeast DEAD-box RNA helicases Ded1 and eIF4A. *Genome Res* **25**, 1196-1205, doi:10.1101/gr.191601.115 (2015).
- 65 Mercer, M., Jang, S., Ni, C. & Buszczak, M. The Dynamic Regulation of mRNA Translation and Ribosome Biogenesis During Germ Cell Development and Reproductive Aging. *Front Cell Dev Biol* **9**, 710186, doi:10.3389/fcell.2021.710186 (2021).
- 66 Johnstone, O. & Lasko, P. Interaction with eIF5B is essential for Vasa function during development. *Development* **131**, 4167-4178, doi:10.1242/dev.01286 (2004).
- 67 Nott, A., Le Hir, H. & Moore, M. J. Splicing enhances translation in mammalian cells: an additional function of the exon junction complex. *Genes Dev* **18**, 210-222, doi:10.1101/gad.1163204 (2004).
- 68 Tsai-Morris, C. H., Sheng, Y., Gutti, R. K., Tang, P. Z. & Dufau, M. L. Gonadotropin-regulated testicular RNA helicase (GRTH/DDX25): a multifunctional protein essential for spermatogenesis. *J Androl* **31**, 45-52, doi:10.2164/jandrol.109.008219 (2010).
- 69 Radhakrishnan, A. *et al.* The DEAD-Box Protein Dhh1p Couples mRNA Decay and Translation by Monitoring Codon Optimality. *Cell* **167**, 122-132 e129, doi:10.1016/j.cell.2016.08.053 (2016).
- 70 Li, Z. *et al.* RNA-binding protein DDX1 is responsible for fatty acid-mediated repression of insulin translation. *Nucleic Acids Res* **46**, 12052-12066, doi:10.1093/nar/gky867 (2018).
- 71 Kim, Y. K. & Maquat, L. E. UPFront and center in RNA decay: UPF1 in nonsense-mediated mRNA decay and beyond. *RNA* **25**, 407-422, doi:10.1261/rna.070136.118 (2019).
- 72 Garneau, N. L., Wilusz, J. & Wilusz, C. J. The highways and byways of mRNA decay. *Nat Rev Mol Cell Biol* **8**, 113-126, doi:10.1038/nrm2104 (2007).
- 73 Callahan, K. P. & Butler, J. S. TRAMP complex enhances RNA degradation by the nuclear exosome component Rrp6. *J Biol Chem* **285**, 3540-3547, doi:10.1074/jbc.M109.058396 (2010).
- 74 Jia, H. *et al.* The RNA helicase Mtr4p modulates polyadenylation in the TRAMP complex. *Cell* **145**, 890-901, doi:10.1016/j.cell.2011.05.010 (2011).
- 75 Houseley, J., LaCava, J. & Tollervey, D. RNA-quality control by the exosome. *Nat Rev Mol Cell Biol* **7**, 529-539, doi:10.1038/nrm1964 (2006).
- 76 Metze, S., Herzog, V. A., Ruepp, M. D. & Muhlemann, O. Comparison of EJC-enhanced and EJC-independent NMD in human cells reveals two partially redundant degradation pathways. *RNA* **19**, 1432-1448, doi:10.1261/rna.038893.113 (2013).

- 77 Ye, J. *et al.* Eukaryotic Initiation Factor 4A-3: A Review of Its Physiological Role and Involvement in Oncogenesis. *Front Oncol* **11**, 712045, doi:10.3389/fonc.2021.712045 (2021).
- 78 Martin, R., Straub, A. U., Doebele, C. & Bohnsack, M. T. DExD/H-box RNA helicases in ribosome biogenesis. *RNA Biol* **10**, 4-18, doi:10.4161/rna.21879 (2013).
- 79 Klinge, S. & Woolford, J. L., Jr. Ribosome assembly coming into focus. *Nat Rev Mol Cell Biol* **20**, 116-131, doi:10.1038/s41580-018-0078-y (2019).
- 80 Sloan, K. E. *et al.* The association of late-acting snoRNPs with human pre-ribosomal complexes requires the RNA helicase DDX21. *Nucleic Acids Res* **43**, 553-564, doi:10.1093/nar/gku1291 (2015).
- 81 Valdez, B. C., Perlaky, L. & Henning, D. Expression, cellular localization, and enzymatic activities of RNA helicase II/Gu(beta). *Exp Cell Res* **276**, 249-263, doi:10.1006/excr.2002.5538 (2002).
- 82 Kirchner, S. & Ignatova, Z. Emerging roles of tRNA in adaptive translation, signalling dynamics and disease. *Nat Rev Genet* **16**, 98-112, doi:10.1038/nrg3861 (2015).
- 83 Popow, J., Schleiffer, A. & Martinez, J. Diversity and roles of (t)RNA ligases. *Cell Mol Life Sci* **69**, 2657-2670, doi:10.1007/s00018-012-0944-2 (2012).
- 84 Jurkin, J. *et al.* The mammalian tRNA ligase complex mediates splicing of XBP1 mRNA and controls antibody secretion in plasma cells. *EMBO J* **33**, 2922-2936, doi:10.15252/embj.201490332 (2014).
- 85 Valadkhan, S. & Gunawardane, L. S. Role of small nuclear RNAs in eukaryotic gene expression. *Essays Biochem* **54**, 79-90, doi:10.1042/bse0540079 (2013).
- 86 Curmi, F. & Cauchi, R. J. The multiple lives of DEAD-box RNA helicase DP103/DDX20/Gemin3. *Biochem Soc Trans* **46**, 329-341, doi:10.1042/BST20180016 (2018).
- 87 Pfliederer, M. M. & Galej, W. P. Emerging insights into the function and structure of the Integrator complex. *Transcription* **12**, 251-265, doi:10.1080/21541264.2022.2047583 (2021).
- 88 Gubitz, A. K., Feng, W. & Dreyfuss, G. The SMN complex. *Exp Cell Res* **296**, 51-56, doi:10.1016/j.yexcr.2004.03.022 (2004).
- 89 Macfarlane, L. A. & Murphy, P. R. MicroRNA: Biogenesis, Function and Role in Cancer. *Curr Genomics* **11**, 537-561, doi:10.2174/138920210793175895 (2010).
- 90 Moy, R. H. *et al.* Stem-loop recognition by DDX17 facilitates miRNA processing and antiviral defense. *Cell* **158**, 764-777, doi:10.1016/j.cell.2014.06.023 (2014).

- 91 Lambert, M. P. *et al.* The RNA helicase DDX17 controls the transcriptional activity of REST and the expression of proneural microRNAs in neuronal differentiation. *Nucleic Acids Res* **46**, 7686-7700, doi:10.1093/nar/gky545 (2018).
- 92 Liu, Y. *et al.* The emerging role of the piRNA/piwi complex in cancer. *Mol Cancer* **18**, 123, doi:10.1186/s12943-019-1052-9 (2019).
- 93 Ku, H. Y. & Lin, H. PIWI proteins and their interactors in piRNA biogenesis, germline development and gene expression. *Natl Sci Rev* **1**, 205-218, doi:10.1093/nsr/nwu014 (2014).
- 94 Hutvagner, G. & Simard, M. J. Argonaute proteins: key players in RNA silencing. *Nat Rev Mol Cell Biol* **9**, 22-32, doi:10.1038/nrm2321 (2008).
- 95 Murakami, R., Sumiyoshi, T., Negishi, L. & Siomi, M. C. DEAD-box polypeptide 43 facilitates piRNA amplification by actively liberating RNA from Ago3-piRISC. *EMBO Rep* **22**, e51313, doi:10.15252/embr.202051313 (2021).
- 96 Tu, Y. T. & Barrientos, A. The Human Mitochondrial DEAD-Box Protein DDX28 Resides in RNA Granules and Functions in Mitoribosome Assembly. *Cell Rep* **10**, 854-864, doi:10.1016/j.celrep.2015.01.033 (2015).
- 97 Schmid, M. & Jensen, T. H. The Nuclear RNA Exosome and Its Cofactors. *Adv Exp Med Biol* **1203**, 113-132, doi:10.1007/978-3-030-31434-7_4 (2019).
- 98 Jia, H., Wang, X., Anderson, J. T. & Jankowsky, E. RNA unwinding by the Trf4/Air2/Mtr4 polyadenylation (TRAMP) complex. *Proc Natl Acad Sci U S A* **109**, 7292-7297, doi:10.1073/pnas.1201085109 (2012).
- 99 Cordin, O. & Beggs, J. D. RNA helicases in splicing. *RNA Biol* **10**, 83-95, doi:10.4161/rna.22547 (2013).
- 100 Le Hir, H., Sauliere, J. & Wang, Z. The exon junction complex as a node of post-transcriptional networks. *Nat Rev Mol Cell Biol* **17**, 41-54, doi:10.1038/nrm.2015.7 (2016).
- 101 Sloan, K. E. & Bohnsack, M. T. Unravelling the Mechanisms of RNA Helicase Regulation. *Trends Biochem Sci* **43**, 237-250, doi:10.1016/j.tibs.2018.02.001 (2018).
- 102 Heining, A. U. *et al.* Protein cofactor competition regulates the action of a multifunctional RNA helicase in different pathways. *RNA Biol* **13**, 320-330, doi:10.1080/15476286.2016.1142038 (2016).
- 103 Young, C. & Karbstein, K. Analysis of cofactor effects on RNA helicases. *Methods Enzymol* **511**, 213-237, doi:10.1016/B978-0-12-396546-2.00010-3 (2012).
- 104 Rogers, G. W., Jr., Richter, N. J. & Merrick, W. C. Biochemical and kinetic characterization of the RNA helicase activity of eukaryotic initiation factor 4A. *J Biol Chem* **274**, 12236-12244, doi:10.1074/jbc.274.18.12236 (1999).

- 105 Korneeva, N. L., First, E. A., Benoit, C. A. & Rhoads, R. E. Interaction between the NH₂-terminal domain of eIF4A and the central domain of eIF4G modulates RNA-stimulated ATPase activity. *J Biol Chem* **280**, 1872-1881, doi:10.1074/jbc.M406168200 (2005).
- 106 Rogers, G. W., Jr., Richter, N. J., Lima, W. F. & Merrick, W. C. Modulation of the helicase activity of eIF4A by eIF4B, eIF4H, and eIF4F. *J Biol Chem* **276**, 30914-30922, doi:10.1074/jbc.M100157200 (2001).
- 107 Richter, N. J., Rogers, G. W., Jr., Hensold, J. O. & Merrick, W. C. Further biochemical and kinetic characterization of human eukaryotic initiation factor 4H. *J Biol Chem* **274**, 35415-35424, doi:10.1074/jbc.274.50.35415 (1999).
- 108 Abramson, R. D., Dever, T. E. & Merrick, W. C. Biochemical evidence supporting a mechanism for cap-independent and internal initiation of eukaryotic mRNA. *J Biol Chem* **263**, 6016-6019 (1988).
- 109 Schutz, P. *et al.* Crystal structure of the yeast eIF4A-eIF4G complex: an RNA-helicase controlled by protein-protein interactions. *Proc Natl Acad Sci U S A* **105**, 9564-9569, doi:10.1073/pnas.0800418105 (2008).
- 110 Hilbert, M., Kebbel, F., Gubaev, A. & Klostermeier, D. eIF4G stimulates the activity of the DEAD box protein eIF4A by a conformational guidance mechanism. *Nucleic Acids Res* **39**, 2260-2270, doi:10.1093/nar/gkq1127 (2011).
- 111 Pause, A., Methot, N., Svitkin, Y., Merrick, W. C. & Sonenberg, N. Dominant negative mutants of mammalian translation initiation factor eIF-4A define a critical role for eIF-4F in cap-dependent and cap-independent initiation of translation. *EMBO J* **13**, 1205-1215, doi:10.1002/j.1460-2075.1994.tb06370.x (1994).
- 112 Sen, N. D., Zhou, F., Harris, M. S., Ingolia, N. T. & Hinnebusch, A. G. eIF4B stimulates translation of long mRNAs with structured 5' UTRs and low closed-loop potential but weak dependence on eIF4G. *Proc Natl Acad Sci U S A* **113**, 10464-10472, doi:10.1073/pnas.1612398113 (2016).
- 113 Yang, H. S. *et al.* The transformation suppressor Pdc4 is a novel eukaryotic translation initiation factor 4A binding protein that inhibits translation. *Mol Cell Biol* **23**, 26-37, doi:10.1128/MCB.23.1.26-37.2003 (2003).
- 114 Chang, J. H. *et al.* Crystal structure of the eIF4A-PDCD4 complex. *Proc Natl Acad Sci U S A* **106**, 3148-3153, doi:10.1073/pnas.0808275106 (2009).
- 115 LaRonde-LeBlanc, N., Santhanam, A. N., Baker, A. R., Wlodawer, A. & Colburn, N. H. Structural basis for inhibition of translation by the tumor suppressor Pdc4. *Mol Cell Biol* **27**, 147-156, doi:10.1128/MCB.00867-06 (2007).

- 116 Gao, Z. *et al.* Coupling between the DEAD-box RNA helicases Ded1p and eIF4A. *Elife* **5**, doi:10.7554/eLife.16408 (2016).
- 117 Senissar, M. *et al.* The DEAD-box helicase Ded1 from yeast is an mRNP cap-associated protein that shuttles between the cytoplasm and nucleus. *Nucleic Acids Res* **42**, 10005-10022, doi:10.1093/nar/gku584 (2014).
- 118 Marsden, S., Nardelli, M., Linder, P. & McCarthy, J. E. Unwinding single RNA molecules using helicases involved in eukaryotic translation initiation. *J Mol Biol* **361**, 327-335, doi:10.1016/j.jmb.2006.06.016 (2006).
- 119 Bolger, T. A. & Wenthe, S. R. Gle1 is a multifunctional DEAD-box protein regulator that modulates Ded1 in translation initiation. *J Biol Chem* **286**, 39750-39759, doi:10.1074/jbc.M111.299321 (2011).
- 120 Aryanpur, P. P. *et al.* Gle1 Regulates RNA Binding of the DEAD-Box Helicase Ded1 in Its Complex Role in Translation Initiation. *Mol Cell Biol* **37**, doi:10.1128/MCB.00139-17 (2017).
- 121 Alcazar-Roman, A. R., Tran, E. J., Guo, S. & Wenthe, S. R. Inositol hexakisphosphate and Gle1 activate the DEAD-box protein Dbp5 for nuclear mRNA export. *Nat Cell Biol* **8**, 711-716, doi:10.1038/ncb1427 (2006).
- 122 Weirich, C. S. *et al.* Activation of the DExD/H-box protein Dbp5 by the nuclear-pore protein Gle1 and its coactivator InsP6 is required for mRNA export. *Nat Cell Biol* **8**, 668-676, doi:10.1038/ncb1424 (2006).
- 123 Correction to 'The nucleoporin Gle1 activates DEAD-box protein 5 (Dbp5) by promoting ATP binding and accelerating rate limiting phosphate release'. *Nucleic Acids Res* **50**, 4197, doi:10.1093/nar/gkac221 (2022).
- 124 Folkmann, A. W., Noble, K. N., Cole, C. N. & Wenthe, S. R. Dbp5, Gle1-IP6 and Nup159: a working model for mRNP export. *Nucleus* **2**, 540-548, doi:10.4161/nucl.2.6.17881 (2011).
- 125 Montpetit, B., Seeliger, M. A. & Weis, K. Analysis of DEAD-box proteins in mRNA export. *Methods Enzymol* **511**, 239-254, doi:10.1016/B978-0-12-396546-2.00011-5 (2012).
- 126 Schmitt, C. *et al.* Dbp5, a DEAD-box protein required for mRNA export, is recruited to the cytoplasmic fibrils of nuclear pore complex via a conserved interaction with CAN/Nup159p. *EMBO J* **18**, 4332-4347, doi:10.1093/emboj/18.15.4332 (1999).
- 127 Weirich, C. S., Erzberger, J. P., Berger, J. M. & Weis, K. The N-terminal domain of Nup159 forms a beta-propeller that functions in mRNA export by tethering the helicase Dbp5 to the nuclear pore. *Mol Cell* **16**, 749-760, doi:10.1016/j.molcel.2004.10.032 (2004).
- 128 Ma, W. K., Cloutier, S. C. & Tran, E. J. The DEAD-box protein Dbp2 functions with the RNA-binding protein Yra1 to promote mRNP assembly. *J Mol Biol* **425**, 3824-3838, doi:10.1016/j.jmb.2013.05.016 (2013).

- 129 Jensen, T. H., Dower, K., Libri, D. & Rosbash, M. Early formation of mRNP: license for export or quality control? *Mol Cell* **11**, 1129-1138, doi:10.1016/s1097-2765(03)00191-6 (2003).
- 130 Ma, W. K. *et al.* Recruitment, Duplex Unwinding and Protein-Mediated Inhibition of the Dead-Box RNA Helicase Dbp2 at Actively Transcribed Chromatin. *J Mol Biol* **428**, 1091-1106, doi:10.1016/j.jmb.2016.02.005 (2016).
- 131 Woodward, L. A., Mabin, J. W., Gangras, P. & Singh, G. The exon junction complex: a lifelong guardian of mRNA fate. *Wiley Interdiscip Rev RNA* **8**, doi:10.1002/wrna.1411 (2017).
- 132 Ballut, L. *et al.* The exon junction core complex is locked onto RNA by inhibition of eIF4AIII ATPase activity. *Nat Struct Mol Biol* **12**, 861-869, doi:10.1038/nsmb990 (2005).
- 133 Nielsen, K. H. *et al.* Mechanism of ATP turnover inhibition in the EJC. *RNA* **15**, 67-75, doi:10.1261/rna.1283109 (2009).
- 134 Granneman, S. *et al.* The nucleolar protein Esf2 interacts directly with the DExD/H box RNA helicase, Dbp8, to stimulate ATP hydrolysis. *Nucleic Acids Res* **34**, 3189-3199, doi:10.1093/nar/gkl419 (2006).
- 135 Jeske, M., Muller, C. W. & Ephrussi, A. The LOTUS domain is a conserved DEAD-box RNA helicase regulator essential for the recruitment of Vasa to the germ plasm and nuage. *Genes Dev* **31**, 939-952, doi:10.1101/gad.297051.117 (2017).
- 136 Cipriani, P. G. *et al.* Novel LOTUS-domain proteins are organizational hubs that recruit *C. elegans* Vasa to germ granules. *Elife* **10**, doi:10.7554/eLife.60833 (2021).
- 137 Kubikova, J., Reinig, R., Salgania, H. K. & Jeske, M. LOTUS-domain proteins - developmental effectors from a molecular perspective. *Biol Chem* **402**, 7-23, doi:10.1515/hsz-2020-0270 (2020).
- 138 Favaro, F. P. *et al.* A noncoding expansion in EIF4A3 causes Richieri-Costa-Pereira syndrome, a craniofacial disorder associated with limb defects. *Am J Hum Genet* **94**, 120-128, doi:10.1016/j.ajhg.2013.11.020 (2014).
- 139 Bertola, D. R. *et al.* Richieri-Costa-Pereira syndrome: Expanding its phenotypic and genotypic spectrum. *Clin Genet* **93**, 800-811, doi:10.1111/cge.13169 (2018).
- 140 Shamseldin, H. E. *et al.* Mutations in DDX59 implicate RNA helicase in the pathogenesis of orofacioidigital syndrome. *Am J Hum Genet* **93**, 555-560, doi:10.1016/j.ajhg.2013.07.012 (2013).
- 141 Balak, C. *et al.* Rare De Novo Missense Variants in RNA Helicase DDX6 Cause Intellectual Disability and Dysmorphic Features and Lead to P-

- Body Defects and RNA Dysregulation. *Am J Hum Genet* **105**, 509-525, doi:10.1016/j.ajhg.2019.07.010 (2019).
- 142 Paine, I. *et al.* Paralog Studies Augment Gene Discovery: DDX and DHX Genes. *Am J Hum Genet* **105**, 302-316, doi:10.1016/j.ajhg.2019.06.001 (2019).
- 143 Snijders Blok, L. *et al.* Mutations in DDX3X Are a Common Cause of Unexplained Intellectual Disability with Gender-Specific Effects on Wnt Signaling. *Am J Hum Genet* **97**, 343-352, doi:10.1016/j.ajhg.2015.07.004 (2015).
- 144 Burns, W. *et al.* Syndromic neurodevelopmental disorder associated with de novo variants in DDX23. *Am J Med Genet A* **185**, 2863-2872, doi:10.1002/ajmg.a.62359 (2021).
- 145 Toriello, H. V. *et al.* Toriello-Carey syndrome: delineation and review. *Am J Med Genet A* **123A**, 84-90, doi:10.1002/ajmg.a.20493 (2003).
- 146 Dikow, N. *et al.* DDX3X mutations in two girls with a phenotype overlapping Toriello-Carey syndrome. *Am J Med Genet A* **173**, 1369-1373, doi:10.1002/ajmg.a.38164 (2017).
- 147 Jones, K. *et al.* Reduction of toxic RNAs in myotonic dystrophies type 1 and type 2 by the RNA helicase p68/DDX5. *Proc Natl Acad Sci U S A* **112**, 8041-8045, doi:10.1073/pnas.1422273112 (2015).
- 148 Zhang, L. *et al.* RNA helicase p68 inhibits the transcription and post-transcription of Pkd1 in ADPKD. *Theranostics* **10**, 8281-8297, doi:10.7150/thno.47315 (2020).
- 149 Laurent, F. X. *et al.* New function for the RNA helicase p68/DDX5 as a modifier of MBNL1 activity on expanded CUG repeats. *Nucleic Acids Res* **40**, 3159-3171, doi:10.1093/nar/gkr1228 (2012).
- 150 Alberti, S. & Hyman, A. A. Biomolecular condensates at the nexus of cellular stress, protein aggregation disease and ageing. *Nat Rev Mol Cell Biol* **22**, 196-213, doi:10.1038/s41580-020-00326-6 (2021).
- 151 Roden, C. & Gladfelter, A. S. RNA contributions to the form and function of biomolecular condensates. *Nat Rev Mol Cell Biol* **22**, 183-195, doi:10.1038/s41580-020-0264-6 (2021).
- 152 Banani, S. F., Lee, H. O., Hyman, A. A. & Rosen, M. K. Biomolecular condensates: organizers of cellular biochemistry. *Nat Rev Mol Cell Biol* **18**, 285-298, doi:10.1038/nrm.2017.7 (2017).
- 153 Mao, Y. S., Zhang, B. & Spector, D. L. Biogenesis and function of nuclear bodies. *Trends Genet* **27**, 295-306, doi:10.1016/j.tig.2011.05.006 (2011).
- 154 Lafontaine, D. L. J., Riback, J. A., Bascetin, R. & Brangwynne, C. P. The nucleolus as a multiphase liquid condensate. *Nat Rev Mol Cell Biol* **22**, 165-182, doi:10.1038/s41580-020-0272-6 (2021).

- 155 Caragine, C. M., Haley, S. C. & Zidovska, A. Nucleolar dynamics and interactions with nucleoplasm in living cells. *Elife* **8**, doi:10.7554/eLife.47533 (2019).
- 156 Feric, M. *et al.* Coexisting Liquid Phases Underlie Nucleolar Subcompartments. *Cell* **165**, 1686-1697, doi:10.1016/j.cell.2016.04.047 (2016).
- 157 Lafontaine, D. L. J. Birth of Nucleolar Compartments: Phase Separation-Driven Ribosomal RNA Sorting and Processing. *Mol Cell* **76**, 694-696, doi:10.1016/j.molcel.2019.11.015 (2019).
- 158 Guillen-Chable, F., Bayona, A., Rodriguez-Zapata, L. C. & Castano, E. Phase Separation of Intrinsically Disordered Nucleolar Proteins Relate to Localization and Function. *Int J Mol Sci* **22**, doi:10.3390/ijms222313095 (2021).
- 159 Bergstrand, S., O'Brien, E. M. & Farnebo, M. The Cajal Body Protein WRAP53beta Prepares the Scene for Repair of DNA Double-Strand Breaks by Regulating Local Ubiquitination. *Front Mol Biosci* **6**, 51, doi:10.3389/fmolb.2019.00051 (2019).
- 160 Stanek, D. & Fox, A. H. Nuclear bodies: news insights into structure and function. *Curr Opin Cell Biol* **46**, 94-101, doi:10.1016/j.ceb.2017.05.001 (2017).
- 161 Trinkle-Mulcahy, L. & Sleeman, J. E. The Cajal body and the nucleolus: "In a relationship" or "It's complicated"? *RNA Biol* **14**, 739-751, doi:10.1080/15476286.2016.1236169 (2017).
- 162 Fox, A. H., Nakagawa, S., Hirose, T. & Bond, C. S. Paraspeckles: Where Long Noncoding RNA Meets Phase Separation. *Trends Biochem Sci* **43**, 124-135, doi:10.1016/j.tibs.2017.12.001 (2018).
- 163 Spector, D. L. & Lamond, A. I. Nuclear speckles. *Cold Spring Harb Perspect Biol* **3**, doi:10.1101/cshperspect.a000646 (2011).
- 164 Galganski, L., Urbanek, M. O. & Krzyzosiak, W. J. Nuclear speckles: molecular organization, biological function and role in disease. *Nucleic Acids Res* **45**, 10350-10368, doi:10.1093/nar/gkx759 (2017).
- 165 Seif, E. *et al.* Phase separation by the polyhomeotic sterile alpha motif compartmentalizes Polycomb Group proteins and enhances their activity. *Nat Commun* **11**, 5609, doi:10.1038/s41467-020-19435-z (2020).
- 166 Tatavosian, R. *et al.* Nuclear condensates of the Polycomb protein chromobox 2 (CBX2) assemble through phase separation. *J Biol Chem* **294**, 1451-1463, doi:10.1074/jbc.RA118.006620 (2019).
- 167 Plys, A. J. *et al.* Phase separation of Polycomb-repressive complex 1 is governed by a charged disordered region of CBX2. *Genes Dev* **33**, 799-813, doi:10.1101/gad.326488.119 (2019).

- 168 Corpet, A. *et al.* PML nuclear bodies and chromatin dynamics: catch me if you can! *Nucleic Acids Res* **48**, 11890-11912, doi:10.1093/nar/gkaa828 (2020).
- 169 Lallemand-Breitenbach, V. & de The, H. PML nuclear bodies. *Cold Spring Harb Perspect Biol* **2**, a000661, doi:10.1101/cshperspect.a000661 (2010).
- 170 Fijen, C. & Rothenberg, E. The evolving complexity of DNA damage foci: RNA, condensates and chromatin in DNA double-strand break repair. *DNA Repair (Amst)* **105**, 103170, doi:10.1016/j.dnarep.2021.103170 (2021).
- 171 Sanulli, S. *et al.* HP1 reshapes nucleosome core to promote phase separation of heterochromatin. *Nature* **575**, 390-394, doi:10.1038/s41586-019-1669-2 (2019).
- 172 Larson, A. G. & Narlikar, G. J. The Role of Phase Separation in Heterochromatin Formation, Function, and Regulation. *Biochemistry* **57**, 2540-2548, doi:10.1021/acs.biochem.8b00401 (2018).
- 173 Keenen, M. M. *et al.* HP1 proteins compact DNA into mechanically and positionally stable phase separated domains. *Elife* **10**, doi:10.7554/eLife.64563 (2021).
- 174 Penagos-Puig, A. & Furlan-Magaril, M. Heterochromatin as an Important Driver of Genome Organization. *Front Cell Dev Biol* **8**, 579137, doi:10.3389/fcell.2020.579137 (2020).
- 175 Guthmann, M., Burton, A. & Torres-Padilla, M. E. Expression and phase separation potential of heterochromatin proteins during early mouse development. *EMBO Rep* **20**, e47952, doi:10.15252/embr.201947952 (2019).
- 176 Pessina, F. *et al.* Functional transcription promoters at DNA double-strand breaks mediate RNA-driven phase separation of damage-response factors. *Nat Cell Biol* **21**, 1286-1299, doi:10.1038/s41556-019-0392-4 (2019).
- 177 Kilic, S. *et al.* Phase separation of 53BP1 determines liquid-like behavior of DNA repair compartments. *EMBO J* **38**, e101379, doi:10.15252/emboj.2018101379 (2019).
- 178 Oshidari, R. *et al.* DNA repair by Rad52 liquid droplets. *Nat Commun* **11**, 695, doi:10.1038/s41467-020-14546-z (2020).
- 179 Cho, W. K. *et al.* Mediator and RNA polymerase II clusters associate in transcription-dependent condensates. *Science* **361**, 412-415, doi:10.1126/science.aar4199 (2018).
- 180 Boehning, M. *et al.* RNA polymerase II clustering through carboxy-terminal domain phase separation. *Nat Struct Mol Biol* **25**, 833-840, doi:10.1038/s41594-018-0112-y (2018).

- 181 Boija, A. *et al.* Transcription Factors Activate Genes through the Phase-Separation Capacity of Their Activation Domains. *Cell* **175**, 1842-1855 e1816, doi:10.1016/j.cell.2018.10.042 (2018).
- 182 Lu, H. *et al.* Phase-separation mechanism for C-terminal hyperphosphorylation of RNA polymerase II. *Nature* **558**, 318-323, doi:10.1038/s41586-018-0174-3 (2018).
- 183 Sabari, B. R. *et al.* Coactivator condensation at super-enhancers links phase separation and gene control. *Science* **361**, doi:10.1126/science.aar3958 (2018).
- 184 Phillips, C. M. & Updike, D. L. Germ granules and gene regulation in the *Caenorhabditis elegans* germline. *Genetics* **220**, doi:10.1093/genetics/iyab195 (2022).
- 185 Mukherjee, N. & Mukherjee, C. Germ cell ribonucleoprotein granules in different clades of life: From insects to mammals. *Wiley Interdiscip Rev RNA* **12**, e1642, doi:10.1002/wrna.1642 (2021).
- 186 Ouyang, J. P. T. & Seydoux, G. Nuage condensates: accelerators or circuit breakers for sRNA silencing pathways? *RNA* **28**, 58-66, doi:10.1261/rna.079003.121 (2022).
- 187 Voronina, E., Seydoux, G., Sassone-Corsi, P. & Nagamori, I. RNA granules in germ cells. *Cold Spring Harb Perspect Biol* **3**, doi:10.1101/cshperspect.a002774 (2011).
- 188 Anbazhagan, R., Kavarthapu, R., Coon, S. L. & Dufau, M. L. Role of Phosphorylated Gonadotropin-Regulated Testicular RNA Helicase (GRTH/DDX25) in the Regulation of Germ Cell Specific mRNAs in Chromatoid Bodies During Spermatogenesis. *Front Cell Dev Biol* **8**, 580019, doi:10.3389/fcell.2020.580019 (2020).
- 189 Bauer, K. E., Kiebler, M. A. & Segura, I. Visualizing RNA granule transport and translation in living neurons. *Methods* **126**, 177-185, doi:10.1016/j.ymeth.2017.06.013 (2017).
- 190 Liao, Y. C. *et al.* RNA Granules Hitchhike on Lysosomes for Long-Distance Transport, Using Annexin A11 as a Molecular Tether. *Cell* **179**, 147-164 e120, doi:10.1016/j.cell.2019.08.050 (2019).
- 191 Pushpalatha, K. V. & Besse, F. Local Translation in Axons: When Membraneless RNP Granules Meet Membrane-Bound Organelles. *Front Mol Biosci* **6**, 129, doi:10.3389/fmolb.2019.00129 (2019).
- 192 Luo, Y., Na, Z. & Slavoff, S. A. P-Bodies: Composition, Properties, and Functions. *Biochemistry* **57**, 2424-2431, doi:10.1021/acs.biochem.7b01162 (2018).
- 193 Xing, W., Muhlrad, D., Parker, R. & Rosen, M. K. A quantitative inventory of yeast P body proteins reveals principles of composition and specificity. *Elife* **9**, doi:10.7554/eLife.56525 (2020).

- 194 Tibble, R. W., Depaix, A., Kowalska, J., Jemielity, J. & Gross, J. D. Biomolecular condensates amplify mRNA decapping by biasing enzyme conformation. *Nat Chem Biol* **17**, 615-623, doi:10.1038/s41589-021-00774-x (2021).
- 195 Schutz, S., Noldeke, E. R. & Sprangers, R. A synergistic network of interactions promotes the formation of in vitro processing bodies and protects mRNA against decapping. *Nucleic Acids Res* **45**, 6911-6922, doi:10.1093/nar/gkx353 (2017).
- 196 Riggs, C. L., Kedersha, N., Ivanov, P. & Anderson, P. Mammalian stress granules and P bodies at a glance. *J Cell Sci* **133**, doi:10.1242/jcs.242487 (2020).
- 197 Ivanov, P., Kedersha, N. & Anderson, P. Stress Granules and Processing Bodies in Translational Control. *Cold Spring Harb Perspect Biol* **11**, doi:10.1101/cshperspect.a032813 (2019).
- 198 Markmiller, S. *et al.* Context-Dependent and Disease-Specific Diversity in Protein Interactions within Stress Granules. *Cell* **172**, 590-604 e513, doi:10.1016/j.cell.2017.12.032 (2018).
- 199 Van Treeck, B. & Parker, R. Principles of Stress Granules Revealed by Imaging Approaches. *Cold Spring Harb Perspect Biol* **11**, doi:10.1101/cshperspect.a033068 (2019).
- 200 Mehta, S. & Zhang, J. Liquid-liquid phase separation drives cellular function and dysfunction in cancer. *Nat Rev Cancer* **22**, 239-252, doi:10.1038/s41568-022-00444-7 (2022).
- 201 Wiedner, H. J. & Giudice, J. It's not just a phase: function and characteristics of RNA-binding proteins in phase separation. *Nat Struct Mol Biol* **28**, 465-473, doi:10.1038/s41594-021-00601-w (2021).
- 202 Xiao, Q., McAtee, C. K. & Su, X. Phase separation in immune signalling. *Nat Rev Immunol* **22**, 188-199, doi:10.1038/s41577-021-00572-5 (2022).
- 203 Du, M. & Chen, Z. J. DNA-induced liquid phase condensation of cGAS activates innate immune signaling. *Science* **361**, 704-709, doi:10.1126/science.aat1022 (2018).
- 204 Xie, W. *et al.* Human cGAS catalytic domain has an additional DNA-binding interface that enhances enzymatic activity and liquid-phase condensation. *Proc Natl Acad Sci U S A* **116**, 11946-11955, doi:10.1073/pnas.1905013116 (2019).
- 205 Zhou, W., Mohr, L., Maciejowski, J. & Kranzusch, P. J. cGAS phase separation inhibits TREX1-mediated DNA degradation and enhances cytosolic DNA sensing. *Mol Cell* **81**, 739-755 e737, doi:10.1016/j.molcel.2021.01.024 (2021).

- 206 Campos-Melo, D., Hawley, Z. C. E., Droppelmann, C. A. & Strong, M. J. The Integral Role of RNA in Stress Granule Formation and Function. *Front Cell Dev Biol* **9**, 621779, doi:10.3389/fcell.2021.621779 (2021).
- 207 McCormick, C. & Khapersky, D. A. Translation inhibition and stress granules in the antiviral immune response. *Nat Rev Immunol* **17**, 647-660, doi:10.1038/nri.2017.63 (2017).
- 208 Babu, M. M. The contribution of intrinsically disordered regions to protein function, cellular complexity, and human disease. *Biochem Soc Trans* **44**, 1185-1200, doi:10.1042/BST20160172 (2016).
- 209 Banerjee, P. R., Milin, A. N., Moosa, M. M., Onuchic, P. L. & Deniz, A. A. Reentrant Phase Transition Drives Dynamic Substructure Formation in Ribonucleoprotein Droplets. *Angew Chem Int Ed Engl* **56**, 11354-11359, doi:10.1002/anie.201703191 (2017).
- 210 Hondele, M. *et al.* DEAD-box ATPases are global regulators of phase-separated organelles. *Nature* **573**, 144-148, doi:10.1038/s41586-019-1502-y (2019).
- 211 Tauber, D. *et al.* Modulation of RNA Condensation by the DEAD-Box Protein eIF4A. *Cell* **180**, 411-426 e416, doi:10.1016/j.cell.2019.12.031 (2020).
- 212 Hooper, C. & Hilliker, A. Packing them up and dusting them off: RNA helicases and mRNA storage. *Biochim Biophys Acta* **1829**, 824-834, doi:10.1016/j.bbagr.2013.03.008 (2013).
- 213 Sachdev, R. *et al.* Pat1 promotes processing body assembly by enhancing the phase separation of the DEAD-box ATPase Dhh1 and RNA. *Elife* **8**, doi:10.7554/eLife.41415 (2019).
- 214 Mugler, C. F. *et al.* ATPase activity of the DEAD-box protein Dhh1 controls processing body formation. *Elife* **5**, doi:10.7554/eLife.18746 (2016).
- 215 Hubstenberger, A., Noble, S. L., Cameron, C. & Evans, T. C. Translation repressors, an RNA helicase, and developmental cues control RNP phase transitions during early development. *Dev Cell* **27**, 161-173, doi:10.1016/j.devcel.2013.09.024 (2013).
- 216 Chalupnikova, K. *et al.* Recruitment of the RNA helicase RHAU to stress granules via a unique RNA-binding domain. *J Biol Chem* **283**, 35186-35198, doi:10.1074/jbc.M804857200 (2008).
- 217 Iserman, C. *et al.* Condensation of Ded1p Promotes a Translational Switch from Housekeeping to Stress Protein Production. *Cell* **181**, 818-831 e819, doi:10.1016/j.cell.2020.04.009 (2020).
- 218 Shen, H. *et al.* Sexually dimorphic RNA helicases DDX3X and DDX3Y differentially regulate RNA metabolism through phase separation. *Mol Cell*, doi:10.1016/j.molcel.2022.04.022 (2022).

- 219 Hilliker, A., Gao, Z., Jankowsky, E. & Parker, R. The DEAD-box protein Ded1 modulates translation by the formation and resolution of an eIF4F-mRNA complex. *Mol Cell* **43**, 962-972, doi:10.1016/j.molcel.2011.08.008 (2011).
- 220 Shih, J. W. *et al.* Critical roles of RNA helicase DDX3 and its interactions with eIF4E/PABP1 in stress granule assembly and stress response. *Biochem J* **441**, 119-129, doi:10.1042/BJ20110739 (2012).
- 221 Samir, P. *et al.* DDX3X acts as a live-or-die checkpoint in stressed cells by regulating NLRP3 inflammasome. *Nature* **573**, 590-594, doi:10.1038/s41586-019-1551-2 (2019).
- 222 Kizhakeyil, A. *et al.* DDX3X loss is an adverse prognostic marker in diffuse large B-cell lymphoma and is associated with chemoresistance in aggressive non-Hodgkin lymphoma subtypes. *Mol Cancer* **20**, 134, doi:10.1186/s12943-021-01437-0 (2021).
- 223 Phung, B. *et al.* The X-Linked DDX3X RNA Helicase Dictates Translation Reprogramming and Metastasis in Melanoma. *Cell Rep* **27**, 3573-3586 e3577, doi:10.1016/j.celrep.2019.05.069 (2019).
- 224 Lennox, A. L. *et al.* Pathogenic DDX3X Mutations Impair RNA Metabolism and Neurogenesis during Fetal Cortical Development. *Neuron* **106**, 404-420 e408, doi:10.1016/j.neuron.2020.01.042 (2020).
- 225 Dodson, A. E. & Kennedy, S. Phase Separation in Germ Cells and Development. *Dev Cell* **55**, 4-17, doi:10.1016/j.devcel.2020.09.004 (2020).
- 226 Wan, G. *et al.* Spatiotemporal regulation of liquid-like condensates in epigenetic inheritance. *Nature* **557**, 679-683, doi:10.1038/s41586-018-0132-0 (2018).
- 227 Ishidate, T. *et al.* ZNFX-1 Functions within Perinuclear Nuage to Balance Epigenetic Signals. *Mol Cell* **70**, 639-649 e636, doi:10.1016/j.molcel.2018.04.009 (2018).
- 228 Xu, C., Cao, Y. & Bao, J. Building RNA-protein germ granules: insights from the multifaceted functions of DEAD-box helicase Vasa/Ddx4 in germline development. *Cell Mol Life Sci* **79**, 4, doi:10.1007/s00018-021-04069-1 (2021).
- 229 Nott, T. J. *et al.* Phase transition of a disordered nuage protein generates environmentally responsive membraneless organelles. *Mol Cell* **57**, 936-947, doi:10.1016/j.molcel.2015.01.013 (2015).
- 230 Floor, S. N., Condon, K. J., Sharma, D., Jankowsky, E. & Doudna, J. A. Autoinhibitory Interdomain Interactions and Subfamily-specific Extensions Redefine the Catalytic Core of the Human DEAD-box Protein DDX3. *J Biol Chem* **291**, 2412-2421, doi:10.1074/jbc.M115.700625 (2016).

- 231 Piovesan, D. *et al.* MobiDB 3.0: more annotations for intrinsic disorder, conformational diversity and interactions in proteins. *Nucleic Acids Res* **46**, D471-D476, doi:10.1093/nar/gkx1071 (2018).
- 232 Yang, Q., Del Campo, M., Lambowitz, A. M. & Jankowsky, E. DEAD-box proteins unwind duplexes by local strand separation. *Mol Cell* **28**, 253-263, doi:10.1016/j.molcel.2007.08.016 (2007).
- 233 Epling, L. B., Grace, C. R., Lowe, B. R., Partridge, J. F. & Enemark, E. J. Cancer-associated mutants of RNA helicase DDX3X are defective in RNA-stimulated ATP hydrolysis. *J Mol Biol* **427**, 1779-1796, doi:10.1016/j.jmb.2015.02.015 (2015).
- 234 Sengoku, T., Nureki, O., Nakamura, A., Kobayashi, S. & Yokoyama, S. Structural basis for RNA unwinding by the DEAD-box protein Drosophila Vasa. *Cell* **125**, 287-300, doi:10.1016/j.cell.2006.01.054 (2006).
- 235 Wang, T. *et al.* Identification and characterization of essential genes in the human genome. *Science* **350**, 1096-1101, doi:10.1126/science.aac7041 (2015).
- 236 Szappanos, D. *et al.* The RNA helicase DDX3X is an essential mediator of innate antimicrobial immunity. *PLoS Pathog* **14**, e1007397, doi:10.1371/journal.ppat.1007397 (2018).
- 237 Li, Q. *et al.* DDX3X regulates cell survival and cell cycle during mouse early embryonic development. *J Biomed Res* **28**, 282-291, doi:10.7555/JBR.27.20130047 (2014).
- 238 Chen, C. Y. *et al.* Targeted inactivation of murine Ddx3x: essential roles of Ddx3x in placentation and embryogenesis. *Hum Mol Genet* **25**, 2905-2922, doi:10.1093/hmg/ddw143 (2016).
- 239 Venkataramanan, S., Gadek, M., Calviello, L., Wilkins, K. & Floor, S. N. DDX3X and DDX3Y are redundant in protein synthesis. *RNA* **27**, 1577-1588, doi:10.1261/rna.078926.121 (2021).
- 240 Patmore, D. M. *et al.* DDX3X Suppresses the Susceptibility of Hindbrain Lineages to Medulloblastoma. *Dev Cell* **54**, 455-470 e455, doi:10.1016/j.devcel.2020.05.027 (2020).
- 241 Hoye, M. L. *et al.* Aberrant cortical development is driven by impaired cell cycle and translational control in a DDX3X syndrome model. *Elife* **11**, doi:10.7554/eLife.78203 (2022).
- 242 Saikruang, W. *et al.* The RNA helicase DDX3 promotes IFNB transcription via enhancing IRF-3/p300 holocomplex binding to the IFNB promoter. *Sci Rep* **12**, 3967, doi:10.1038/s41598-022-07876-z (2022).
- 243 Gartel, A. L. p21(WAF1/CIP1) and cancer: a shifting paradigm? *Biofactors* **35**, 161-164, doi:10.1002/biof.26 (2009).
- 244 Chao, C. H. *et al.* DDX3, a DEAD box RNA helicase with tumor growth-suppressive property and transcriptional regulation activity of the

- p21waf1/cip1 promoter, is a candidate tumor suppressor. *Cancer Res* **66**, 6579-6588, doi:10.1158/0008-5472.CAN-05-2415 (2006).
- 245 Vella, P., Barozzi, I., Cuomo, A., Bonaldi, T. & Pasini, D. Yin Yang 1 extends the Myc-related transcription factors network in embryonic stem cells. *Nucleic Acids Res* **40**, 3403-3418, doi:10.1093/nar/gkr1290 (2012).
- 246 Clevers, H. Wnt/beta-catenin signaling in development and disease. *Cell* **127**, 469-480, doi:10.1016/j.cell.2006.10.018 (2006).
- 247 Yang, F. *et al.* Cis-Acting circ-CTNNB1 Promotes beta-Catenin Signaling and Cancer Progression via DDX3-Mediated Transactivation of YY1. *Cancer Res* **79**, 557-571, doi:10.1158/0008-5472.CAN-18-1559 (2019).
- 248 Zhao, L., Mao, Y., Zhao, Y. & He, Y. DDX3X promotes the biogenesis of a subset of miRNAs and the potential roles they played in cancer development. *Sci Rep* **6**, 32739, doi:10.1038/srep32739 (2016).
- 249 Han, J. *et al.* The Drosha-DGCR8 complex in primary microRNA processing. *Genes Dev* **18**, 3016-3027, doi:10.1101/gad.1262504 (2004).
- 250 Nussbacher, J. K. & Yeo, G. W. Systematic Discovery of RNA Binding Proteins that Regulate MicroRNA Levels. *Mol Cell* **69**, 1005-1016 e1007, doi:10.1016/j.molcel.2018.02.012 (2018).
- 251 Li, H. K. *et al.* DDX3 Represses Stemness by Epigenetically Modulating Tumor-suppressive miRNAs in Hepatocellular Carcinoma. *Sci Rep* **6**, 28637, doi:10.1038/srep28637 (2016).
- 252 Topisirovic, I. *et al.* Molecular dissection of the eukaryotic initiation factor 4E (eIF4E) export-competent RNP. *EMBO J* **28**, 1087-1098, doi:10.1038/emboj.2009.53 (2009).
- 253 Lai, M. C., Lee, Y. H. & Tarn, W. Y. The DEAD-box RNA helicase DDX3 associates with export messenger ribonucleoproteins as well as tip-associated protein and participates in translational control. *Mol Biol Cell* **19**, 3847-3858, doi:10.1091/mbc.E07-12-1264 (2008).
- 254 Askjaer, P. *et al.* RanGTP-regulated interactions of CRM1 with nucleoporins and a shuttling DEAD-box helicase. *Mol Cell Biol* **19**, 6276-6285, doi:10.1128/MCB.19.9.6276 (1999).
- 255 Soto-Rifo, R. *et al.* DEAD-box protein DDX3 associates with eIF4F to promote translation of selected mRNAs. *EMBO J* **31**, 3745-3756, doi:10.1038/emboj.2012.220 (2012).
- 256 Chen, H. H., Yu, H. I., Yang, M. H. & Tarn, W. Y. DDX3 Activates CBC-eIF3-Mediated Translation of uORF-Containing Oncogenic mRNAs to Promote Metastasis in HNSCC. *Cancer Res* **78**, 4512-4523, doi:10.1158/0008-5472.CAN-18-0282 (2018).
- 257 Ku, Y. C. *et al.* DDX3 Participates in Translational Control of Inflammation Induced by Infections and Injuries. *Mol Cell Biol* **39**, doi:10.1128/MCB.00285-18 (2019).

- 258 Linsalata, A. E. *et al.* DDX3X and specific initiation factors modulate FMR1 repeat-associated non-AUG-initiated translation. *EMBO Rep* **20**, e47498, doi:10.15252/embr.201847498 (2019).
- 259 Cheng, W. *et al.* CRISPR-Cas9 Screens Identify the RNA Helicase DDX3X as a Repressor of C9ORF72 (GGGGCC)_n Repeat-Associated Non-AUG Translation. *Neuron* **104**, 885-898 e888, doi:10.1016/j.neuron.2019.09.003 (2019).
- 260 Zu, T. *et al.* Non-ATG-initiated translation directed by microsatellite expansions. *Proc Natl Acad Sci U S A* **108**, 260-265, doi:10.1073/pnas.1013343108 (2011).
- 261 Jain, S. *et al.* ATPase-Modulated Stress Granules Contain a Diverse Proteome and Substructure. *Cell* **164**, 487-498, doi:10.1016/j.cell.2015.12.038 (2016).
- 262 Dolde, C. *et al.* A CK1 FRET biosensor reveals that DDX3X is an essential activator of CK1epsilon. *J Cell Sci* **131**, doi:10.1242/jcs.207316 (2018).
- 263 Cruciat, C. M. *et al.* RNA helicase DDX3 is a regulatory subunit of casein kinase 1 in Wnt-beta-catenin signaling. *Science* **339**, 1436-1441, doi:10.1126/science.1231499 (2013).
- 264 Soulat, D. *et al.* The DEAD-box helicase DDX3X is a critical component of the TANK-binding kinase 1-dependent innate immune response. *EMBO J* **27**, 2135-2146, doi:10.1038/emboj.2008.126 (2008).
- 265 Schroder, M., Baran, M. & Bowie, A. G. Viral targeting of DEAD box protein 3 reveals its role in TBK1/IKKepsilon-mediated IRF activation. *EMBO J* **27**, 2147-2157, doi:10.1038/emboj.2008.143 (2008).
- 266 Gu, L., Fullam, A., Brennan, R. & Schroder, M. Human DEAD box helicase 3 couples I κ B kinase epsilon to interferon regulatory factor 3 activation. *Mol Cell Biol* **33**, 2004-2015, doi:10.1128/MCB.01603-12 (2013).
- 267 Oshiumi, H., Sakai, K., Matsumoto, M. & Seya, T. DEAD/H BOX 3 (DDX3) helicase binds the RIG-I adaptor IPS-1 to up-regulate IFN-beta-inducing potential. *Eur J Immunol* **40**, 940-948, doi:10.1002/eji.200940203 (2010).
- 268 Gu, L., Fullam, A., McCormack, N., Hohn, Y. & Schroder, M. DDX3 directly regulates TRAF3 ubiquitination and acts as a scaffold to coordinate assembly of signalling complexes downstream from MAVS. *Biochem J* **474**, 571-587, doi:10.1042/BCJ20160956 (2017).
- 269 Fullam, A., Gu, L., Hohn, Y. & Schroder, M. DDX3 directly facilitates IKKalpha activation and regulates downstream signalling pathways. *Biochem J* **475**, 3595-3607, doi:10.1042/BCJ20180163 (2018).
- 270 Goubau, D., Deddouche, S. & Reis e Sousa, C. Cytosolic sensing of viruses. *Immunity* **38**, 855-869, doi:10.1016/j.immuni.2013.05.007 (2013).

- 271 Rehwinkel, J. & Gack, M. U. RIG-I-like receptors: their regulation and roles in RNA sensing. *Nat Rev Immunol* **20**, 537-551, doi:10.1038/s41577-020-0288-3 (2020).
- 272 Tang, L. *et al.* Prospective and detailed behavioral phenotyping in DDX3X syndrome. *Mol Autism* **12**, 36, doi:10.1186/s13229-021-00431-z (2021).
- 273 Chen, H. H., Yu, H. I. & Tarn, W. Y. DDX3 Modulates Neurite Development via Translationally Activating an RNA Regulon Involved in Rac1 Activation. *J Neurosci* **36**, 9792-9804, doi:10.1523/JNEUROSCI.4603-15.2016 (2016).
- 274 Zhao, L. *et al.* Multifunctional DDX3: dual roles in various cancer development and its related signaling pathways. *Am J Cancer Res* **6**, 387-402 (2016).
- 275 Lin, T. C. DDX3X Multifunctionally Modulates Tumor Progression and Serves as a Prognostic Indicator to Predict Cancer Outcomes. *Int J Mol Sci* **21**, doi:10.3390/ijms21010281 (2019).
- 276 Mo, J. *et al.* DDX3X: structure, physiologic functions and cancer. *Mol Cancer* **20**, 38, doi:10.1186/s12943-021-01325-7 (2021).
- 277 Heerma van Voss, M. R. *et al.* Targeting mitochondrial translation by inhibiting DDX3: a novel radiosensitization strategy for cancer treatment. *Oncogene* **37**, 63-74, doi:10.1038/onc.2017.308 (2018).
- 278 Montes-Mojarro, I. A. *et al.* Mutational profile and EBV strains of extranodal NK/T-cell lymphoma, nasal type in Latin America. *Mod Pathol* **33**, 781-791, doi:10.1038/s41379-019-0415-5 (2020).
- 279 Tantravedi, S. *et al.* Targeting DDX3 in Medulloblastoma Using the Small Molecule Inhibitor RK-33. *Transl Oncol* **12**, 96-105, doi:10.1016/j.tranon.2018.09.002 (2019).
- 280 Xie, M. *et al.* RK-33 Radiosensitizes Prostate Cancer Cells by Blocking the RNA Helicase DDX3. *Cancer Res* **76**, 6340-6350, doi:10.1158/0008-5472.CAN-16-0440 (2016).
- 281 Miao, X. *et al.* Nectin-2 and DDX3 are biomarkers for metastasis and poor prognosis of squamous cell/adenosquamous carcinomas and adenocarcinoma of gallbladder. *Int J Clin Exp Pathol* **6**, 179-190 (2013).
- 282 Liang, S. *et al.* The Clinical and Pathological Significance of Nectin-2 and DDX3 Expression in Pancreatic Ductal Adenocarcinomas. *Dis Markers* **2015**, 379568, doi:10.1155/2015/379568 (2015).
- 283 Zheng, Y. *et al.* DEAD-Box Helicase 3 X-Linked Promotes Metastasis by Inducing Epithelial-Mesenchymal Transition via p62/Sequestosome-1. *Dig Dis Sci* **66**, 3893-3902, doi:10.1007/s10620-020-06735-z (2021).
- 284 el Mezni, F. *et al.* [Histopathologic aspects of pre-AIDS lymph nodes (apropos fo 2 cases)]. *Tunis Med* **67**, 547-551 (1989).

- 285 Su, C. Y. *et al.* DDX3 as a strongest prognosis marker and its downregulation promotes metastasis in colorectal cancer. *Oncotarget* **6**, 18602-18612, doi:10.18632/oncotarget.4329 (2015).
- 286 Bol, G. M. *et al.* Expression of the RNA helicase DDX3 and the hypoxia response in breast cancer. *PLoS One* **8**, e63548, doi:10.1371/journal.pone.0063548 (2013).
- 287 Wang, Y. *et al.* Distinct Ring1b complexes defined by DEAD-box helicases and EMT transcription factors synergistically enhance E-cadherin silencing in breast cancer. *Cell Death Dis* **12**, 202, doi:10.1038/s41419-021-03491-4 (2021).
- 288 Vellky, J. E., McSweeney, S. T., Ricke, E. A. & Ricke, W. A. RNA-binding protein DDX3 mediates posttranscriptional regulation of androgen receptor: A mechanism of castration resistance. *Proc Natl Acad Sci U S A* **117**, 28092-28101, doi:10.1073/pnas.2008479117 (2020).
- 289 Vellky, J. E., Ricke, E. A., Huang, W. & Ricke, W. A. Expression and Localization of DDX3 in Prostate Cancer Progression and Metastasis. *Am J Pathol* **189**, 1256-1267, doi:10.1016/j.ajpath.2019.02.011 (2019).
- 290 Wu, D. W. *et al.* Reduced p21(WAF1/CIP1) via alteration of p53-DDX3 pathway is associated with poor relapse-free survival in early-stage human papillomavirus-associated lung cancer. *Clin Cancer Res* **17**, 1895-1905, doi:10.1158/1078-0432.CCR-10-2316 (2011).
- 291 Wu, D. W. *et al.* DDX3 loss by p53 inactivation promotes tumor malignancy via the MDM2/Slug/E-cadherin pathway and poor patient outcome in non-small-cell lung cancer. *Oncogene* **33**, 1515-1526, doi:10.1038/onc.2013.107 (2014).
- 292 Lin, T. C. DDX3X is Epigenetically Repressed in Renal Cell Carcinoma and Serves as a Prognostic Indicator and Therapeutic Target in Cancer Progression. *Int J Mol Sci* **21**, doi:10.3390/ijms21082881 (2020).
- 293 Fu, R. *et al.* Avenanthramide A triggers potent ROS-mediated anti-tumor effects in colorectal cancer by directly targeting DDX3. *Cell Death Dis* **10**, 593, doi:10.1038/s41419-019-1825-5 (2019).
- 294 Wu, D. W., Lin, P. L., Wang, L., Huang, C. C. & Lee, H. The YAP1/SIX2 axis is required for DDX3-mediated tumor aggressiveness and cetuximab resistance in KRAS-wild-type colorectal cancer. *Theranostics* **7**, 1114-1132, doi:10.7150/thno.18175 (2017).
- 295 Wu, D. W. *et al.* DDX3 enhances oncogenic KRAS-induced tumor invasion in colorectal cancer via the betacatenin/ZEB1 axis. *Oncotarget* **7**, 22687-22699, doi:10.18632/oncotarget.8143 (2016).
- 296 He, T. Y. *et al.* DDX3 promotes tumor invasion in colorectal cancer via the CK1epsilon/Dvl2 axis. *Sci Rep* **6**, 21483, doi:10.1038/srep21483 (2016).

- 297 Heerma van Voss, M. R. *et al.* Identification of the DEAD box RNA helicase DDX3 as a therapeutic target in colorectal cancer. *Oncotarget* **6**, 28312-28326, doi:10.18632/oncotarget.4873 (2015).
- 298 Shriwas, O. *et al.* DDX3 modulates cisplatin resistance in OSCC through ALKBH5-mediated m(6)A-demethylation of FOXM1 and NANOG. *Apoptosis* **25**, 233-246, doi:10.1007/s10495-020-01591-8 (2020).
- 299 Geck, P. & Pfeiffer, B. Inhibition of ion transport in Ehrlich cells by muzolimine. *Naunyn Schmiedebergs Arch Pharmacol* **333**, 323-329, doi:10.1007/BF00512948 (1986).
- 300 Lee, C. H. *et al.* Low/negative expression of DDX3 might predict poor prognosis in non-smoker patients with oral cancer. *Oral Dis* **20**, 76-83, doi:10.1111/odi.12076 (2014).
- 301 Heerma van Voss, M. R. *et al.* DDX3 has divergent roles in head and neck squamous cell carcinomas in smoking versus non-smoking patients. *Oral Dis* **21**, 270-271, doi:10.1111/odi.12299 (2015).
- 302 Chang, P. C. *et al.* DDX3, a DEAD box RNA helicase, is deregulated in hepatitis virus-associated hepatocellular carcinoma and is involved in cell growth control. *Oncogene* **25**, 1991-2003, doi:10.1038/sj.onc.1209239 (2006).
- 303 Huang, J. S. *et al.* Diverse cellular transformation capability of overexpressed genes in human hepatocellular carcinoma. *Biochem Biophys Res Commun* **315**, 950-958, doi:10.1016/j.bbrc.2004.01.151 (2004).
- 304 Meier-Abt, F. *et al.* The protein landscape of chronic lymphocytic leukemia. *Blood* **138**, 2514-2525, doi:10.1182/blood.2020009741 (2021).
- 305 Takahashi, K. *et al.* Clinical implications of cancer gene mutations in patients with chronic lymphocytic leukemia treated with lenalidomide. *Blood* **131**, 1820-1832, doi:10.1182/blood-2017-11-817296 (2018).
- 306 Yu, L. *et al.* Survival of Del17p CLL Depends on Genomic Complexity and Somatic Mutation. *Clin Cancer Res* **23**, 735-745, doi:10.1158/1078-0432.CCR-16-0594 (2017).
- 307 Vollbrecht, C. *et al.* Comprehensive Analysis of Disease-Related Genes in Chronic Lymphocytic Leukemia by Multiplex PCR-Based Next Generation Sequencing. *PLoS One* **10**, e0129544, doi:10.1371/journal.pone.0129544 (2015).
- 308 Ojha, J. *et al.* Identification of recurrent truncated DDX3X mutations in chronic lymphocytic leukaemia. *Br J Haematol* **169**, 445-448, doi:10.1111/bjh.13211 (2015).
- 309 Wang, L. *et al.* SF3B1 and other novel cancer genes in chronic lymphocytic leukemia. *N Engl J Med* **365**, 2497-2506, doi:10.1056/NEJMoa1109016 (2011).

- 310 Gonzalez-Farre, B. *et al.* Burkitt-like lymphoma with 11q aberration: a germinal center-derived lymphoma genetically unrelated to Burkitt lymphoma. *Haematologica* **104**, 1822-1829, doi:10.3324/haematol.2018.207928 (2019).
- 311 Ramis-Zaldivar, J. E. *et al.* Distinct molecular profile of IRF4-rearranged large B-cell lymphoma. *Blood* **135**, 274-286, doi:10.1182/blood.2019002699 (2020).
- 312 Zhou, P. *et al.* Sporadic and endemic Burkitt lymphoma have frequent FOXO1 mutations but distinct hotspots in the AKT recognition motif. *Blood Adv* **3**, 2118-2127, doi:10.1182/bloodadvances.2018029546 (2019).
- 313 Gong, C. *et al.* Sequential inverse dysregulation of the RNA helicases DDX3X and DDX3Y facilitates MYC-driven lymphomagenesis. *Mol Cell* **81**, 4059-4075 e4011, doi:10.1016/j.molcel.2021.07.041 (2021).
- 314 Dobashi, A. *et al.* Frequent BCOR aberrations in extranodal NK/T-Cell lymphoma, nasal type. *Genes Chromosomes Cancer* **55**, 460-471, doi:10.1002/gcc.22348 (2016).
- 315 Jiang, L. *et al.* Exome sequencing identifies somatic mutations of DDX3X in natural killer/T-cell lymphoma. *Nat Genet* **47**, 1061-1066, doi:10.1038/ng.3358 (2015).
- 316 Gao, L. M. *et al.* Somatic mutations in KMT2D and TET2 associated with worse prognosis in Epstein-Barr virus-associated T or natural killer-cell lymphoproliferative disorders. *Cancer Biol Ther* **20**, 1319-1327, doi:10.1080/15384047.2019.1638670 (2019).
- 317 Gajjar, A. *et al.* Outcomes by Clinical and Molecular Features in Children With Medulloblastoma Treated With Risk-Adapted Therapy: Results of an International Phase III Trial (SJMB03). *J Clin Oncol* **39**, 822-835, doi:10.1200/JCO.20.01372 (2021).
- 318 Wong, G. C. *et al.* Clinical and mutational profiles of adult medulloblastoma groups. *Acta Neuropathol Commun* **8**, 191, doi:10.1186/s40478-020-01066-6 (2020).
- 319 Kool, M. *et al.* Genome sequencing of SHH medulloblastoma predicts genotype-related response to smoothed inhibition. *Cancer Cell* **25**, 393-405, doi:10.1016/j.ccr.2014.02.004 (2014).
- 320 Jones, D. T. *et al.* Dissecting the genomic complexity underlying medulloblastoma. *Nature* **488**, 100-105, doi:10.1038/nature11284 (2012).
- 321 Pugh, T. J. *et al.* Medulloblastoma exome sequencing uncovers subtype-specific somatic mutations. *Nature* **488**, 106-110, doi:10.1038/nature11329 (2012).
- 322 Robinson, G. *et al.* Novel mutations target distinct subgroups of medulloblastoma. *Nature* **488**, 43-48, doi:10.1038/nature11213 (2012).

- 323 Hernandez-Diaz, T., Valiente-Echeverria, F. & Soto-Rifo, R. RNA Helicase DDX3: A Double-Edged Sword for Viral Replication and Immune Signaling. *Microorganisms* **9**, doi:10.3390/microorganisms9061206 (2021).
- 324 Vashist, S., Urena, L., Chaudhry, Y. & Goodfellow, I. Identification of RNA-protein interaction networks involved in the norovirus life cycle. *J Virol* **86**, 11977-11990, doi:10.1128/JVI.00432-12 (2012).
- 325 Chahar, H. S., Chen, S. & Manjunath, N. P-body components LSM1, GW182, DDX3, DDX6 and XRN1 are recruited to WNV replication sites and positively regulate viral replication. *Virology* **436**, 1-7, doi:10.1016/j.virol.2012.09.041 (2013).
- 326 Li, C. *et al.* Cellular DDX3 regulates Japanese encephalitis virus replication by interacting with viral un-translated regions. *Virology* **449**, 70-81, doi:10.1016/j.virol.2013.11.008 (2014).
- 327 Su, Y. S. *et al.* Stimulation of the Internal Ribosome Entry Site (IRES)-Dependent Translation of Enterovirus 71 by DDX3X RNA Helicase and Viral 2A and 3C Proteases. *Front Microbiol* **9**, 1324, doi:10.3389/fmicb.2018.01324 (2018).
- 328 Han, S. *et al.* Ribosomal Protein L13 Promotes IRES-Driven Translation of Foot-and-Mouth Disease Virus in a Helicase DDX3-Dependent Manner. *J Virol* **94**, doi:10.1128/JVI.01679-19 (2020).
- 329 Bushman, F. D. *et al.* Host cell factors in HIV replication: meta-analysis of genome-wide studies. *PLoS Pathog* **5**, e1000437, doi:10.1371/journal.ppat.1000437 (2009).
- 330 Lai, M. C. *et al.* Human DDX3 interacts with the HIV-1 Tat protein to facilitate viral mRNA translation. *PLoS One* **8**, e68665, doi:10.1371/journal.pone.0068665 (2013).
- 331 Ishaq, M. *et al.* Knockdown of cellular RNA helicase DDX3 by short hairpin RNAs suppresses HIV-1 viral replication without inducing apoptosis. *Mol Biotechnol* **39**, 231-238, doi:10.1007/s12033-008-9040-0 (2008).
- 332 Khadivjam, B. *et al.* The ATP-Dependent RNA Helicase DDX3X Modulates Herpes Simplex Virus 1 Gene Expression. *J Virol* **91**, doi:10.1128/JVI.02411-16 (2017).
- 333 Cavnac, Y. *et al.* The Cellular Proteins Grb2 and DDX3 Are Increased upon Human Cytomegalovirus Infection and Act in a Proviral Fashion. *PLoS One* **10**, e0131614, doi:10.1371/journal.pone.0131614 (2015).
- 334 Ciccocanti, F. *et al.* Proteomic analysis identifies the RNA helicase DDX3X as a host target against SARS-CoV-2 infection. *Antiviral Res* **190**, 105064, doi:10.1016/j.antiviral.2021.105064 (2021).
- 335 Soto-Rifo, R., Rubilar, P. S. & Ohlmann, T. The DEAD-box helicase DDX3 substitutes for the cap-binding protein eIF4E to promote

- compartmentalized translation initiation of the HIV-1 genomic RNA. *Nucleic Acids Res* **41**, 6286-6299, doi:10.1093/nar/gkt306 (2013).
- 336 Liu, J., Henao-Mejia, J., Liu, H., Zhao, Y. & He, J. J. Translational regulation of HIV-1 replication by HIV-1 Rev cellular cofactors Sam68, eIF5A, hRIP, and DDX3. *J Neuroimmune Pharmacol* **6**, 308-321, doi:10.1007/s11481-011-9265-8 (2011).
- 337 Loureiro, M. E. *et al.* DDX3 suppresses type I interferons and favors viral replication during Arenavirus infection. *PLoS Pathog* **14**, e1007125, doi:10.1371/journal.ppat.1007125 (2018).
- 338 Pene, V., Li, Q., Sodroski, C., Hsu, C. S. & Liang, T. J. Dynamic Interaction of Stress Granules, DDX3X, and IKK-alpha Mediates Multiple Functions in Hepatitis C Virus Infection. *J Virol* **89**, 5462-5477, doi:10.1128/JVI.03197-14 (2015).
- 339 Owsianka, A. M. & Patel, A. H. Hepatitis C virus core protein interacts with a human DEAD box protein DDX3. *Virology* **257**, 330-340, doi:10.1006/viro.1999.9659 (1999).
- 340 You, L. R. *et al.* Hepatitis C virus core protein interacts with cellular putative RNA helicase. *J Virol* **73**, 2841-2853, doi:10.1128/JVI.73.4.2841-2853.1999 (1999).
- 341 Angus, A. G. *et al.* Requirement of cellular DDX3 for hepatitis C virus replication is unrelated to its interaction with the viral core protein. *J Gen Virol* **91**, 122-132, doi:10.1099/vir.0.015909-0 (2010).
- 342 Oshiumi, H. *et al.* Hepatitis C virus core protein abrogates the DDX3 function that enhances IPS-1-mediated IFN-beta induction. *PLoS One* **5**, e14258, doi:10.1371/journal.pone.0014258 (2010).
- 343 Ko, C., Lee, S., Windisch, M. P. & Ryu, W. S. DDX3 DEAD-box RNA helicase is a host factor that restricts hepatitis B virus replication at the transcriptional level. *J Virol* **88**, 13689-13698, doi:10.1128/JVI.02035-14 (2014).
- 344 Wang, H., Kim, S. & Ryu, W. S. DDX3 DEAD-Box RNA helicase inhibits hepatitis B virus reverse transcription by incorporation into nucleocapsids. *J Virol* **83**, 5815-5824, doi:10.1128/JVI.00011-09 (2009).
- 345 Yu, S. *et al.* Hepatitis B virus polymerase inhibits RIG-I- and Toll-like receptor 3-mediated beta interferon induction in human hepatocytes through interference with interferon regulatory factor 3 activation and dampening of the interaction between TBK1/IKKepsilon and DDX3. *J Gen Virol* **91**, 2080-2090, doi:10.1099/vir.0.020552-0 (2010).
- 346 Li, G., Feng, T., Pan, W., Shi, X. & Dai, J. DEAD-box RNA helicase DDX3X inhibits DENV replication via regulating type one interferon pathway. *Biochem Biophys Res Commun* **456**, 327-332, doi:10.1016/j.bbrc.2014.11.080 (2015).

- 347 Kumar, R., Singh, N., Abdin, M. Z., Patel, A. H. & Medigeshi, G. R. Dengue Virus Capsid Interacts with DDX3X-A Potential Mechanism for Suppression of Antiviral Functions in Dengue Infection. *Front Cell Infect Microbiol* **7**, 542, doi:10.3389/fcimb.2017.00542 (2017).
- 348 Thulasi Raman, S. N. *et al.* DDX3 Interacts with Influenza A Virus NS1 and NP Proteins and Exerts Antiviral Function through Regulation of Stress Granule Formation. *J Virol* **90**, 3661-3675, doi:10.1128/JVI.03010-15 (2016).
- 349 Kesavardhana, S. *et al.* DDX3X coordinates host defense against influenza virus by activating the NLRP3 inflammasome and type I interferon response. *J Biol Chem* **296**, 100579, doi:10.1016/j.jbc.2021.100579 (2021).
- 350 Lai, M. C., Sun, H. S., Wang, S. W. & Tarn, W. Y. DDX3 functions in antiviral innate immunity through translational control of PACT. *FEBS J* **283**, 88-101, doi:10.1111/febs.13553 (2016).
- 351 Winnard, P. T., Jr., Vesuna, F. & Raman, V. Targeting host DEAD-box RNA helicase DDX3X for treating viral infections. *Antiviral Res* **185**, 104994, doi:10.1016/j.antiviral.2020.104994 (2021).
- 352 Smith, G. L. *et al.* Vaccinia virus immune evasion: mechanisms, virulence and immunogenicity. *J Gen Virol* **94**, 2367-2392, doi:10.1099/vir.0.055921-0 (2013).
- 353 Guo, Z. S. *et al.* Vaccinia virus-mediated cancer immunotherapy: cancer vaccines and oncolytics. *J Immunother Cancer* **7**, 6, doi:10.1186/s40425-018-0495-7 (2019).
- 354 Volz, A. & Sutter, G. Modified Vaccinia Virus Ankara: History, Value in Basic Research, and Current Perspectives for Vaccine Development. *Adv Virus Res* **97**, 187-243, doi:10.1016/bs.aivir.2016.07.001 (2017).
- 355 Casadevall, A. & Pirofski, L. A. Virulence factors and their mechanisms of action: the view from a damage-response framework. *J Water Health* **7 Suppl 1**, S2-S18, doi:10.2166/wh.2009.036 (2009).
- 356 Pirofski, L. A. & Casadevall, A. The damage-response framework of microbial pathogenesis and infectious diseases. *Adv Exp Med Biol* **635**, 135-146, doi:10.1007/978-0-387-09550-9_11 (2008).
- 357 Bull, J. J. & Luring, A. S. Theory and empiricism in virulence evolution. *PLoS Pathog* **10**, e1004387, doi:10.1371/journal.ppat.1004387 (2014).
- 358 Benfield, C. T. O., Ren, H., Lucas, S. J., Bahsoun, B. & Smith, G. L. Vaccinia virus protein K7 is a virulence factor that alters the acute immune response to infection. *J Gen Virol* **94**, 1647-1657, doi:10.1099/vir.0.052670-0 (2013).

- 359 Chen, N. *et al.* Virulence differences between monkeypox virus isolates from West Africa and the Congo basin. *Virology* **340**, 46-63, doi:10.1016/j.virol.2005.05.030 (2005).
- 360 Keasey, S. *et al.* Proteomic basis of the antibody response to monkeypox virus infection examined in cynomolgus macaques and a comparison to human smallpox vaccination. *PLoS One* **5**, e15547, doi:10.1371/journal.pone.0015547 (2010).
- 361 Li, Y., Zhang, L. & Ke, Y. Cellular interactome analysis of vaccinia virus K7 protein identifies three transport machineries as binding partners for K7. *Virus Genes* **53**, 814-822, doi:10.1007/s11262-017-1504-5 (2017).
- 362 Pichlmair, A. *et al.* Viral immune modulators perturb the human molecular network by common and unique strategies. *Nature* **487**, 486-490, doi:10.1038/nature11289 (2012).
- 363 Torres, A. A. *et al.* The actin nucleator Spir-1 is a virus restriction factor that promotes innate immune signalling. *PLoS Pathog* **18**, e1010277, doi:10.1371/journal.ppat.1010277 (2022).
- 364 Oda, S., Schroder, M. & Khan, A. R. Structural basis for targeting of human RNA helicase DDX3 by poxvirus protein K7. *Structure* **17**, 1528-1537, doi:10.1016/j.str.2009.09.005 (2009).
- 365 Kalverda, A. P. *et al.* Poxvirus K7 protein adopts a Bcl-2 fold: biochemical mapping of its interactions with human DEAD box RNA helicase DDX3. *J Mol Biol* **385**, 843-853, doi:10.1016/j.jmb.2008.09.048 (2009).
- 366 Venus, S. & Jankowsky, E. Measuring the impact of cofactors on RNA helicase activities. *Methods* **204**, 376-385, doi:10.1016/j.ymeth.2022.04.005 (2022).
- 367 Roberts, K. L. & Smith, G. L. Vaccinia virus morphogenesis and dissemination. *Trends Microbiol* **16**, 472-479, doi:10.1016/j.tim.2008.07.009 (2008).
- 368 Kieser, Q., Noyce, R. S., Shenouda, M., Lin, Y. J. & Evans, D. H. Cytoplasmic factories, virus assembly, and DNA replication kinetics collectively constrain the formation of poxvirus recombinants. *PLoS One* **15**, e0228028, doi:10.1371/journal.pone.0228028 (2020).
- 369 Liem, J. & Liu, J. Stress Beyond Translation: Poxviruses and More. *Viruses* **8**, doi:10.3390/v8060169 (2016).
- 370 Moss, B. Poxvirus DNA replication. *Cold Spring Harb Perspect Biol* **5**, doi:10.1101/cshperspect.a010199 (2013).
- 371 Brownsword, M. J. & Locker, N. A little less aggregation a little more replication: Viral manipulation of stress granules. *Wiley Interdiscip Rev RNA*, e1741, doi:10.1002/wrna.1741 (2022).
- 372 Gaete-Argel, A., Marquez, C. L., Barriga, G. P., Soto-Rifo, R. & Valiente-Echeverria, F. Strategies for Success. *Viral Infections and Membraneless*

- Organelles. *Front Cell Infect Microbiol* **9**, 336, doi:10.3389/fcimb.2019.00336 (2019).
- 373 Lloyd, R. E. How do viruses interact with stress-associated RNA granules? *PLoS Pathog* **8**, e1002741, doi:10.1371/journal.ppat.1002741 (2012).
- 374 Gao, J. *et al.* G-quadruplex DNA inhibits unwinding activity but promotes liquid-liquid phase separation by the DEAD-box helicase Ded1p. *Chem Commun (Camb)* **57**, 7445-7448, doi:10.1039/d1cc01479j (2021).
- 375 Zhang, K. *et al.* Stress Granule Assembly Disrupts Nucleocytoplasmic Transport. *Cell* **173**, 958-971 e917, doi:10.1016/j.cell.2018.03.025 (2018).
- 376 Yang, P. *et al.* G3BP1 Is a Tunable Switch that Triggers Phase Separation to Assemble Stress Granules. *Cell* **181**, 325-345 e328, doi:10.1016/j.cell.2020.03.046 (2020).
- 377 Kim, J. H. *et al.* High cleavage efficiency of a 2A peptide derived from porcine teschovirus-1 in human cell lines, zebrafish and mice. *PLoS One* **6**, e18556, doi:10.1371/journal.pone.0018556 (2011).
- 378 Rozelle, D. K., Filone, C. M., Kedersha, N. & Connor, J. H. Activation of stress response pathways promotes formation of antiviral granules and restricts virus replication. *Mol Cell Biol* **34**, 2003-2016, doi:10.1128/MCB.01630-13 (2014).
- 379 Schierhorn, K. L. *et al.* Influenza A Virus Virulence Depends on Two Amino Acids in the N-Terminal Domain of Its NS1 Protein To Facilitate Inhibition of the RNA-Dependent Protein Kinase PKR. *J Virol* **91**, doi:10.1128/JVI.00198-17 (2017).
- 380 Fernandez-Carrillo, C., Perez-Vilaro, G., Diez, J. & Perez-Del-Pulgar, S. Hepatitis C virus plays with fire and yet avoids getting burned. A review for clinicians on processing bodies and stress granules. *Liver Int* **38**, 388-398, doi:10.1111/liv.13541 (2018).
- 381 Shih, J. W., Tsai, T. Y., Chao, C. H. & Wu Lee, Y. H. Candidate tumor suppressor DDX3 RNA helicase specifically represses cap-dependent translation by acting as an eIF4E inhibitory protein. *Oncogene* **27**, 700-714, doi:10.1038/sj.onc.1210687 (2008).
- 382 Dhungel, P., Cantu, F. M., Molina, J. A. & Yang, Z. Vaccinia Virus as a Master of Host Shutoff Induction: Targeting Processes of the Central Dogma and Beyond. *Pathogens* **9**, doi:10.3390/pathogens9050400 (2020).
- 383 Dai, A. *et al.* Ribosome Profiling Reveals Translational Upregulation of Cellular Oxidative Phosphorylation mRNAs during Vaccinia Virus-Induced Host Shutoff. *J Virol* **91**, doi:10.1128/JVI.01858-16 (2017).

- 384 Aviner, R. The science of puromycin: From studies of ribosome function to applications in biotechnology. *Comput Struct Biotechnol J* **18**, 1074-1083, doi:10.1016/j.csbj.2020.04.014 (2020).
- 385 Wang, F., Li, J., Fan, S., Jin, Z. & Huang, C. Targeting stress granules: A novel therapeutic strategy for human diseases. *Pharmacol Res* **161**, 105143, doi:10.1016/j.phrs.2020.105143 (2020).
- 386 Wheeler, R. J. Therapeutics-how to treat phase separation-associated diseases. *Emerg Top Life Sci* **4**, 307-318, doi:10.1042/ETLS20190176 (2020).
- 387 Mullard, A. Biomolecular condensates pique drug discovery curiosity. *Nat Rev Drug Discov*, doi:10.1038/d41573-019-00069-w (2019).
- 388 Dolgin, E. Drug startups coalesce around condensates. *Nat Biotechnol* **39**, 123-125, doi:10.1038/s41587-021-00828-4 (2021).
- 389 Choi, K. J. *et al.* A Chemical Chaperone Decouples TDP-43 Disordered Domain Phase Separation from Fibrillation. *Biochemistry* **57**, 6822-6826, doi:10.1021/acs.biochem.8b01051 (2018).
- 390 Latron, F. *et al.* Active suppression of major histocompatibility complex class II gene expression during differentiation from B cells to plasma cells. *Proc Natl Acad Sci U S A* **85**, 2229-2233, doi:10.1073/pnas.85.7.2229 (1988).
- 391 Richard J Wheeler, H. O. L., Ina Poser, Arun Pal, Thom Doeleman, Satoshi Kishigami, Sukhleen Kour, Eric Nathaniel Anderson, Lara Marrone, Anastasia C Murthy, Marcus Jahnel, Xiaojie Zhang, Edgar Boczek, Anatol Fritsch, Nicolas L Fawzi, Jared Sternecker, Udai Pandey, Della C David, Benjamin G Davis, Andrew J Baldwin, Andreas Hermann, Marc Bickle, Simon Albertia, Anthony A Hyman. Small molecules for modulating protein driven liquid-liquid phase separation in treating neurodegenerative disease. *bioRxiv*, doi:<https://doi.org/10.1101/721001> (2019).
- 392 De Mol, E. *et al.* EPI-001, A Compound Active against Castration-Resistant Prostate Cancer, Targets Transactivation Unit 5 of the Androgen Receptor. *ACS Chem Biol* **11**, 2499-2505, doi:10.1021/acscchembio.6b00182 (2016).
- 393 Andersen, R. J. *et al.* Regression of castrate-recurrent prostate cancer by a small-molecule inhibitor of the amino-terminus domain of the androgen receptor. *Cancer Cell* **17**, 535-546, doi:10.1016/j.ccr.2010.04.027 (2010).
- 394 Krishnan, N. *et al.* Targeting the disordered C terminus of PTP1B with an allosteric inhibitor. *Nat Chem Biol* **10**, 558-566, doi:10.1038/nchembio.1528 (2014).
- 395 Metallo, S. J. Intrinsically disordered proteins are potential drug targets. *Curr Opin Chem Biol* **14**, 481-488, doi:10.1016/j.cbpa.2010.06.169 (2010).

- 396 Babinchak, W. M. *et al.* Small molecules as potent biphasic modulators of protein liquid-liquid phase separation. *Nat Commun* **11**, 5574, doi:10.1038/s41467-020-19211-z (2020).
- 397 Patel, A. *et al.* ATP as a biological hydrotrope. *Science* **356**, 753-756, doi:10.1126/science.aaf6846 (2017).
- 398 Saurabh, S. *et al.* ATP-responsive biomolecular condensates tune bacterial kinase signaling. *Sci Adv* **8**, eabm6570, doi:10.1126/sciadv.abm6570 (2022).
- 399 Kushwah, N., Jain, V. & Yadav, D. Osmolytes: A Possible Therapeutic Molecule for Ameliorating the Neurodegeneration Caused by Protein Misfolding and Aggregation. *Biomolecules* **10**, doi:10.3390/biom10010132 (2020).
- 400 Ignatova, Z. & Gierasch, L. M. Inhibition of protein aggregation in vitro and in vivo by a natural osmoprotectant. *Proc Natl Acad Sci U S A* **103**, 13357-13361, doi:10.1073/pnas.0603772103 (2006).
- 401 Krishnan, N., Dickman, M. B. & Becker, D. F. Proline modulates the intracellular redox environment and protects mammalian cells against oxidative stress. *Free Radic Biol Med* **44**, 671-681, doi:10.1016/j.freeradbiomed.2007.10.054 (2008).
- 402 Patriarca, E. J. *et al.* The Multifaceted Roles of Proline in Cell Behavior. *Front Cell Dev Biol* **9**, 728576, doi:10.3389/fcell.2021.728576 (2021).
- 403 Thiemicke, A. & Neuert, G. Kinetics of osmotic stress regulate a cell fate switch of cell survival. *Sci Adv* **7**, doi:10.1126/sciadv.abe1122 (2021).
- 404 Krokowski, D. *et al.* Stress-induced perturbations in intracellular amino acids reprogram mRNA translation in osmoadaptation independently of the ISR. *Cell Rep* **40**, 111092, doi:10.1016/j.celrep.2022.111092 (2022).
- 405 Ghisolfi, J. *et al.* Plasma free amino acids in normal children and in patients with proteinocaloric malnutrition: fasting and infection. *Pediatr Res* **12**, 912-917, doi:10.1203/00006450-197809000-00006 (1978).
- 406 Simpson-Holley, M. *et al.* Formation of antiviral cytoplasmic granules during orthopoxvirus infection. *J Virol* **85**, 1581-1593, doi:10.1128/JVI.02247-10 (2011).
- 407 Deater, M., Tamhankar, M. & Lloyd, R. E. TDRD3 is an antiviral restriction factor that promotes IFN signaling with G3BP1. *PLoS Pathog* **18**, e1010249, doi:10.1371/journal.ppat.1010249 (2022).
- 408 Gao, B. *et al.* Inhibition of anti-viral stress granule formation by coronavirus endoribonuclease nsp15 ensures efficient virus replication. *PLoS Pathog* **17**, e1008690, doi:10.1371/journal.ppat.1008690 (2021).
- 409 Swanson, K. V., Deng, M. & Ting, J. P. The NLRP3 inflammasome: molecular activation and regulation to therapeutics. *Nat Rev Immunol* **19**, 477-489, doi:10.1038/s41577-019-0165-0 (2019).

- 410 Arimoto, K., Fukuda, H., Imajoh-Ohmi, S., Saito, H. & Takekawa, M. Formation of stress granules inhibits apoptosis by suppressing stress-responsive MAPK pathways. *Nat Cell Biol* **10**, 1324-1332, doi:10.1038/ncb1791 (2008).
- 411 Crowley, L. C., Marfell, B. J., Scott, A. P. & Waterhouse, N. J. Quantitation of Apoptosis and Necrosis by Annexin V Binding, Propidium Iodide Uptake, and Flow Cytometry. *Cold Spring Harb Protoc* **2016**, doi:10.1101/pdb.prot087288 (2016).
- 412 Santolini, E., Migliaccio, G. & La Monica, N. Biosynthesis and biochemical properties of the hepatitis C virus core protein. *J Virol* **68**, 3631-3641, doi:10.1128/JVI.68.6.3631-3641.1994 (1994).
- 413 Ambroggio, E. E., Costa Navarro, G. S., Perez Socas, L. B., Bagatolli, L. A. & Gamarnik, A. V. Dengue and Zika virus capsid proteins bind to membranes and self-assemble into liquid droplets with nucleic acids. *J Biol Chem* **297**, 101059, doi:10.1016/j.jbc.2021.101059 (2021).
- 414 Zhang, L. *et al.* Influenza Virus NS1 Protein-RNA Interactome Reveals Intron Targeting. *J Virol* **92**, doi:10.1128/JVI.01634-18 (2018).
- 415 Hu, Y., Sneyd, H., Dekant, R. & Wang, J. Influenza A Virus Nucleoprotein: A Highly Conserved Multi-Functional Viral Protein as a Hot Antiviral Drug Target. *Curr Top Med Chem* **17**, 2271-2285, doi:10.2174/1568026617666170224122508 (2017).
- 416 Hornbeck, P. V. *et al.* PhosphoSitePlus, 2014: mutations, PTMs and recalibrations. *Nucleic Acids Res* **43**, D512-520, doi:10.1093/nar/gku1267 (2015).
- 417 Saito, M. *et al.* Acetylation of intrinsically disordered regions regulates phase separation. *Nat Chem Biol* **15**, 51-61, doi:10.1038/s41589-018-0180-7 (2019).
- 418 Minshall, N. & Standart, N. The active form of Xp54 RNA helicase in translational repression is an RNA-mediated oligomer. *Nucleic Acids Res* **32**, 1325-1334, doi:10.1093/nar/gkh303 (2004).
- 419 Garcia-Nafria, J., Watson, J. F. & Greger, I. H. IVA cloning: A single-tube universal cloning system exploiting bacterial In Vivo Assembly. *Sci Rep* **6**, 27459, doi:10.1038/srep27459 (2016).